

REPORT DOCUMENTATION PAGE			Form Approved OMB NO. 0704-0188		
<p>The public reporting burden for this collection of information is estimated to average 1 hour per response, including the time for reviewing instructions, searching existing data sources, gathering and maintaining the data needed, and completing and reviewing the collection of information. Send comments regarding this burden estimate or any other aspect of this collection of information, including suggestions for reducing this burden, to Washington Headquarters Services, Directorate for Information Operations and Reports, 1215 Jefferson Davis Highway, Suite 1204, Arlington VA, 22202-4302. Respondents should be aware that notwithstanding any other provision of law, no person shall be subject to any penalty for failing to comply with a collection of information if it does not display a currently valid OMB control number.</p> <p>PLEASE DO NOT RETURN YOUR FORM TO THE ABOVE ADDRESS.</p>					
1. REPORT DATE (DD-MM-YYYY) 30-09-2014		2. REPORT TYPE Final Report		3. DATES COVERED (From - To) 1-Mar-2009 - 30-Jun-2014	
4. TITLE AND SUBTITLE Final Report: Design and Demonstration of RSFQ Processor Datapath for High Performance Computing			5a. CONTRACT NUMBER		
			5b. GRANT NUMBER W911NF-09-C-0036		
			5c. PROGRAM ELEMENT NUMBER 611102		
6. AUTHORS Alex F. Kirichenko			5d. PROJECT NUMBER		
			5e. TASK NUMBER		
			5f. WORK UNIT NUMBER		
7. PERFORMING ORGANIZATION NAMES AND ADDRESSES HYPRES, Inc. 175 Clearbrook Road Elmsford, NY 10523 -1109			8. PERFORMING ORGANIZATION REPORT NUMBER		
9. SPONSORING/MONITORING AGENCY NAME(S) AND ADDRESS (ES) U.S. Army Research Office P.O. Box 12211 Research Triangle Park, NC 27709-2211			10. SPONSOR/MONITOR'S ACRONYM(S) ARO		
			11. SPONSOR/MONITOR'S REPORT NUMBER(S) 55336-PH-OC.17		
12. DISTRIBUTION AVAILABILITY STATEMENT Approved for Public Release; Distribution Unlimited					
13. SUPPLEMENTARY NOTES The views, opinions and/or findings contained in this report are those of the author(s) and should not be construed as an official Department of the Army position, policy or decision, unless so designated by other documentation.					
14. ABSTRACT The main goal of the project is designing in RSFQ technology a 20-GHz 8-bit-wide energy efficient processor datapath consisting of an 8-bit ALU, an 8x8-bit Register File, and an Instruction Decoder. We have had several project modifications resulted in additional tasks, such as the development of energy-efficient zero-static-power dissipation SFQ technology, the development of energy-efficient interface based on a low input voltage polarization modulating VCSELs, and the development of superconducting ferromagnetic Random Access Memory.					
15. SUBJECT TERMS energy efficient electronics, datapath, SFQ, ALU, register file, MRAM, VCSEL					
16. SECURITY CLASSIFICATION OF:			17. LIMITATION OF ABSTRACT UU	18. NUMBER OF PAGES	19a. NAME OF RESPONSIBLE PERSON Alex Kirichenko
a. REPORT UU	b. ABSTRACT UU	c. THIS PAGE UU			19b. TELEPHONE NUMBER 914-592-1190

Report Title

Final Report: Design and Demonstration of RSFQ Processor Datapath for High Performance Computing

ABSTRACT

The main goal of the project is designing in RSFQ technology a 20-GHz 8-bit-wide energy efficient processor datapath consisting of an 8-bit ALU, an 8x8-bit Register File, and an Instruction Decoder. We have had several project modifications resulted in additional tasks, such as the development of energy-efficient zero-static-power dissipation SFQ technology, the development of energy-efficient interface based on a low input voltage polarization modulating VCSELs, and the development of superconducting ferromagnetic Random Access Memory.

Enter List of papers submitted or published that acknowledge ARO support from the start of the project to the date of this printing. List the papers, including journal references, in the following categories:

(a) Papers published in peer-reviewed journals (N/A for none)

<u>Received</u>	<u>Paper</u>
08/30/2011 1.00	T. Filippov, M. Dorojevets, A. Sahu, A. Kirichenko, C. Ayala, O. Mukhanov. 8-Bit Asynchronous Wave-Pipelined RSFQ Arithmetic-Logic Unit, IEEE Transactions on Applied Superconductivity, (06 2011): 847. doi: 10.1109/TASC.2010.2103918
08/30/2011 4.00	Oleg A. Mukhanov. Energy-Efficient Single Flux Quantum Technology, IEEE Transactions on Applied Superconductivity, (06 2011): 760. doi: 10.1109/TASC.2010.2096792
08/30/2011 3.00	D. E. Kirichenko, S. Sarwana, A. F. Kirichenko. Zero Static Power Dissipation Biasing of RSFQ Circuits, IEEE Transactions on Applied Superconductivity, (06 2011): 776. doi: 10.1109/TASC.2010.2098432
08/30/2011 2.00	Mikhail Dorojevets, Christopher L. Ayala, Artur K. Kasperek. Data-Flow Microarchitecture for Wide Datapath RSFQ Processors: Design Study, IEEE Transactions on Applied Superconductivity, (06 2011): 787. doi: 10.1109/TASC.2010.2087410
09/30/2014 13.00	Oleksandr Chernyashevskyy, Georgy V. Prokopenko, Ivan P. Nevirkovets, Oleg A. Mukhanov, John B. Ketterson. Superconducting-Ferromagnetic Transistor, IEEE Transactions on Applied Superconductivity, (08 2014): 1800506. doi: 10.1109/TASC.2014.2318317
09/30/2014 14.00	O. A. Mukhanov, M. H. Volkmann, A. Sahu, C. J. Fourie. Experimental Investigation of Energy-Efficient Digital Circuits Based on eSFQ Logic, IEEE Transactions on Applied Superconductivity, (06 2013): 1301505. doi: 10.1109/TASC.2013.2240755
09/30/2014 15.00	O A Mukhanov, M H Volkmann, A Sahu, C J Fourie. Implementation of energy efficient single flux quantum digital circuits with sub-aJ/bit operation, Superconductor Science and Technology, (01 2013): 15002. doi: 10.1088/0953-2048/26/1/015002
TOTAL:	7

Number of Papers published in peer-reviewed journals:

(b) Papers published in non-peer-reviewed journals (N/A for none)

Received Paper

TOTAL:

Number of Papers published in non peer-reviewed journals:

(c) Presentations

Number of Presentations: 3.00

Non Peer-Reviewed Conference Proceeding publications (other than abstracts):

Received Paper

08/30/2012 5.00 Alex F. Kirichenko. ERSFQ - Zero Static Power Dissipation RSFQ Logic, Superconducting SFQ VLSI Workshop, SSV2011, Kyoto, Japan. 01-NOV-11, . : ,

TOTAL: 1

Number of Non Peer-Reviewed Conference Proceeding publications (other than abstracts):

Peer-Reviewed Conference Proceeding publications (other than abstracts):

Received Paper

09/30/2014 11.00 O. A. Mukhanov, I. Vernik, A. Kirichenko, A. Kadin, K. D. Choquette, M. P. Tan, T. Fryslie. Development of Energy-efficient Cryogenic Optical (ECO) data link, 2013 IEEE 14th International Superconductive Electronics Conference (ISEC). 07-JUL-13, Cambridge, MA, USA. : ,

TOTAL: 1

Number of Peer-Reviewed Conference Proceeding publications (other than abstracts):

(d) Manuscripts

<u>Received</u>	<u>Paper</u>
08/30/2012	7.00 Timur V. Filippov, Anubhav Sahu, Alex F. Kirichenko, Igor V. Vernik, Oleg A. Mukhanov, Mikhail Dorojevets, Christopher L. Ayala. 20 GHz operation of an asynchronous wave-pipelined RSFQ arithmetic logic unit, Physics Procedia (09 2012)
08/31/2012	8.00 M H Volkmann, A Sahu, C J Fourie, O A Mukhanov. Implementation of Energy Efficient Single Flux Quantum (eSFQ) Digital Circuits with sub-aJ/bit Operation, Supercond. Sci. Technol (08 2012)
09/30/2014	9.00 Alex F. Kirichenko, , Artur K. Kasperek, Mikhail Dorojevets, , Anubhav Sahu, , Timur V. Filippov, , Oleg A. Mukhanov, , Andriy V. Dotsenko,. Demonstration of an 8x8-bit RSFQ Multi-Port Register File, Proceedings of 14th IEEE International Superconductive Electronics conference (06 2013)
09/30/2014	16.00 Alex F. Kirichenko, Igor V. Vernik, John A. Vivalda, Rick T. Hunt, Daniel T. Yohannes. ERSFQ 8-bit parallel adders as a process benchmark, IEEE Transactions on Applied Superconductivity, (08 2014)
TOTAL:	4

Number of Manuscripts:

Books

<u>Received</u>	<u>Book</u>
-----------------	-------------

TOTAL:

TOTAL:

Patents Submitted

LOW-POWER BIASING NETWORKS FOR SUPERCONDUCTING INTEGRATED CIRCUITS

Patents Awarded

LOW-POWER BIASING NETWORKS FOR SUPERCONDUCTING INTEGRATED CIRCUITS

Awards

Graduate Students

<u>NAME</u>	<u>PERCENT SUPPORTED</u>
FTE Equivalent:	
Total Number:	

Names of Post Doctorates

<u>NAME</u>	<u>PERCENT SUPPORTED</u>
FTE Equivalent:	
Total Number:	

Names of Faculty Supported

<u>NAME</u>	<u>PERCENT SUPPORTED</u>
FTE Equivalent:	
Total Number:	

Names of Under Graduate students supported

<u>NAME</u>	<u>PERCENT SUPPORTED</u>
FTE Equivalent:	
Total Number:	

Student Metrics

This section only applies to graduating undergraduates supported by this agreement in this reporting period

The number of undergraduates funded by this agreement who graduated during this period: 0.00

The number of undergraduates funded by this agreement who graduated during this period with a degree in science, mathematics, engineering, or technology fields:..... 0.00

The number of undergraduates funded by your agreement who graduated during this period and will continue to pursue a graduate or Ph.D. degree in science, mathematics, engineering, or technology fields:..... 0.00

Number of graduating undergraduates who achieved a 3.5 GPA to 4.0 (4.0 max scale):..... 0.00

Number of graduating undergraduates funded by a DoD funded Center of Excellence grant for Education, Research and Engineering:..... 0.00

The number of undergraduates funded by your agreement who graduated during this period and intend to work for the Department of Defense 0.00

The number of undergraduates funded by your agreement who graduated during this period and will receive scholarships or fellowships for further studies in science, mathematics, engineering or technology fields: 0.00

Names of Personnel receiving masters degrees

NAME

Total Number:

Names of personnel receiving PHDs

NAME

Total Number:

Names of other research staff

NAME

PERCENT SUPPORTED

FTE Equivalent:

Total Number:

Sub Contractors (DD882)

1 a. InQubit, Inc.

1 b. 21143 Hawthorne Blvd. #459

Torrance

CA

90503

Sub Contractor Numbers (c):

Patent Clause Number (d-1):

Patent Date (d-2):

Work Description (e): SF Memory Development

Sub Contract Award Date (f-1):

Sub Contract Est Completion Date(f-2):

1 a. University of Illinois-Urbana Champagne

1 b.

00000

Sub Contractor Numbers (c):

Patent Clause Number (d-1):

Patent Date (d-2):

Work Description (e): development and demonstration of the energy-efficient output data interface based on VC

Sub Contract Award Date (f-1):

Sub Contract Est Completion Date(f-2):

1 a. University of Illinois-Urbana Champagne

1 b.

00000

Sub Contractor Numbers (c):

Patent Clause Number (d-1):

Patent Date (d-2):

Work Description (e): development and demonstration of the energy-efficient output data interface based on VC

Sub Contract Award Date (f-1):

Sub Contract Est Completion Date(f-2):

Inventions (DD882)

5 LOW-POWER BIASING NETWORKS FOR SUPERCONDUCTING INTEGRATED CIRCUITS

Patent Filed in US? (5d-1) Y

Patent Filed in Foreign Countries? (5d-2) N

Was the assignment forwarded to the contracting officer? (5e) N

Foreign Countries of application (5g-2):

5a: Alex Kirichenko

5f-1a: HYPRES

5f-c: 175 Clearbrook Rd

Elmsford ny 10523

5a: Dmitri Kirichenko

5f-1a: HYPRES

5f-c: 175 Clearbrook Rd

Elmsford NY 10523

5a: Oleg Mukhanov

5f-1a: HYPRES

5f-c: 175 Clearbrook Rd

Elmsford ny 10523

Scientific Progress

See Attachment

Technology Transfer

FINAL REPORT

Design and Demonstration of RSFQ Processor Datapath for High Performance Computing

Contract Number: W911NF-09-C-0036

Reporting Period: 7/30/2009 to 08/31/2014

Principal Investigator: Alex F. Kirichenko

HYPRES

175 Clearbrook Road

Elmsford, NY 10523

phone: (914) 592-1190

fax: (914) 347-2239

e-mail: alex@hypres.com

Summary

The main goal of the project is designing in RSFQ technology a 20-GHz 8-bit-wide energy efficient processor datapath consisting of an 8-bit ALU, an 8x8-bit Register File, and an Instruction Decoder. We have had several project modifications resulted in additional tasks, such as the development of energy-efficient zero-static-power dissipation SFQ technology, the development of energy-efficient interface based on a low input voltage polarization modulating VCSELs, and the development of superconducting ferromagnetic Random Access Memory.

During the project, we have achieved the following results:

- 1) The VHDL-level design of the 8-BIT datapath was performed in collaboration with SUNY at Stonybrook group. Based on VHDL simulation results, we have designed physical-level layout for HYPRES's standard fabrication process.
- 2) We have designed an 8-bit Arithmetic-Logic Unit (ALU) in RSFQ technology. The design is based on Kogge-Stone CLA adder and employs wave-pipeline architecture. The ALU was fabricated and successfully tested at 20-GHz clock frequency, the major and critical part of the proposed processor datapath. The ALU was fully tested for functionality and operational margins. At low speed, the measured critical margin for bias current was +/- 7%. Using an on-chip test-bed based on the controlled SFQ relays, we have fully tested the ALU at 20-GHz clock frequency.
- 3) We have designed, fabricated, and tested an 8-byte Register File comprising a matrix of two banks of four 8-bit registers integrated with control logic block. The complete 8x8-bit Register File was successfully demonstrated. Besides the data port operation, all 64 memory cells of the register file were tested individually at the nominal bias current. The operational margins for dc bias current were varying from -14% / +25% to -1% / +2%.
- 4) In an additional effort, we have developed a novel resistor-free biasing scheme for RSFQ with zero static- and minimal dynamic power dissipation. We called it energy-efficient RSFQ or ERSFQ. It is fully compatible on a cell level with resistive RSFQ logic allowing us to utilize RSFQ cell library with minor modifications. Using this approach, we have designed and successfully demonstrated at high (up to 60 GHz) speed a number of circuits including a static frequency divider by 2^{20} , a detector digital readout (ADC), and two types of an 8-bit parallel adder. The main achievement in energy dissipation reduction was demonstration of ERSFQ 8-bit parallel adder dissipating 160 aJ per operation. All investigated ERSFQ circuits have shown no performance degradation comparing to their RSFQ counterparts and in some cases even excelled them.
- 5) The 8-bit ALU was designed in new ERSFQ technology. The new ALU architecture is based on wave-pipeline ripple-carry adder featuring high throughput (simulated 44 GHz at 4.5 kA/cm^2 process), asynchronous carry propagation and small latency. At the same time, it operates with high data skew factor that should be matched by the register file.
- 6) The other additional goal of this multi-phase project is to develop and demonstrate the energy-efficient output data interface between cryogenic 4 K superconducting modules and room-temperature semiconductor systems using a combination of energy-efficient on-chip drivers, low loss and dispersion cables, and polarization modulating vertical-cavity emission lasers (PM

VCSELs). During this project period, we completed the fabrication and testing of the second generation designs of PM VCSELs with modifications introduced during the previous project period. This new design is based on a “half-VCSEL” structure with dielectric top distributed Bragg reflector (DBR). We fabricated the first iteration of VCSEL devices with dielectric DBR and demonstrated improvement in performance although with lesser polarization control. The second fabrication iteration to address polarization control is 80% complete. Preliminary testing of these devices before deposition of the top dielectric DBR mirror shows diode current-voltage characteristics, and clear electroluminescence was observed. In addition, we have completed, optimized and employed a cryogenic setup for cryogenic VCSEL testing in wide temperature range. It is based on Sumitomo two-stage cryocooler with accurate temperature control of the first stage. The measurement process and data collection is performed using the developed for the measurements Labview program. We tested a set of VCSEL samples produced by Univ. of Illinois team to verify and calibrate our cryogenic setup. We also fabricated and successfully tested new on-chip energy-efficient driver based on ERSFQ logic. These drivers are based on dc/SFQ converters re-designed to ERSFQ logic. The bias of the driver output stage was implemented via the output data line from the PM VCSEL.

- 7) Another added task was the development of approaches to maximizing energy-efficiency of SFQ digital circuits. We performed the first experimental demonstration of recently proposed energy-efficient single flux quantum logic with zero static power dissipation, eSFQ. We also demonstrate that the introduction of passive phase shifters allows the reduction of dynamic power dissipation by about 20%. Two types of demonstration eSFQ circuits, shift registers and demultiplexers (deserializers), were implemented using the standard HYPRES 4.5 kA/cm² fabrication process.
- 8) The goal of this additional task is to perform development of a 4K Superconducting Ferromagnetic MRAM circuits compatible with Josephson junction digital energy efficient SFQ circuits. A scalable, energy-efficient memory element based on Magnetic Josephson junctions (MJJs) was developed and demonstrated. For SISFS MJJ, we demonstrated the memory properties of two memory states with different critical current values and high $I_c R_n$ comparable to that of conventional SIS Josephson junctions. We have also demonstrated a superconducting ferromagnetic transistor (SFT) – a three-terminal device with good input/output isolation for integration with MJJ-based memory cell capable of performing the memory cell selector function in random access memory arrays.

Table of Contents

I.	Demonstration of RSFQ processor datapath	5
	VHDL-level 8-bit datapath design	6
	RSFQ 8-bit ALU design and demonstration.....	8
	RSFQ 8-byte Register File design and demonstration.....	20
II.	Energy efficiency improvement of SFQ Circuits.....	28
	ERSFQ – Zero Static Power Dissipation RSFQ logic	28
	ERSFQ 8-bit adder family	34
	Redesigning Arithmetic Logic Unit (ALU) in ERSFQ	42
	Investigation of alternative approaches to SFQ energy efficiency (eSFQ).....	48
III.	Energy-Efficient Interface based on Ultra-Low Input Voltage polarization modulating VCSELS	64
IV.	Superconducting Ferromagnetic Random Access Memory Development	78
V.	Conclusion	92

I. Demonstration of RSFQ processor datapath

This project is the first demonstration of the scalable processor microarchitecture suitable for the implementation of wide data path digital circuits.

High-performance computing (HPC) is one of the fields, in which high speed and low power dissipation of superconducting digital circuits has been the motivation for several Josephson microprocessor development efforts following the path established by IBM's famous Josephson project¹. Unfortunately, the requirement of global timing for the superconductor *ac*-powered latching logic, as well as the high power dissipation of the voltage-generating elements of this logic family, along with some other technical obstacles, made the implementation of high-speed processors impossible at tens-of-gigahertz clock rate.

With RSFQ logic², the development of a high-performance superconductor processor became feasible. Non-latching, dc-powered RSFQ logic featuring local and self-timing³ enabled the design of processing modules operating at tens of gigahertz with very low power dissipation. There were two projects for developing a superconductor computer^{4,5,6}. A major part of these projects was the developing an RSFQ microprocessor operating at minimum power while clocking at very high rates.

Until recently, only two 8-bit prototypes of such a microprocessor – FLUX⁵ and CORE⁶ - were developed. Only CORE was successfully demonstrated. And neither of them used true 8-bit wide datapath processing in their pipelines. FLUX microprocessor followed processing-in-registers microarchitecture that allowed eight ALU operations to proceed simultaneously in its datapath, producing up to eight bits per cycle (albeit belonging to different operations). CORE used a simple bit-serial pipeline generating one bit of result per cycle.

The FLUX microarchitecture was able to hide the latency of its eight bit-serial processing pipelines by allowing any instruction to start its execution as soon as the least significant bits of its input operands are calculated. In the bit-serial CORE processor, an instruction needs to wait until all eight bits of its inputs are calculated sequentially.

Although these approaches allowed the design of low-complexity execution pipelines in these first microprocessor prototypes, they are not scalable or applicable to future 32-/64-bit RSFQ processors. The development of a wide-datapath microprocessor is crucial for superconductor-based HPC.

¹ W. Anacker, "Josephson Computer Technology: An IBM Research Project", *IBM Journal of Research and Development*, vol. 24, no. 2, pp. 107-112, Mar. 1980.

² K. Likharev and V. Semenov, "RSFQ logic/memory family: A new Josephson-junction technology for sub-terahertz clock-frequency digital systems", *IEEE Trans. Appl. Supercond.*, vol. 1, pp. 3-28, Mar. 1991.

³ O. A. Mukhanov, S. V. Rylov, V. K. Semenov, and S. V. Vyshenskii, "RSFQ logic arithmetic," *IEEE Trans. Magn.*, vol. MAG-25, no. 2, pp. 857-860, Mar. 1989.

⁴ T. Sterling, "A design analysis of a hybrid technology multithreaded architecture for petaflops scale computation," in *Proc. of International Conference on Supercomputing*, p. 386-296, 1999.

⁵ P. Bunyk, M. Leung, J. Spargo, M. Dorojevets, "FLUX-1 RSFQ microprocessor," *IEEE Trans. Appl. Supercond.*, vol. 13(1), p.433, 2003.

⁶ A. Fujimaki, M. Tanaka, T. Yamada, Y. Yamanashi, H. Park, N. Yoshikawa, "Bit-serial single flux quantum microprocessor CORE," *IEICE Trans. Electron.*, vol. E91-C pp 342-349, Mar. 2008.

1. VHDL-level 8-bit datapath design and verification

VHDL design of the datapath was performed by group of prof. M. Dorojevets of Stonybrook University (Stonybrook, NY) using cell library provided by HYPRES.

The 8-bit datapath consists of three major blocks:

- Instruction Control: Instruction issue & instruction decode units (IIU/IDU)
- Data Storage: Register file (RF)
- Processing: Arithmetic-logic unit (ALU)

The Instruction Issue Unit (IIU) and Instruction Decode Unit (IDU) are responsible for:

- resolving data hazards (data dependencies between instructions),
- fetching instructions from the instruction buffer,
- decoding them into control signals for the datapath.

The IIU consists of a 5-instruction buffer with each instruction containing 20-bits. The buffer is essentially a group of shift registers with a parallel read out.

The IIU also contains an Issue Control Block which resolved data hazards by delaying instruction issue until both source operands for the instruction are calculated. The issuing of instructions is based on a dataflow mechanism. Each instruction has a field that specifies the first instruction in the instruction buffer that needs the instruction's result.

The 8-bit Multi-Port register file stores and delivers data to ALU for further computation. The register file can perform two simultaneous read operations and one write operation from ALU providing that separate source registers are used for each operation.

The 8-bit register file has eight 8-bit registers. Two of the registers are used as input/output left and right ports.

The register file is divided into two banks, providing left and right operands for ALU operations, respectively. The left and right register bits are interleaved, so that the most significant bit from left bank is placed next to most significant bit from the right register bank and so on. This placement is dictated by the ALU layout to provide the smallest data skew on data inputs to ALU.

Six out of the eight registers provide non-destructive data readout. The two I/O ports can be loaded bit-serially from the outside of the chip and read as source data to ALU (with destructive read-out). When written with the results of ALU operations, the I/O ports can be bit-serially read out to the outside of the chip.

The data stored in each of the eight 8-bit registers are read using a "one-hot-encoded" read vector signal. The output of each register bit is merged with corresponding outputs of other registers in the same bank as well as an immediate value from an instruction.

Besides two operands, the ALU opcode and Ready signals are received from the Instruction decode stage and broadcasted to the RF output, one copy for each ALU bit slice.

The register file contains an asynchronous write-back destination register address FIFO which is used to deliver and write data to a destination register when the data and their ready signal from ALU arrive at the write input of the register file. Four register destination addresses received from the Instruction decode

stage can be buffered inside the write-back FIFO, thus allowing up to four outstanding (on-going) ALU operations to be in the state-of-execution within the datapath.

The ALU implements wave-pipelining techniques that allow it to effectively use all of its stages without the need for registers and clocks in between. The major goal is to find efficient design techniques capable of improving the design's performance in terms of latency and rate while tolerating large delay fluctuations in wide datapath circuits. Using the Kogge-Stone adder as a starting point, an ALU has been developed to perform a set of logic operations such as AND, NOR, XOR, XNOR, etc. Additionally, the ALU also has four types of ADD operations namely, normal ADD, ADD with inverted A, ADD with inverted B, and ADD with inverted A and B.

ALU has a latency of approximately 392 ps (also ~eight 20 GHz datapath chip cycles) and an overall complexity of 7,319 JJs. It is capable of running at a maximum rate of ~29 GHz.

The simulations results of the datapath confirm full functionality of all units running together up to ~23.3 GHz (43-ps cycle time). By inspecting the violations log of the simulation, all failed waves are due to timing violations in the write-back destination FIFO within the register file, making it the rate limiting component of the datapath.

Depending on the destination register chosen for an instruction, the full datapath latency can range from ~786 ps up to ~878 ps. Overall, the entire 8-bit datapath has a complexity of ~ 16K JJs.

TABLE II. DATAPATH HARDWARE CONSUMPTION

Datapath Block	Total JJs	%JJs
IIU/IDU	4,467	27.97%
RF	4,390	27.48%
ALU	7,116	44.55%
Total	15,973	100.00%

2. RSFQ 8-bit ALU design and demonstration

Arithmetic Logic Unit (ALU) Chip

Our ALU is based on a Kogge-Stone type adder. Fig. 2.1.1 shows the block diagram of the ALU. It consists of four types of blocks: INIT, ROUT1, ROUT2, and SUM, - connected with passive transmission lines (PTLs). The most important part of the ALU is the INIT block. It

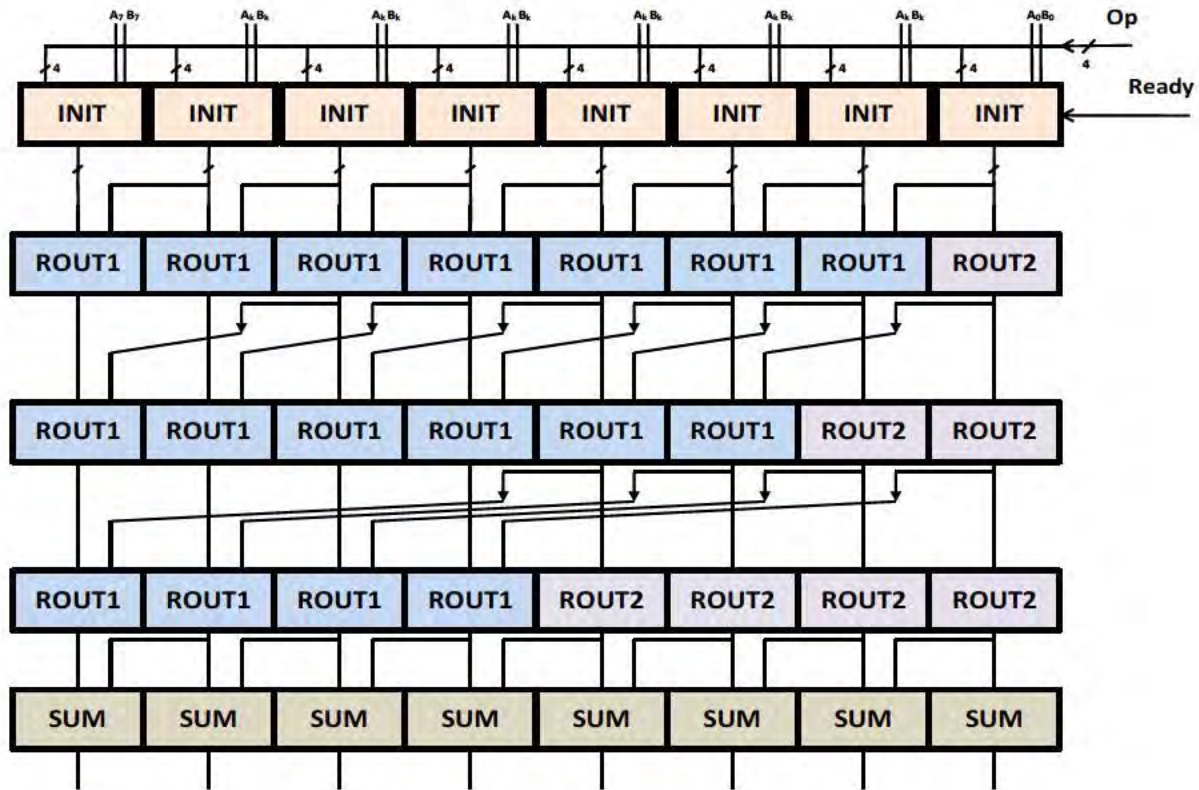


Fig. 2.1.1. Block-diagram of the 8-bit RSFQ ALU.

For testing ALU, we have fabricated two chips, - one is for low-speed functionality test (Fig. 2.1.2) and the other one contains the embedded high-speed test-bed circuitry. Each chip has about 8,000 Josephson junctions (active elements of RSFQ technology).

Chip with 8-bit ALU

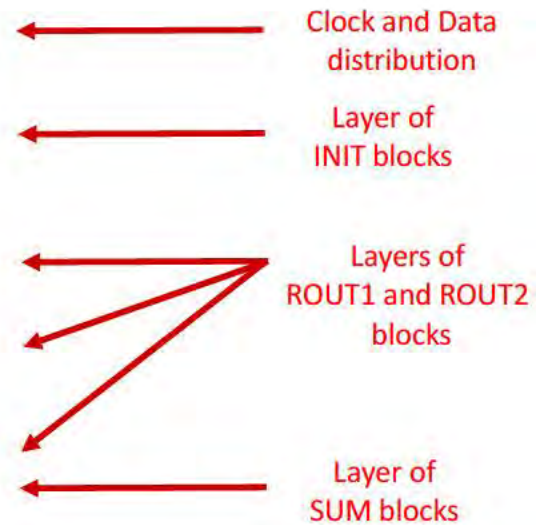
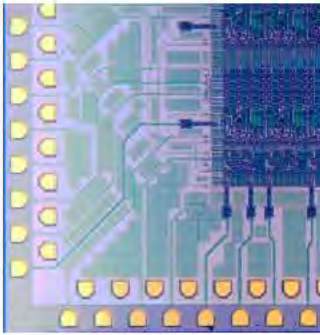


Fig. 2.1.2.4 microphotograph of a chip with 8-bit ALU.

Number of JSs = 7710

The ALU has 12 instructions in its instruction set. They are coded with 4 bit instruction address. This is a complete instruction set that allows programming any logic or arithmetic operation.

Operation	Op3	Op2	Op1	Op0
ADD	1	1	0	0
ADD-Invert A	1	1	1	0
ADD-Invert B	1	1	0	1
ADD-Invert A and B	1	1	1	1
AND	1	0	0	0
NOR	1	0	1	1
Set all bits to "1"	0	0	1	1
AND-Invert A	1	0	1	0
AND-Invert B	1	0	0	1
XOR	0	1	0	0
XNOR	0	1	0	1
NOP	0	0	0	0

Table 1. The instruction set.

In the instruction set of the processor (Table 1), an addition (ADD) function is the most complex and hardware consuming arithmetic operation. This led us to design our ALU based on a parallel adder design.

ALU Functionality Test

W911NF-09-C-0036 ALU Functionality Test

ALU functionality test. A+B

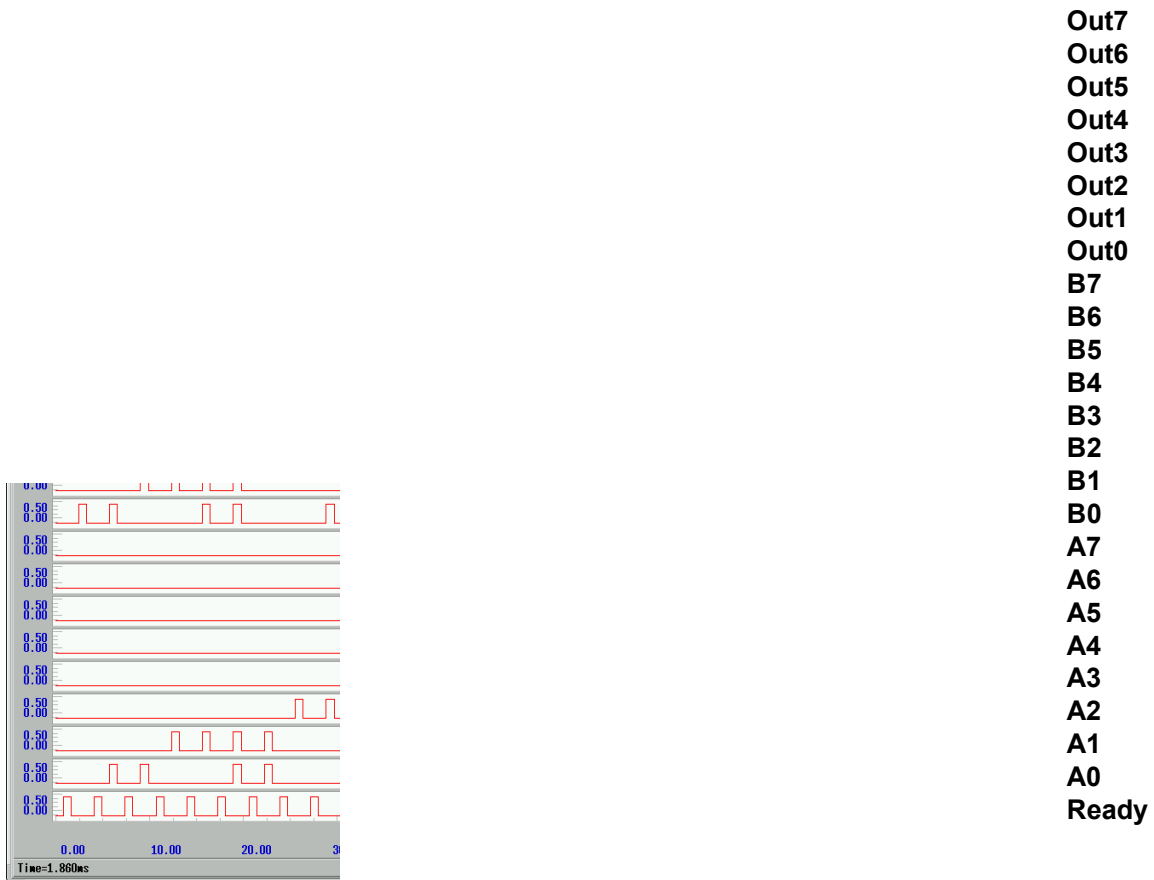


Fig. 2.1.3. ALU functionality test for operation “ADD” {A+B}.

Fig. 2.1.3 shows the correct operation of the ALU adding 8-bit numbers (A+B). The bottom trace is the Ready signal, applied at every instruction execution. The 8-bit operand A, operand B, and the 8-bit output are shown in ascending order. The result of the addition process comes out as modulo 256.

In order to provide subtraction, the ALU can invert one or both operands and add them at a single instruction. The most complex operation in the instruction set is “ADD-Invert A and B”, which is essentially equivalent to the arithmetic operation $(-2-A-B)$. The test result of the ALU performing this operation is shown in Fig. 2.1.4. Here, we have preserved the same order of traces and the same operand pattern as in Fig. 2.1.3.

ALU functionality test. $\sim A + \sim B$



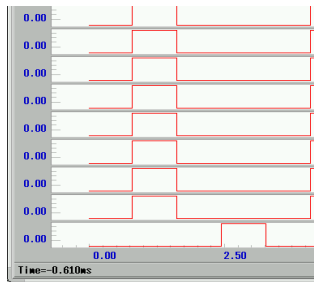
Fig. 2.1.4. ALU functionality test for operation “ADD-Invert A and B” (both operands A and B are inverted before adding) $\{\sim A + \sim B\}$.

The functionally simplest operations are the so-called bit-logic operations, such as AND, XOR, NOR, etc. They do not produce a “carry” bit propagating across the ALU. The results of logic operations performed in the INIT blocks of the ALU (Fig. 2.1.1) go directly to the output. This property of the bit-logic operations simplifies the test pattern necessary to perform a complete test of the ALU.

The low-speed functionality test results for four bit-logic operations are shown: operation AND in Fig. 2.1.5; operation (Inv A) AND B in Fig. 2.1.6, operation A AND (Inv B) in Fig. 2.1.7, operation NOR in Fig. 2.1.8; XOR in Fig. 2.1.9; and XNOR in Fig. 2.1.10. For consistency, we placed the traces in the same order as in Fig. 2.1.3.

The critical (minimal) operating margins on dc bias current were $\pm 7\%$. This is quite sufficient for functioning ALU with acceptable bit-error rate. We plan testing more chips in order to find yield and statistics on operational margins.

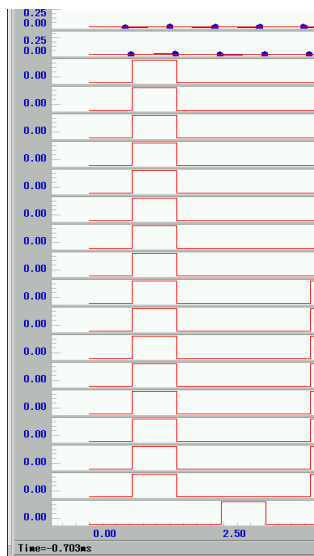
ALU functionality test. A & B



Out7
Out6
Out5
Out4
Out3
Out2
Out1
Out0
B7
B6
B5
B4
B3
B2
B1
B0
A7
A6
A5
A4
A3
A2
A1
A0
Ready

F_i

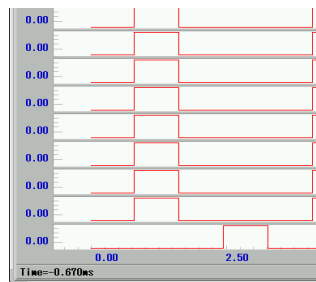
ALU functionality test. $\sim A$ & B



Out7
Out6
Out5
Out4
Out3
Out2
Out1
Out0
B7
B6
B5
B4
B3
B2
B1
B0
A7
A6
A5
A4
A3
A2
A1
A0
Ready

Fig. 2.1.6. ALU functionality test for operation “AND-Invert A” $\{(\sim A) \& B\}$.

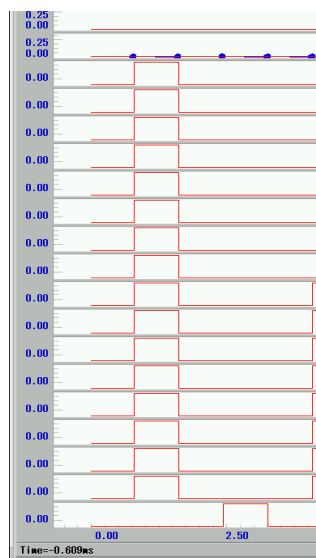
ALU functionality test. $A \& \sim B$



Out7
Out6
Out5
Out4
Out3
Out2
Out1
Out0
B7
B6
B5
B4
B3
B2
B1
B0
A7
A6
A5
A4
A3
A2
A1
A0
Ready

F_i

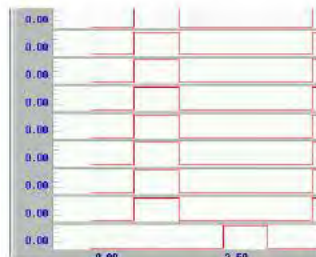
ALU functionality test. $\sim(A|B)$



Out7
Out6
Out5
Out4
Out3
Out2
Out1
Out0
B7
B6
B5
B4
B3
B2
B1
B0
A7
A6
A5
A4
A3
A2
A1
A0
Ready

Fig. 2.1.8. ALU functionality test for operation “NOR” $\{\sim(A|B)\}$.

ALU functionality test. $A \wedge B$



Out7
Out6
Out5
Out4
Out3
Out2
Out1
Out0
B7
B6
B5
B4
B3
B2
B1
B0
A7
A6
A5
A4
A3
A2
A1
A0
Ready

Fi

ALU functionality test. $\sim(A \wedge B)$



Out7
Out6
Out5
Out4
Out3
Out2
Out1
Out0
B7
B6
B5
B4
B3
B2
B1
B0
A7
A6
A5
A4
A3
A2
A1
A0
Ready

Fig. 2.1.10. ALU functionality test for operation "XNOR" $\{\sim(A \wedge B)\}$.

ALU High-Speed Test

The 8-bit ALU has as many as 21 high-speed input- and 8 high-speed output terminals (Fig. 2.1.11). A 20-GHz 20-channel pattern generator capable of producing highly synchronous data streams is not available. It is a common practice to test high-speed digital circuits using on-chip test functions. The test-bed design approach is based on generating operands and control signals from the clock (ready) by means of SFQ relays controlled by dc or low-frequency signals (Fig. 2.1.12). A relay lets an SFQ pulse through when the control current is applied and inhibits it when the current is off.

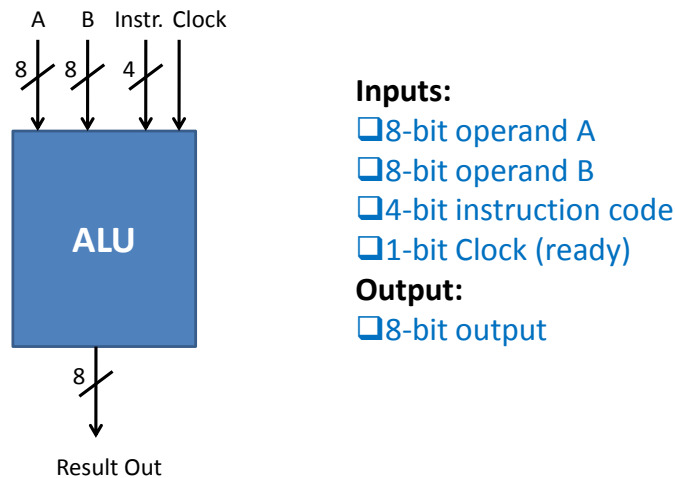


Fig. 2.1.11. The 8-bit ALU I/O count.

The test-bed design approach is based on generating operands and control signals from the clock (ready) by means of SFQ relays controlled by dc or low-frequency signals (Fig. 2.1.12). A relay lets an SFQ pulse through when the control current is applied and inhibits it when the current is off.

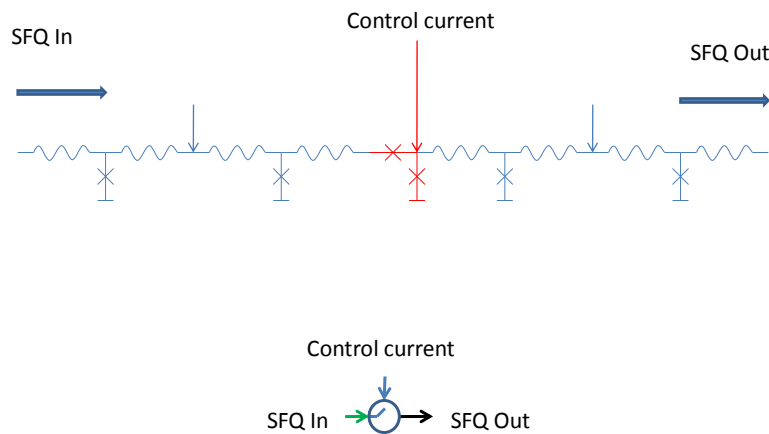


Fig. 2.1.12. Schematics and symbol of an SFQ relay.

We designed a chip for the high-speed test of the ALU. In this chip (Fig. 2.1.13), the high-speed clock (ready) signal is applied to all input data terminals via SFQ relays described above. By

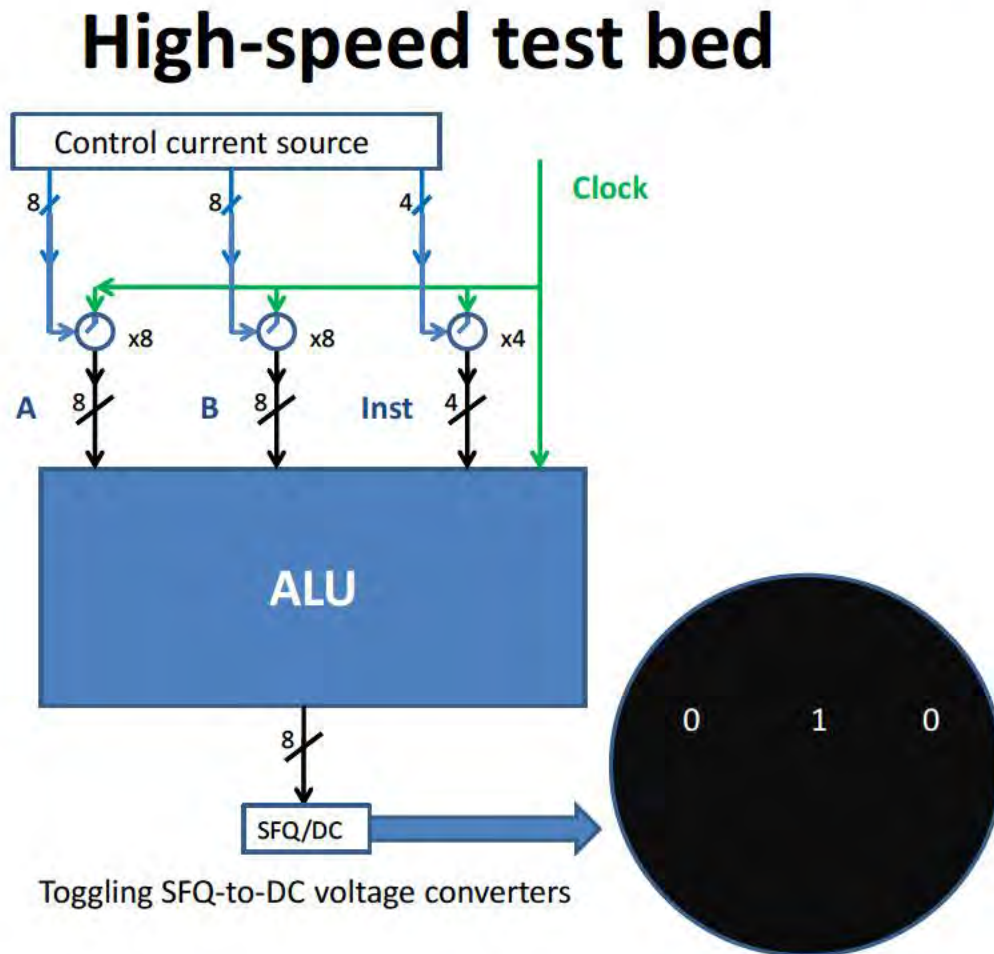


Fig. 2.1.13. Block-diagram of the ALU high-speed test chip.

For the output amplifiers, we used the same toggling-type SFQ-to-DC converters as for the low-speed functionality test. A toggling SFQ-to-DC converter switches its dc-voltage state between 0 mV and 0.5 mV and back every time the SFQ pulse appears. On the low-speed oscilloscope, a 20-GHz output (steady “1”) will be shown as a single line at 0.25 mV (average voltage between two SFQ/DC states toggling at 20 GHz), while the absence of output signal (steady “0”) will appear either as a voltage level of 0.0 mV or 0.5 mV (see the inset in Fig. 2.1.13).

20-GHz ALU operation




A	B	A+B	A&B	A^B	A+B	
(101)	(45)					
1	1					Out0
0	0					Out1
1	1					Out2
0	1					Out3
0	0					Out4
1	1					Out5
1	0					Out6
0	0					Out7
		10010010 (146)	00100101	01001000	10010010	

Fig. 2.1.14. High-speed test of the ALU at 20 GHz. Constant operands and variable instructions.

A typical result of ALU high-speed test is shown in Fig. 2.1.14. Here, we applied constant operands ($A=101$, $B=45$) and varied a 4-bit instruction code. A double line on the picture indicates output “0” and a single line represents output “1”. The 4-bit instruction code (Table I) was controlled by low-frequency pattern generators in order to apply different instructions to the operands A and B. The correct output is shown for addition, logical AND, and logical XOR operations.

The most delay-sensitive operation is an addition, when the carry signal is being generated and propagated along the ALU. In Fig. 2.1.15, we have fixed operand A at value 127 (to avoid modulo 256 arithmetic) and alternated B between 0 and 1. As Fig. 2.1.15 shows, the ALU output correctly switches between values 127 and 128 in accordance with changes of operand B.

ALU operation **A+B**

A	B	B=1	B=0	B=1	B=0	B=1	
(127)	(0/1)						
1	0/1						Out0
1	0						Out1
1	0						Out2
1	0						Out3
1	0						Out4
1	0						Out5
1	0						Out6
0	0						Out7
		128	127	128	127	128	

Fig. 2.1.15. A 20-GHz test for the correct carry propagation in the ALU. Addition of 127 and 1.

The extreme case of addition “255+1” is shown in Fig. 2.1.16. Naturally, in 8-bit logic, number 256 modulo 256 is 0. It shows the correct propagation of carry through the whole ALU, albeit it does not look spectacular. This is the most critical (delay-wise) case among all ALU operations. We measured +/- 5% operating margins on dc bias current. The ALU was operating properly at higher frequencies. It was tested at 23 GHz and, at some operations, up to 33 GHz. Above this frequency, most likely, HF characteristics of the cryoprobe used in the experiment did not allow us to apply undistorted signal.

In order to test bit-error rate, all eight outputs of the ALU were supplied with complementary outputs (inverted data). So, for any operation, we can pick between direct and inverted output for providing the set of eight zeros. In this case, all eight toggling SFQ/DC converters generate no voltage. Switching voltage state of at least one of the 8 outputs indicates an error occurred during ALU operation.

We have observed error-free operation at 20 GHz during 17 minutes. That gives us error rate of $\sim 5 \cdot 10^{-14}$.

ALU operation **A+B**

A	B	B=0	B=1	B=0	B=1	B=0	
(255)	(0/1)						
1	0/1						Out0
1	0						Out1
1	0						Out2
1	0						Out3
1	0						Out4
1	0						Out5
1	0						Out6
1	0						Out7
		255	256	255	256	255	

Fig. 2.1.16. A 20 GHz test for the correct carry propagation in the ALU. Addition of 255 and 1.

3. SFQ 8-byte Register File design and demonstration

One of the major parts of the processor datapath is a Register File (RF). It comprises a matrix of two banks of four 8-bit registers integrated with control logic block (Fig. 1.3.1).

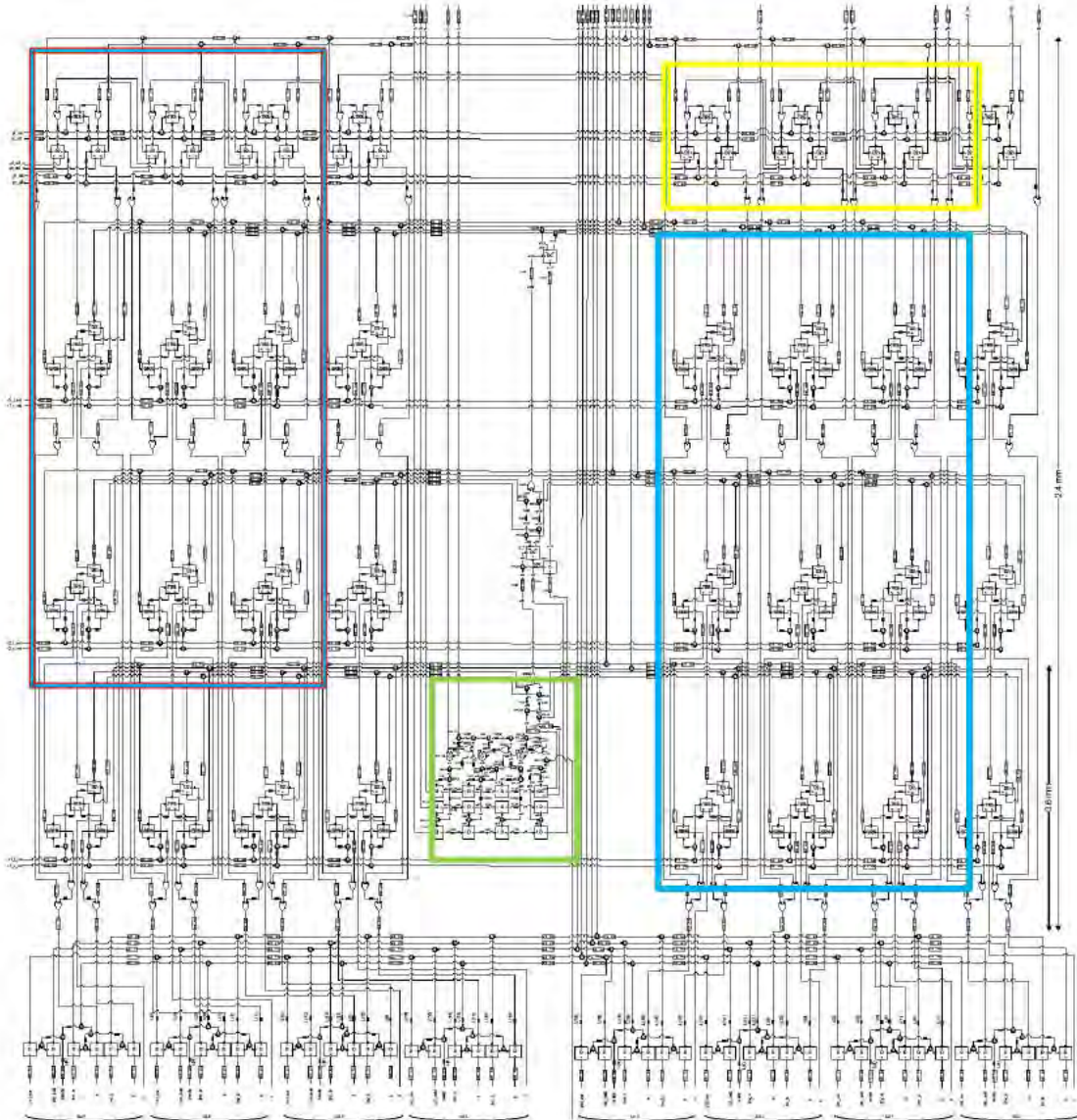


Fig. 1.3.1. Register File cell-level schematics.

We have designed, fabricated, and currently are testing the complete Register File integrated on a 1-cm² chip (Fig. 1.3.2). The chip is designed for standard HYPRES fabrication process. The Register File has been designed in traditional RSFQ technology.

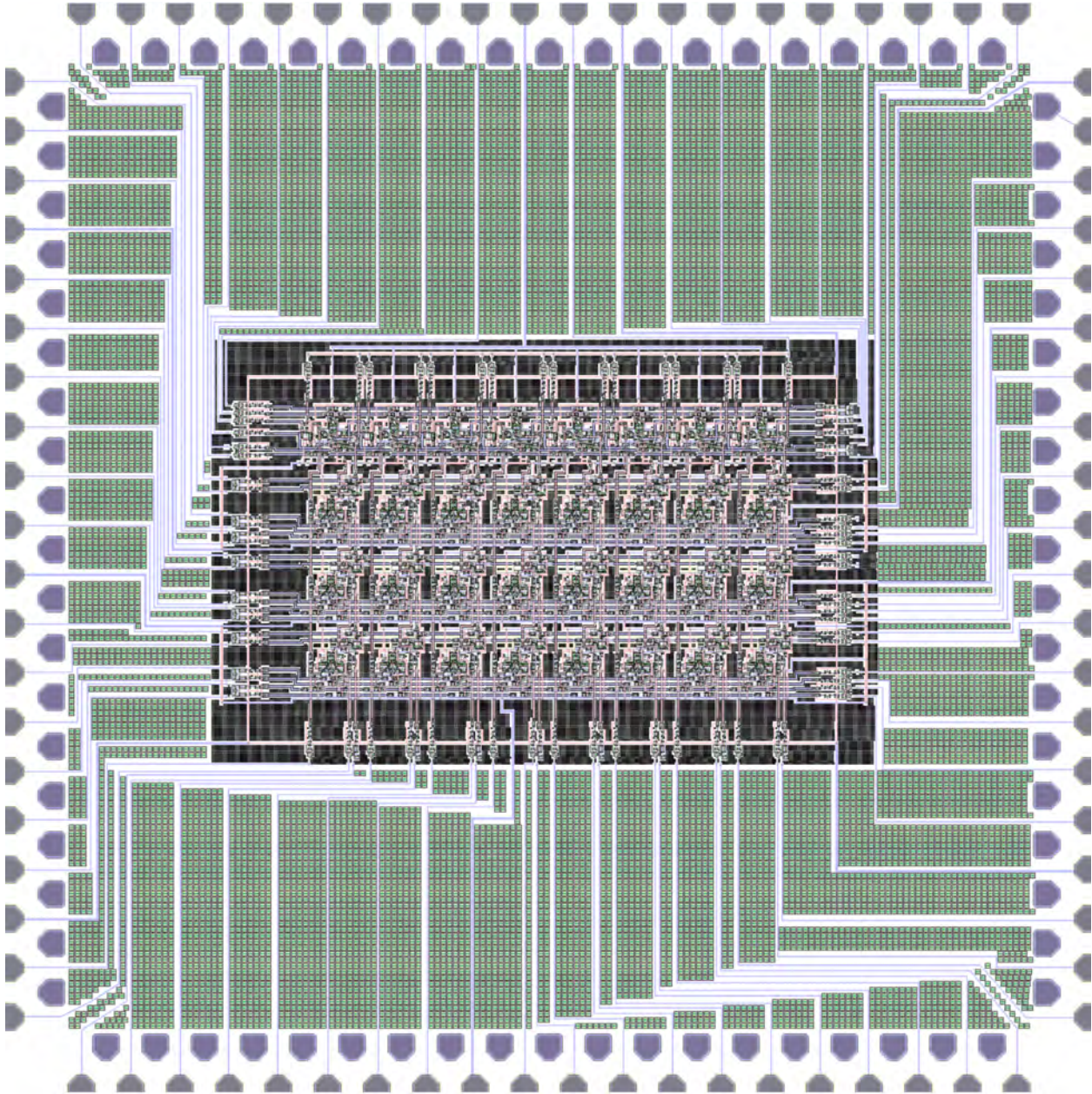
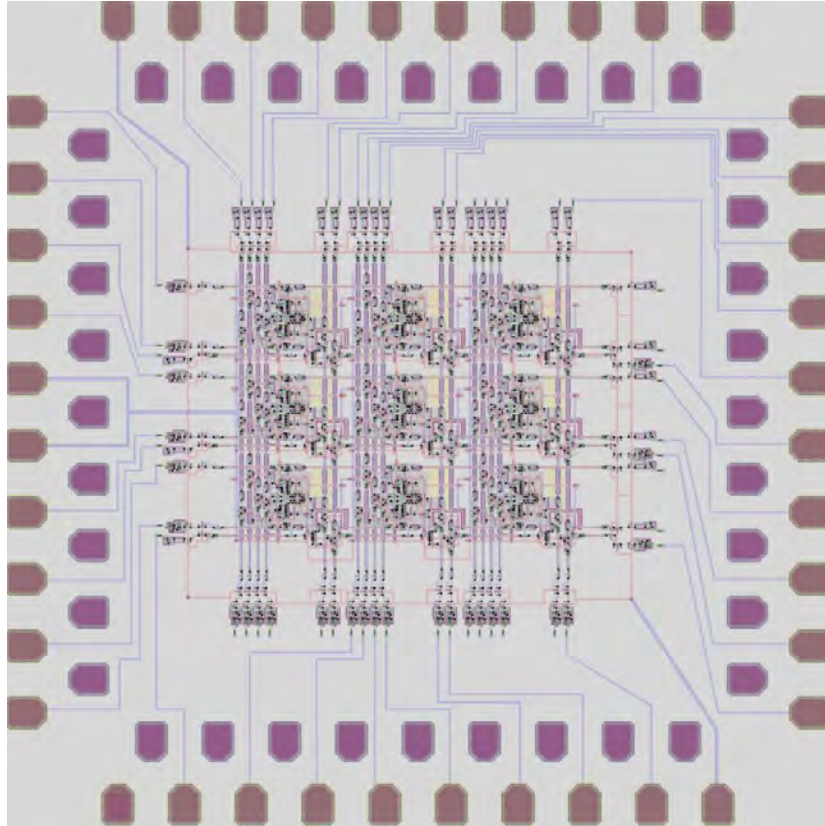


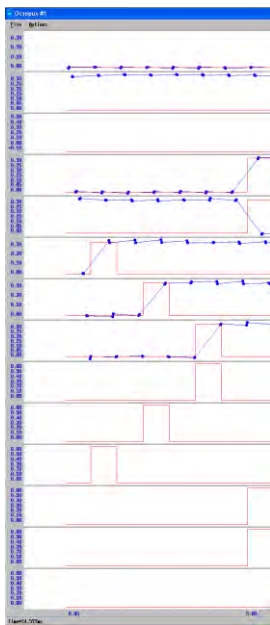
Fig. 1.3.2. The 8-word Register File integrated on a $-cm^2$ chip.

While testing of the whole Register File is in progress, we have successfully tested all critical parts of the circuits. These parts (shown by colored frames in Fig. 1.3.1) were placed on separate chips and tested for functionality. We have performed a comprehensive functionality test using automated test setup.

A successful test of a 3x3 matrix of dual-port memory (blue frame in Fig. 1.3.1) has been reported before. Using this computerized test setup we were able applying the full test pattern to every cell in the matrix, thus measuring operational margins of each out of 9 cells in the fragment. All tested cells worked within $\pm 15\%$ margins on dc bias current (Fig. 1.3.4).



Fi **Functionality test of a Register File block**



Dout_L
Dout_R
Wrt_Data
Read_R_mon
Read_L_mon
Reset_L_mon
Reset_R_mon
Wrt_mon
Wrt
Reset_R
Reset_L
Read_L
Read_R
Bypass

Fig. 1.3.4. Functionality test pattern of a single cell in the 3x3 memory matrix (blue-marked fragment of the register file in Fig.2.1). Operational margins are +/- 15%

The top row of cells (fragment marked with yellow frame in Fig.2.1) has most complicated test logic (Fig. 1.3.5). These memory cells have two ports. Besides parallel connection to the datapath, they are connected in serial providing external data load/unload. We have successfully tested this fragment with operational dc bias current margins $\pm 18\%$.

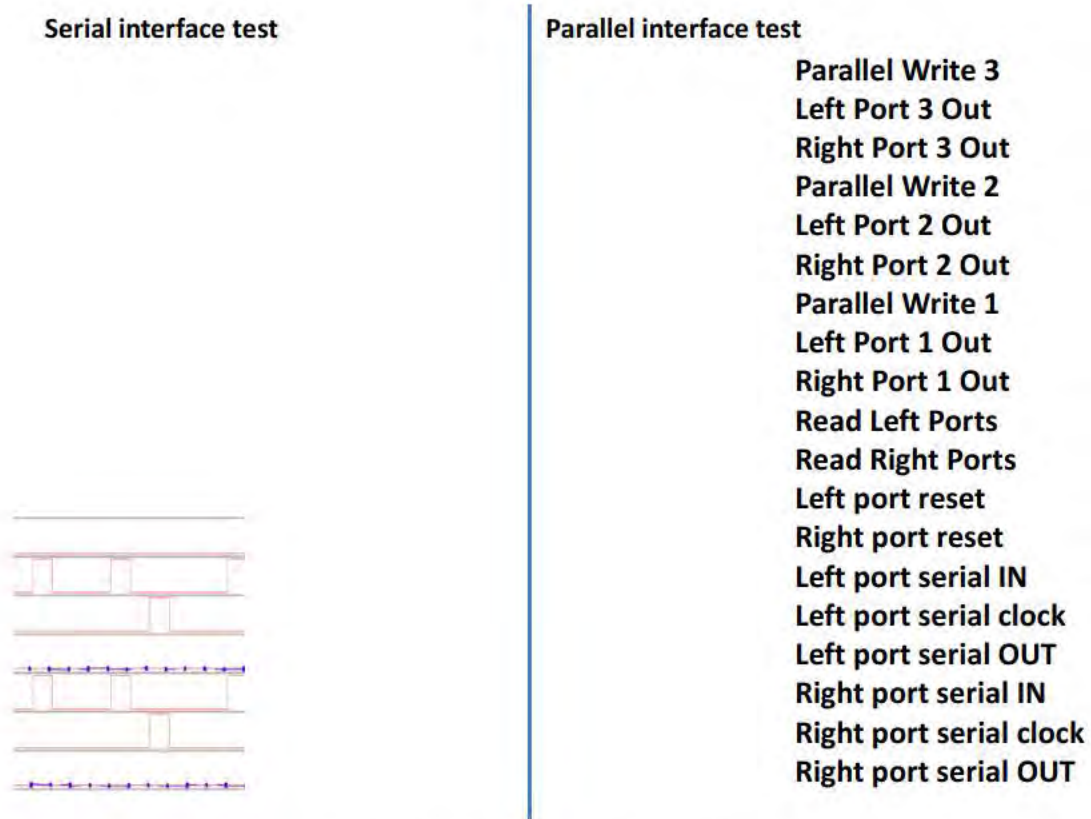


Fig. 1.3.5. Functionality test pattern of a fragment of external port of the register file (yellow-marked fragment in Fig.2.1).

The combination of 3x2 memory matrix integrated with 3 port cells (red-colored fragment in Fig.2.1) has also been successfully tested with operational dc bias current margins $\pm 5\%$.

The complicated test pattern for testing the whole Register File requires two automated test setups working in parallel. We are hoping to get results soon.

Testing of RSFQ 8-word Register File

The requirements to the register file architecture induced by the ALU were an 8-bit word size, 20-GHz throughput, minimal (less than 200 ps) latency, independent read/write access, and a reliable interface to the external memory (for testing). The cell-level design was done by Stony Brook University team using their VHDL-based design flow with HYPRES cell library timing data.

The register file can perform two simultaneous read operations and one write operation from ALU providing that separate source registers are used for each operation where both reads are fetched from distinct register banks (left vs. right). We have designed a register file based on SFQ latches, such as NDRO cell and several flavors of B-flip-flop cell. The designed register file (Fig. 1.3.6) consists of 4 pairs of 8-bit registers that are bit-by-bit interleaved. The top row of the register file in Fig. 1.3.6 consists of dual-port memory cells (D2FF) utilizing one port as a parallel interface to the ALU and the second port as a serial interface to the external memory. The other 3 rows comprise NDRO memory cells with parallel interface to the ALU.

In the middle of the register file, there is a Decode and Control block. It used for buffering destination register addresses and providing control signals that are used for routing write data from ALU to a target destination register. Its FIFO can buffer up to four register write addresses. The control section logic has to be a single block as it contains the critical path of register file. Hence, the register file operating speed depends on the layout of this block.

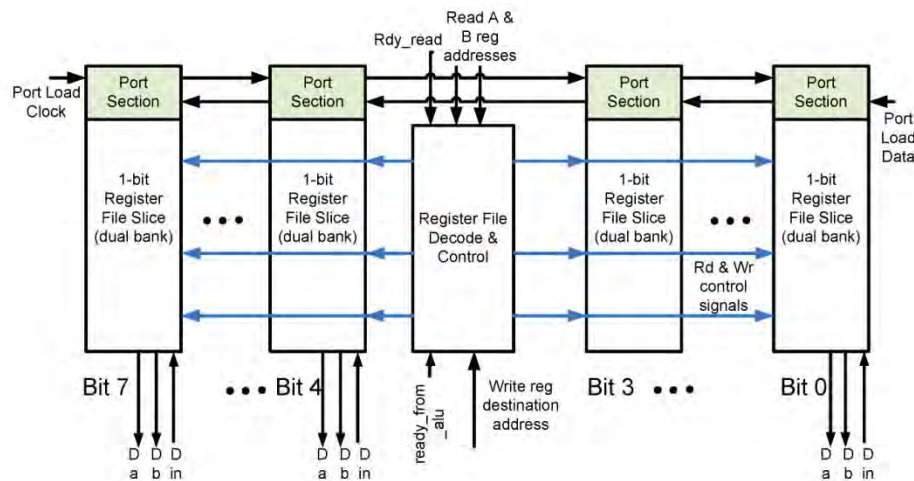


Fig. 1.3.6. Block diagram of the register file.

To simplify the register file design, only one of each pair of left and right registers occupying the same row of each bank can be calculated at any moment. In other words, it is not possible to have two on-going operations, one of which writing to register in the left bank and another - to

register in the right bank. But simultaneous reading from both banks or reading from one bank and writing to the other bank is possible.

The 8x8-bit register file has been designed and fabricated using the standard 1- μm 4.5-kA/cm² HYPRES process. The register file has size of 4.4 mm x 3.0 mm and consists of ~4000 Josephson junctions. The total length of passive transmission lines (PTL) used in wiring is ~0.2m.

We have performed a complete functionality test of the register file without Control block. The control block was successfully tested separately. Due to complicated test patterns, the automated test setup was used for thorough testing of the register file.

Fig. 1.3.7 shows the test pattern for testing serial interface of the right-bank port register. The

ft

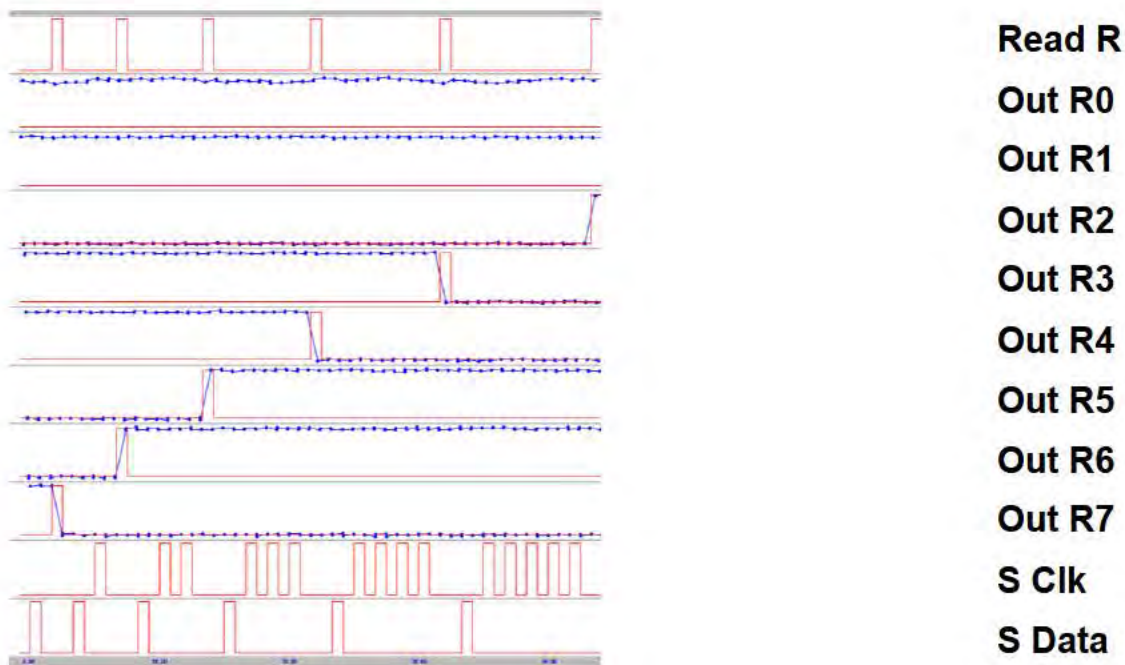


Fig. 1.3.7. Low-speed functionality test of serial interface to the right-bank port register (top row in Fig. 1.3.6).

For testing parallel interface to ALU, we have tested all registers cell-by-cell, accessing them individually. Fig. 1.3.8 shows a typical pattern for testing a memory register cell in row (register) M (0-3) and column (bit) N (0-7). Both (left and right) register banks are tested in this pattern. First, “1” is written down to the left bank, then readout signal verifies content of both NDROs (only left bank reads out “1”); then “1” is written down to the right bank (both banks output “1”);

and finally, “0” is written down to both banks (reset). This is a complete functionality test pattern for registers

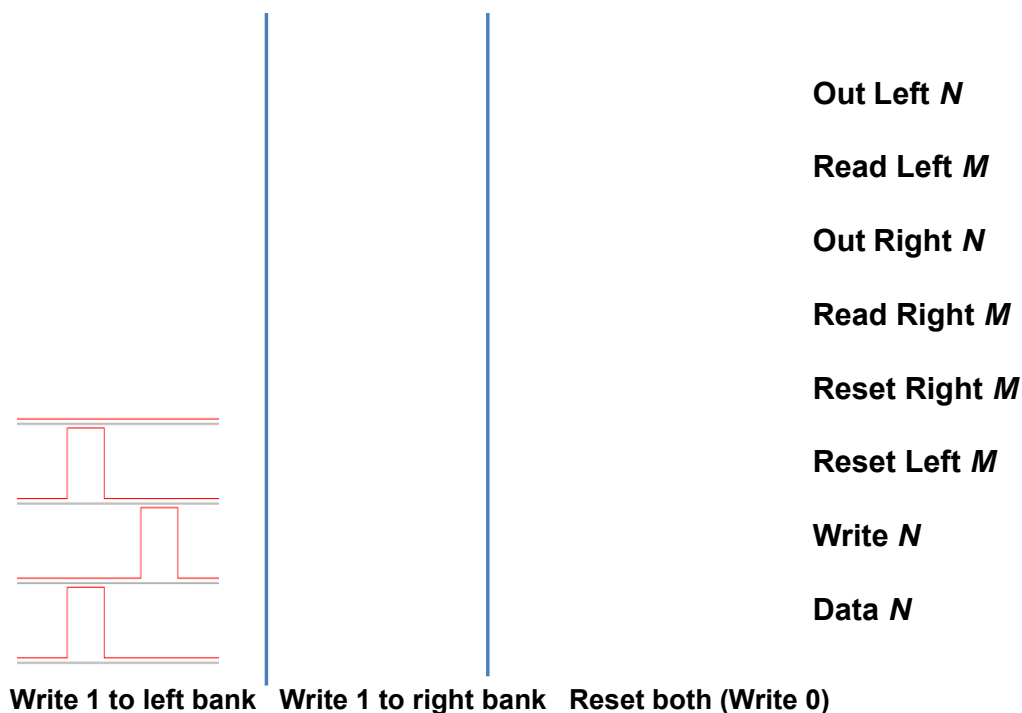


Fig. 1.3.8. Low-speed functionality test of memory register cell located in row M and column N (Fig. 1.3.6). Some of the input signals are not shown for clarity.

With this pattern, we have tested all 24 memory register cells and 8 port register cells consequently. Table 1.3.1 shows the test map, i.e. operational margins (in percent) on dc bias current for each cell, of the register file evaluation.

Reg.	Bit (column number)							
number	0:	1:	2:	3:	4:	5:	6:	7:
0:	-9/+24	-12/+24	-13/+24	-8/+21	-12/+21	-14/+25	-12/+24	-7/+10
1:	-11/+24	-10/+24	-13/+24	-8/+20	-13/+22	-14/+25	-12/+20	-5/+8
2:	-12/+21	-14/+22	-13/+20	-12/+20	-12/+20	-14/+19	-13/+22	-2/+3
3:	-11/+23	-11/+24	-7/+10	-5/+8	-4/+6	-3/+4	-1/+3	-1/+2

Table 1.3.1. Register File Test Map

The margins variation from cell to cell can be caused by many reasons, such as local magnetic flux trapping, external magnetic field, fabrication, etc.

The severe operational margins degradation at the right-bottom part of the array has been caused by proximity of the dc bias current injection point.

II. Energy efficiency improvement of SFQ Circuits

1. ERSFQ – Zero Static Power Dissipation RSFQ logic

Replacing each bias resistor with a Josephson junction as a current distributing element seems to be a natural idea ¹. The Josephson junction's critical current I_c is a natural current-limiting phenomenon. When a shunted ($\beta_c < 1$) Josephson junction is connected to a very small ($V \ll I_c R_n$)

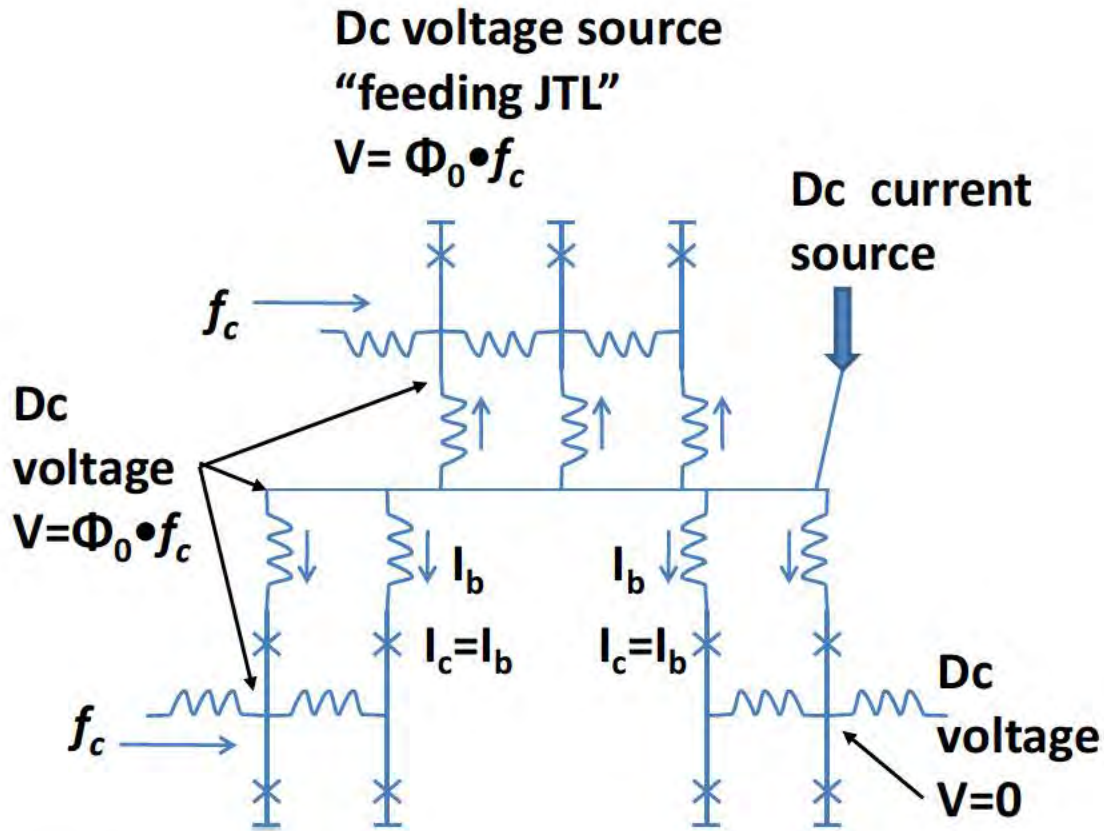


Fig. 2.1.1. The biasing scheme of ERSFQ

The necessary condition of such current distribution scheme is that the voltage on power line should be equal to or greater than the maximum possible dc voltage in the powered circuit. For all RSFQ circuits (with the exception of output amplifiers and some exotic SFQ pulse multipliers²), the maximum possible dc voltage is $V_{max} = \Phi_0 f_{clock}$. In order to create such a voltage source, we use a Josephson transmission line (JTL) biased by common with the circuit

¹ L. Eaton and M. Johnson, "Superconducting constant current source", US Patent #7,002,366, issued Feb. 21, 2006.

² V. K. Semenov, "Digital to analog conversion based on processing of the SFQ pulses", *IEEE Trans. Appl. Supercond.*, vol. 3, pp. 2637-2640, Mar 1993

power line through large superconductive inductors. We call it a “feeding JTL”, for its functionality is to serve as an additional supply of bias current. By applying SFQ pulses from the circuit’s clock source to the feeding JTL, we create an exact dc voltage V_{max} on the bias line.

To prevent dynamic current redistribution and to increase the impedance of the local bias current source, large inductances L_b were serially connected to the bias junctions, providing filtering of the ac components. The maximum bias current dynamic deviation in this case is $\delta I \leq \Phi_0/L_b$. At $L_b=400$ pH, the current fluctuations do not exceed $5 \mu\text{A}$.

The circuit needs to be biased with the dc current value just under the total critical current of bias junctions. So, in the passive state (when the clock is not applied), an ERSFQ circuit does not dissipate any power at all (zero static power dissipation). After turning it on, i.e. applying a clock from the clock source, the total power dissipation of an ERSFQ circuit becomes $P=I_b\Phi_0f_{clk}$, where I_b is the total bias current for the circuit (from the dc current source) and f_{clk} is its operating clock frequency. This is orders of magnitude less than the amount of power dissipated in traditional RSFQ circuits.

Albeit the additional power dissipates in the voltage source (the feeding JTL), its value varies between zero and approximately a quarter of the total power dissipation in the ERSQ circuit. This value depends on the particular design of the circuit. In an RSFQ circuit, clock is transmitted via tree of clock JTLs. These JTLs as good voltage source for power buss as the feeding JTL. To our estimate, in an ERSFQ circuit, the total critical current of all clock JTLs, including the feeding JTL, should be in excess of $\sim 25\%$ of the total dc bias current. Some ERSFQ circuits may not require a feeding JTL at all, maintaining dc bias voltage with their clock-distributing JTLs.

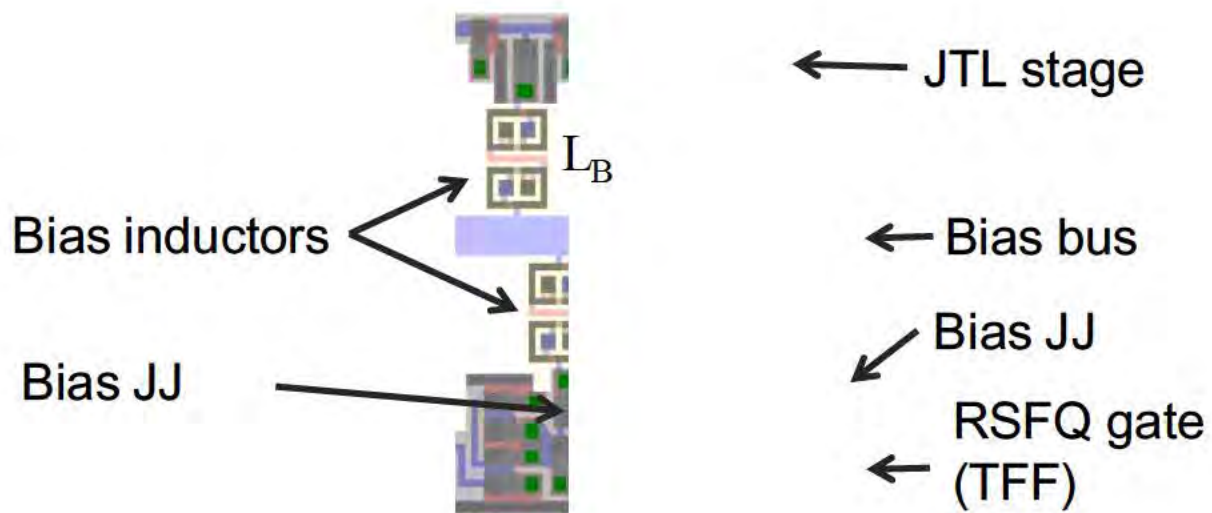


Fig. 2.1.2. A layout fragment of an ERSFQ circuit.

One can easily see large (~ 400 pH) bias inductors consuming substantial space on a chip. Luckily bias inductances are not restricted in value so they can be moved to any place on a

DFFC microphotograph

Lb
Jb



Fig. 2.1.3. Microphotograph of ERSFQ D flip-flop with complementary outputs.

The other drawback of ERSFQ is its expectedly high time jitter due to unavoidable bias current fluctuation is $\delta I \leq \Phi_0/L_b$. The obvious solution to that is increasing value L_b of a bias inductor and generally employing pipeline architecture in designing large circuits. Fig. 2.1.3 shows a microphotograph of the fabricated ERSFQ circuit. In order to obtain large inductance, ground planes were removed from under the inductor.

We have designed and fabricated several chips in order to benchmark ERSFQ technology with logic cells designed in both (ERSFQ and RSFQ) standards. This was done to experimentally verify any differences in operational margins of the two technologies. The output amplifiers have a separate power bus and are designed in standard RSFQ for the obvious reason.

The chip contains two (ERSFQ and RSFQ) versions of a D flip-flop with complementary outputs and two versions of a static frequency divider by 16. For the sake of comparison, both versions of the cells were made using the same design template and look alike (the RSFQ version of each cell was made by replacing bias JJs with resistors in its ERSFQ counterpart). The chip

al
v;

ERSFQ DFFC LF Operation

d



Operating at LF within 22% dc bias margins

Fig. 2.1.4. ERSFQ DFFC gate low-speed test

The functionality test results of a DFFC gate are shown in Fig. 2.1.4. The circuit operated within $\pm 22\%$ bias current margins. The operating region includes the case when the total bias current exceeds the total critical current of bias junction, in which case there is static power dissipation.

ERSFQ Static Frequency Divider by 16

Input

Output



Fig. 2.1.5. **Operating at LF within 26% dc bias margins**

The correct operation of a static frequency divider is shown in Fig. 2.1.5. The ERSFQ version of the circuit was operating within $\pm 26\%$ bias current margins. For some reason, the margins were even higher than those of its RSEFQ counterpart.

ERSFQ Static Frequency Divider by 2^{20}

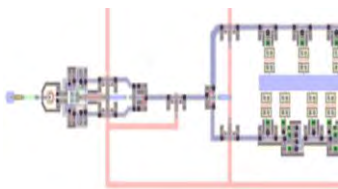


Fig. 2.1.6. ERSFQ static frequency divider by 2^{20} .

An good circuit for verifying ERSFQ approach, - each TFF works at its own frequency

We performed the direct measurements of the bit-error rate (BER). The block diagram of this experiment is shown in Fig. 2.1.7. In this experiment, we used two phase-locked frequency generators; one for the high-frequency clock and the other for the reference signal. The maximum frequency we can apply to the chip through our standard cryoprobe is about 30 GHz. We used an on-chip double-rate converter to double the clock frequency. So, the first stage of the frequency divider could operate at 60 GHz. Then, after dividing by factor of 2^{20} , the signal goes through the output amplifier to an oscilloscope, where it is compared with the reference signal.

The circuit worked correctly at up to 67 GHz of clock frequency within $\pm 16\%$ dc bias current margins. This shows that it could have worked at much higher frequency, and 33 GHz is just a limit of our high-l

At the nominal
signal during ~ 9 h

HF Test of ERSFQ Static Freque

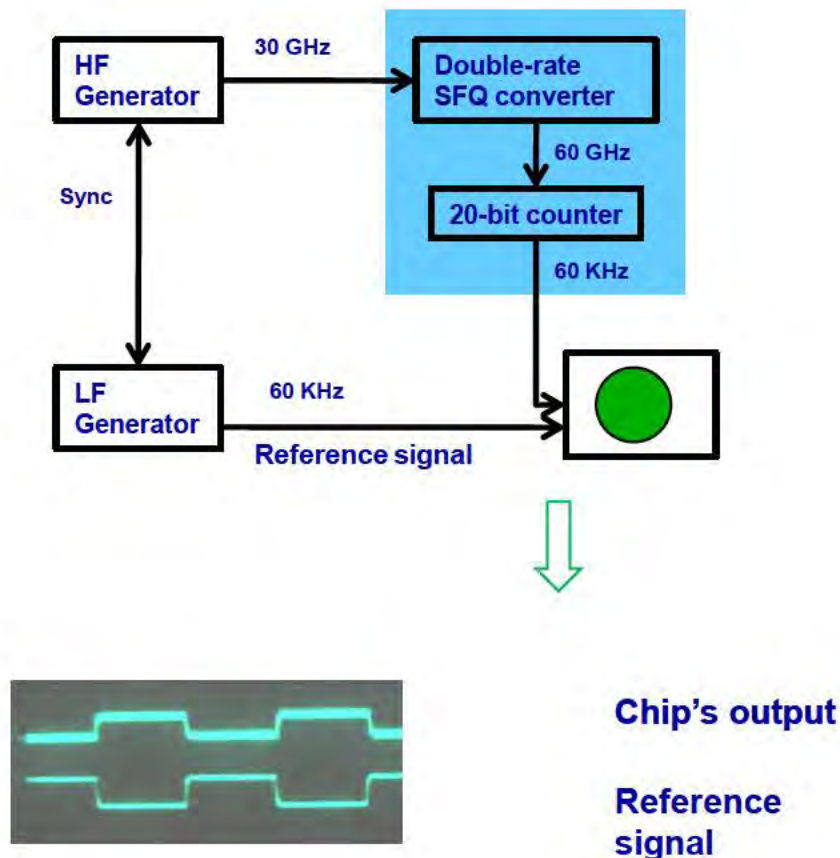


Fig. 2.1.7. Experiment on high-speed BER measurement of ERSFQ static frequency divider by 2^{20} .

2. An ERSFQ 8-bit Adder Family

Using ERSFQ approach, we have designed two versions of an 8-bit parallel adder employing a wave-pipelined architecture. The adders were constructed with an asynchronous-carry half-adder (HA) cell. This cell comprises a hybrid between an asynchronous Mille element and a B flip-flop. It is insensitive to the delay between inputs, allowing high-throughput operation of the adder.

The first design (Fig. 2.2.1) was a most straight-forward approach imposed by the aligned data front requirement (i.e. LSB and MSB should have been produced simultaneously). The second reason was our desire (at the time) to avoid using a merger cell in ERSFQ design. Further on, we will refer to this architecture as an “aligned-front” (AF) adder. In this architecture, clock signal follows the data, resulting in a single-clock operation. For the described above half-adder cell, clock is needed for producing the SUM (XOR) output, while the CARRY (AND) output signal is being generated and propagated asynchronously.

The asynchronous carry propagation and a specially designed clock distribution tree provided, in simulation, a high throughput (up to 30 GHz) with 800-ps latency (at 4.5-kA/cm² process). The adder was designed for 20-GHz target throughput. It consists of 36 Half Adder cells (~2,000 JJs), and dissipates 0.36 fJ per single 8-bit addition operation.

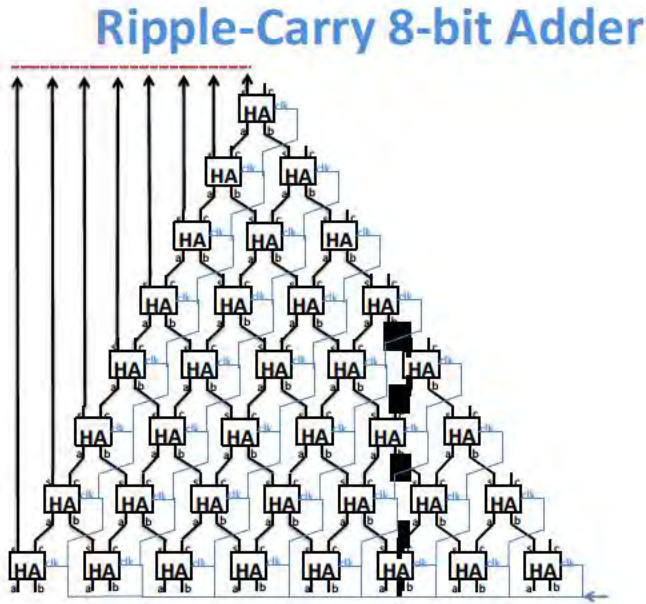


Fig. 2.2.1. Schematics of the “aligned-front” 8-bit wave pipeline adder.

The obvious drawback of this design is its large size. An N -bit AF adder requires $N \cdot (N+1)/2$ half adder cells. This results in a low-scale integration (LSI;) and in a high-value total dc bias current (i.e. power dissipation in ERSFQ).

After solving a problem with an ERSFQ merger cell, we have designed a simple ripple-carry adder (Fig. 2.1.2). In this case, the N -bit adder utilizes only $2 \cdot N$ half adder cells. It still operates in the wave-pipeline mode (i.e. performs single-clock full operation), but requires a heavy-skewed input data front for operating at maximum speed.

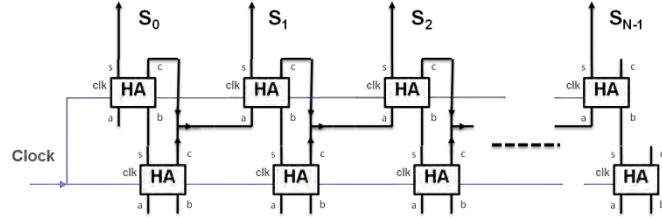


Fig. 2.1.2. Schematics of the ripple-carry 8-bit wave pipeline adder.

For the 4.5-kA/cm^2 fabrication process, the 8-bit RC adder operates at 37-GHz throughput. For the same J_c , the latency between LSB-in and LSB-out is 44 ps, and the total latency (between LSB-in and MSB-out) is 960 ps. The RC adder dissipates only 0.16 fJ per single 8-bit addition operation.

Initially, the 8-bit AF adder was designed and fabricated in old HYPRES's 4-layer $1.0\text{-}\mu\text{m}$ 4.5-kA/cm^2 process. Then, with the successful development of HYPRES's advanced process, we have redesigned the chip with new (6 metal layers, $0.25\text{ }\mu\text{m}$ litho) design rules.

The advanced process allowed scaling down our cell library. This process is especially beneficial for ERSFQ designs. Utilizing two extra wiring planarized layers, we placed all space-consuming bias inductors under the ground plane. This, together with the lithography improvement, results in a seven-fold area reduction of an ERSFQ design.

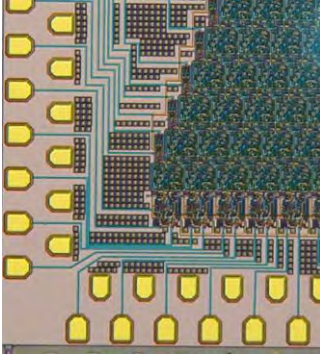
Fig. 2.1.3 shows microphotograph of the 8-bit ERSFQ adder placed on a $5 \times 5\text{-mm}^2$ chip fabricated in standard (a) and advanced (b) HYPRES' process. The difference in the circuit area is 6.6 times.

Standard HYPRES' process:

- 1.0/4.5 kA/cm²
- 4 metal layers
- 1.0 μm feature

Enhanced HYPRES' process:

- 4.5/20.0 kA/cm²
- 6 metal layers
- 0.25 μm feature



a)

6.6 times reduction in circuit area

b)

Fig. 2.1.3. Microphotograph of the 8-bit aligned-front adder on a 5x5 mm² chip fabricated in standard (a) and advanced (b) HYPRES' process.

After that, we have designed a similar adder for HYPRES's 0.25-μm 4-layer process (Fig. 2.1.4a) in order to compare the test results. Thus, the ERSFQ 8-bit adder family has become our benchmark for evaluating a fabrication process.



Fig. 2.1.4. The 8-bit RC adder on a 5x5-mm chip designed for HYPRES's 0.25- μm 4-layer process

The test methodology and test patterns are the same for all flavors of parallel 8-bit adders. Because of that, here, we will describe test procedure without specifying the type of adder. Then, we will report and discuss test results specific for each fabrication process.

The functionality test at low speed allows comparably easy evaluation of a chip for the high-speed test pre-selection. It also provides a valuable feedback to the foundry on the yield.

Using automated test setup, we have performed the complete functionality test of the adder at low speed. We have measured the dc bias current margins for all 2^{16} combinations of arguments A and B of the 8-bit adder. This comprehensive test takes a long time and has to be run overnight. Later, we have decided, that testing critical carry patterns only would be sufficient for the functionality test.



Fig. 2.1.5. Functionality test of the 8-bit ERSFQ adder.

An ostentatious test pattern is shown in Fig. 2.1.5. This pattern has been created for the sake of visualization of the adder functionality.

In order to perform high-speed test, we used built-in switch-based test bed. This approach also allows us to measure the bit-error rate of the circuit at high speed. The idea is to produce input data signals by passing clock pulses through SFQ relays controlled by external dc current. If the control current is ON, the clock pulse passes through the relay, providing “1” on the corresponding input, and “0” otherwise. Thus we can apply the same input pattern repeatedly at a high-speed clock rate. The output data stream is monitored on toggling-type SFQ-to-DC converters. When the output is “0” (no pulses coming to the converter), the output will be a static voltage level (0 or V_{\max}). If a high-speed stream of SFQ pulses is coming to the converter, it oscillates with the clock frequency resulting in average voltage level between two voltage states ($\sim V_{\max} / 2$). On the oscilloscope, the first (“0”) case will be represented with a double line, and the second (“1”) – as a single “fat” line. Not every circuit can be tested with this method, but the parallel adder is quite suitable for this.

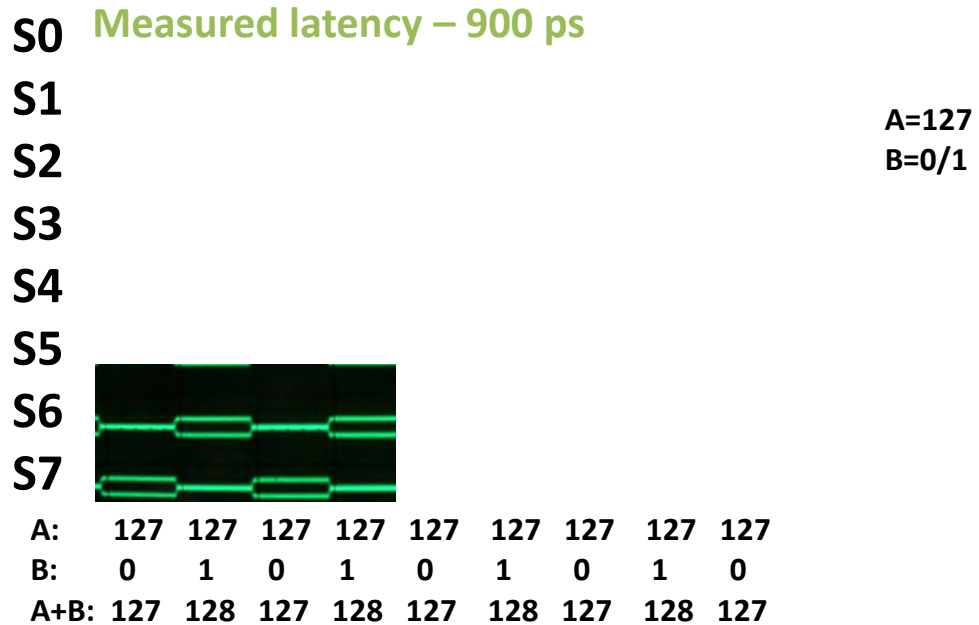
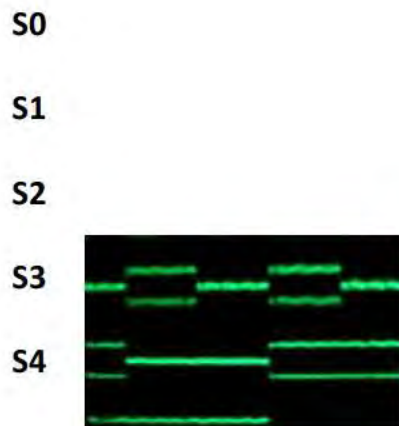


Fig. 2.1.6. A 20-GHz test of the 8-bit ERSFQ adder. Argument A is 127, while B is alternating 0 and 1.

Using this technique, we have performed various tests. The most critical timing-wise parallel adder operation is a CARRY propagation throughout the whole circuit. In case of 8-bit parallel adder, this is operation “255+1” or “127+1”. Fig. 2.1.6 shows the correct work at 20 GHz at alternating operations “127+0” and “127+1”.

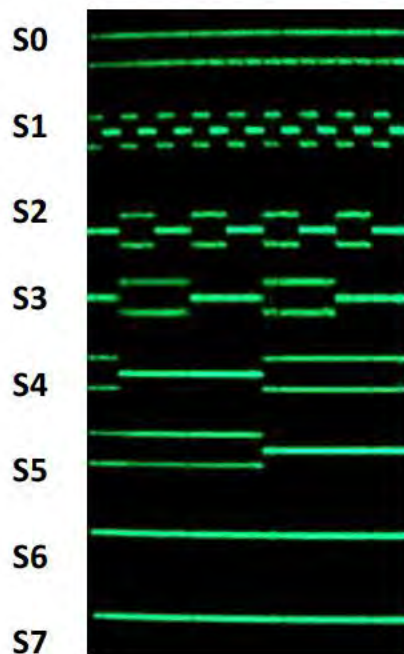
The more visually interesting pattern is the pattern with all possible 8-bit numbers. The test results of such pattern require a complicated interpretation. Fig. 2.1.7 illustrates how to apply any 8-bit number pattern simply using 8 synced generators. Here, one of the adder arguments is equal to 0, while the other scans through all possible 8-bit numbers. So, the operation shown in Fig. 2.1.7 is $A+0=A$ for all 256 combinations. After applying argument B, as alternating “0” and “1”, we have obtained Fig. 2.1.8. The arrow points at the correct operation “127+1”.

All 256 8-bit numbers are assigned to A, B=0



ERSFQ 8-bit Adder 20-GHz test

Addition of A and alternating B (0/1)



One LSB period

Fig. 2.1.8. A 20-GHz test of the 8-bit ERSFQ adder. Argument A consequently takes all 256 numbers, while B is alternating 0 and 1.

Using a high-frequency oscilloscope, we have directly measured latency of the AF adder. The delay between clock and the output signal is 900 ps. That is slightly larger than predicted by simulation (800 ps).

The structure of RSFQ logic allows a quite simple measurement of the power dissipating by an ERSFQ circuit. All RSFQ circuits are biased with the current from an external dc current source. Therefore, the dissipating power equals to a product of the dc bias current value and the measured average voltage on the bias line. Naturally, the measured voltage depends on the clock frequency of the circuit. In case of ERSFQ, it is a direct Josephson relation ($V = f_{clk} \cdot \Phi_0$). Fig. 2.1.9 shows the results of such measurement for both AF and RC adders. The experimental results are in ideal agreement with theoretical prediction. As can be seen, the power dissipation of the AF adder at 20 GHz is $\sim 7.2 \mu\text{W}$. That gives us the theoretically predicted 0.36 fJ per single clock. tal bias
current ($\sim 3.2 \mu$

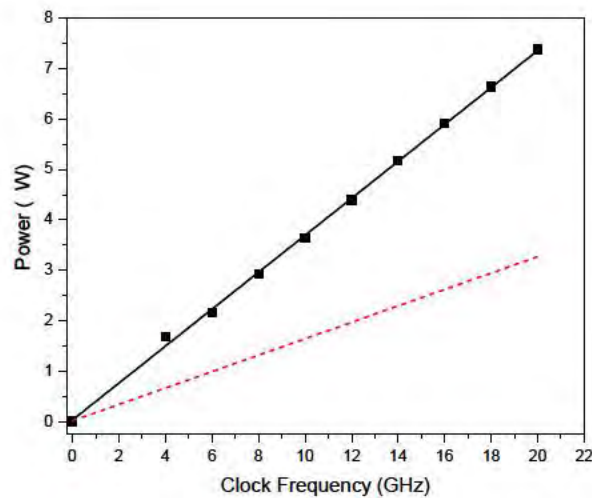


Fig. 2.1.9. Experimentally measured power dissipation of the 8-bit ERSFQ AF (solid line) and RC (dashed line) adders vs. operating frequency.

3. Redesigning Arithmetic Logic Unit (ALU) in ERSFQ

While redesigning the existing Kogge-Stone adder based 8-bit ALU in ERSFQ technology, we have encountered a problem with the size of its physical layout. The size of the ALU was too large to be integrated with the Register File and the Instruction Decoder on one chip. So, we have faced the necessity of changing ALU architecture to more compact version without losing its performance and with the same specifications.

The previous ALU architecture (developed by subcontractors from Stony Brook University) was based on a Kogge-Stone type adder (see previous progress reports). The advantages of this

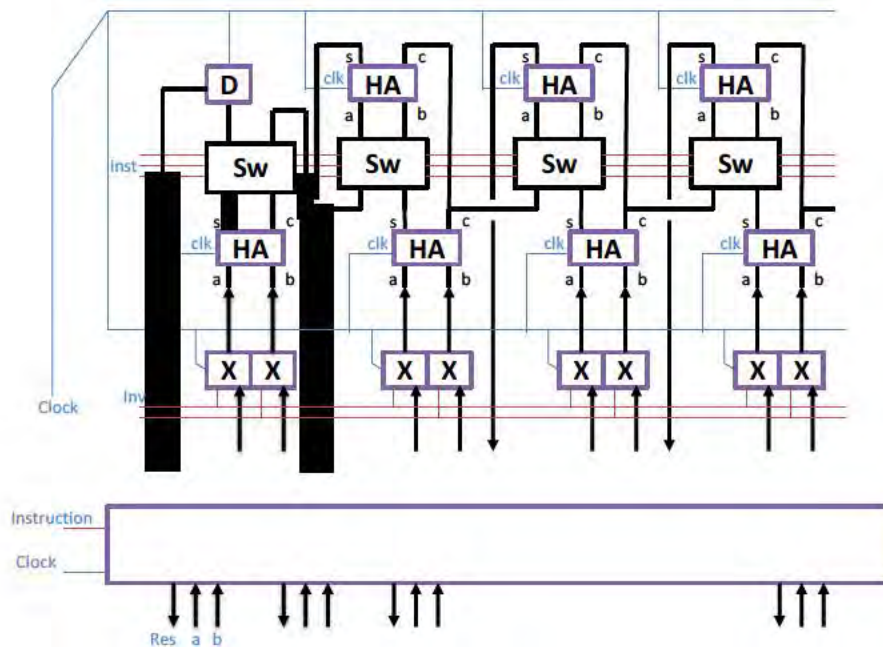


Fig. 2.3.1. Block-diagram of the 8-bit ERSFQ ALU.

The base element of the ALU is an ERSFQ Half Adder cells (Fig.1.2). This cell has been successfully used in ERSFQ 8-bit adder, in DSP processor, and in various ADCs. The main feature of this cell is its asynchronous Carry signal. Meaning, a Carry signal is not being latched to a Clock signal and is being produced as soon as the second argument “1” is arrived before the Reset (clock). This property allows us propagating Carry signals in a form of a wave.

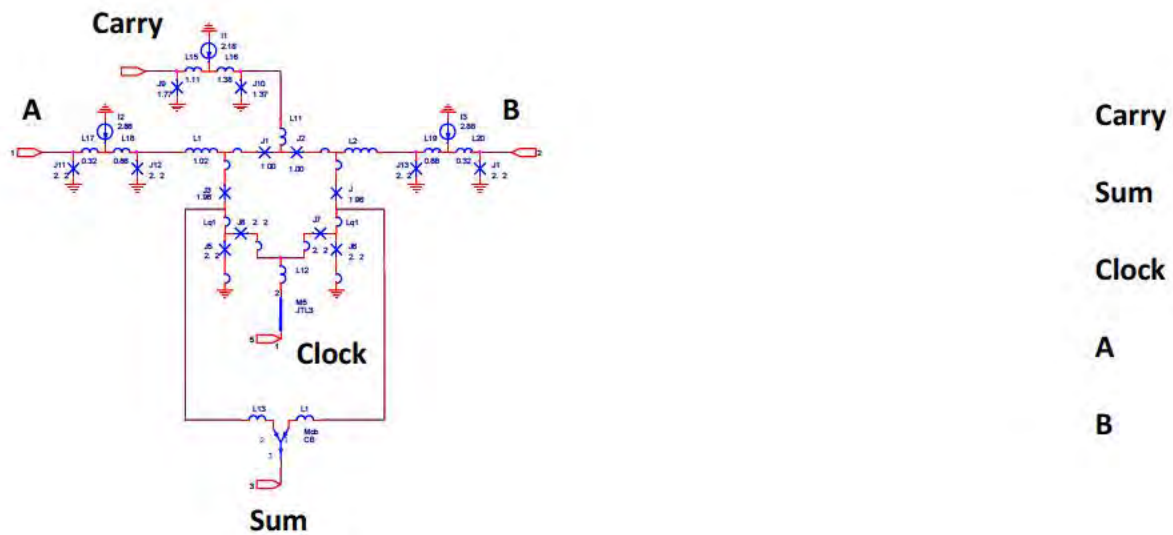


Fig. 2.3.2. ERSFQ Half Adder cell. Schematics and functionality test.

The instruction select is achieved by a switch cell that relays Sum and Carry signals from the first stage of Half Adders to the second stage. This simple routing provides execution of such instruction: the operands, this gives

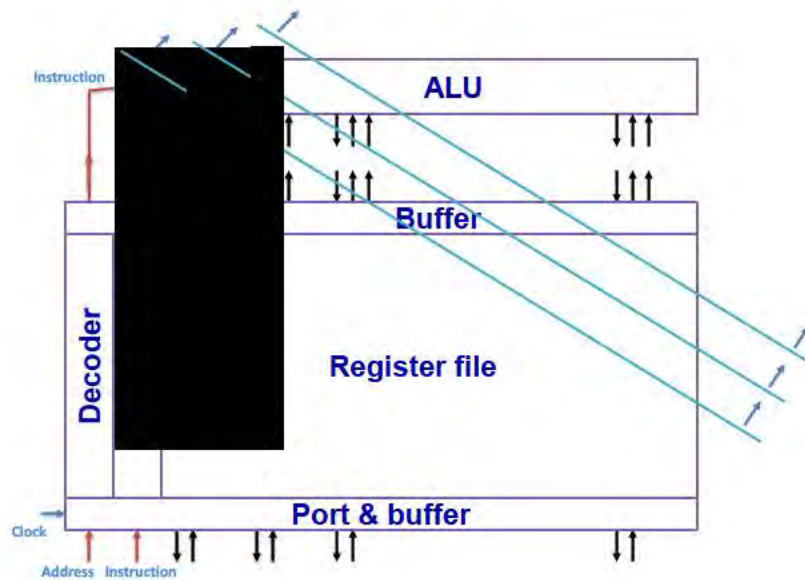


Fig. 2.3.3. The ERSFQ processor datapath timing scheme.

In the new ALU architecture (Fig. 2.3.1), we exploited advantages of local timing featuring RSFQ technology. The idea of new wave-pipelined ERSFQ ALU is in propagating an instruction code and a clock signal in sync from LSB to MSB of the operands. The same

“skewed” approach (Fig. 2.3.3) is used in reading from and writing to a register as well, providing extremely high throughput. A small “vertical” size of the ALU, i.e. a short distance between input and output terminals, provides very low latency (simulated - 80 ps). Here, under “latency”, we assume a “turnaround” time between the start of loading operands LSBs and receiving a result LSB. The wave propagation time from LSB to MSB is 400 ps for the 8-bit ALU, but it does not affect the Datapath performance and therefore should not be regarded as ALU latency. The simulated throughput of the 8-bit ALU is 44 GHz in 4.5-kA/cm² fabrication process.

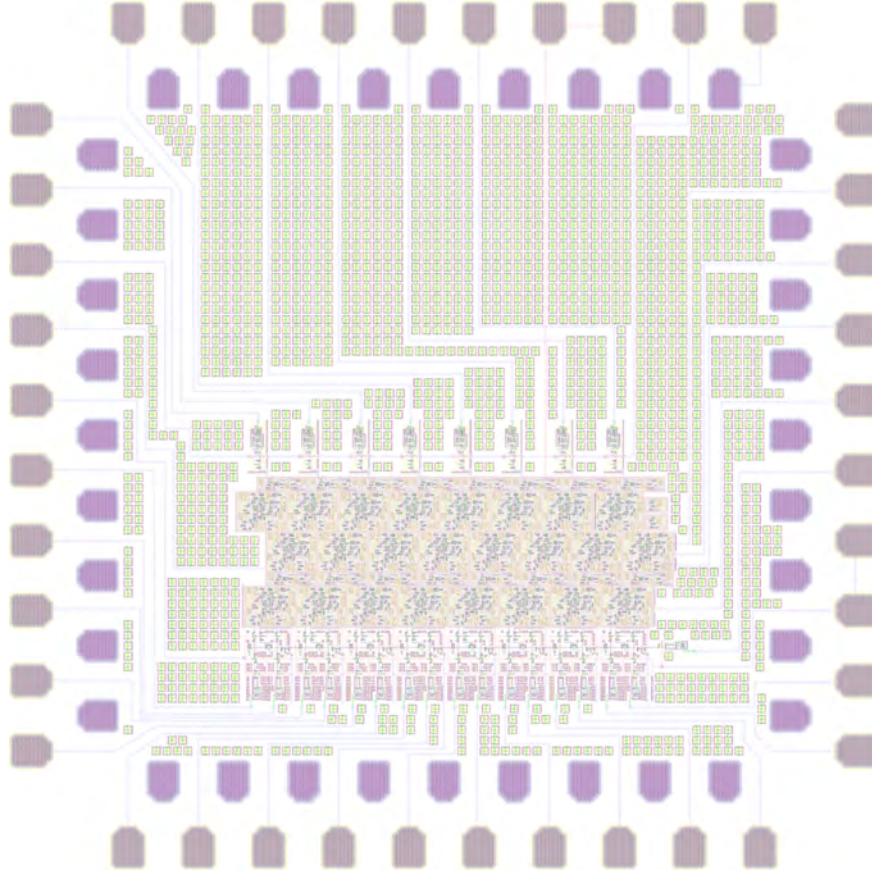


Fig. 2.3.4. A 5x5-mm chip with the prototype of 8-bit ERSFQ ALU.

Finally, we have designed an 8-bit ALU prototype on a 5 mm by 5mm chip (Fig. 2.3.4). The size of the ERSFQ ALU is three times smaller than the size of previous RSFQ 8-bit ALU, although ERSFQ cells occupy more room than their RSFQ counterparts, because of the biasing scheme.

I. Redesigning Arithmetic Logic Unit (ALU) in ERSFQ

While redesigning the existing Kogge-Stone adder based 8-bit ALU in ERSFQ technology, we have encountered a problem with the size of its physical layout. The size of the ALU was too large to be integrated with the Register File and the Instruction Decoder on one chip. So, we have faced the necessity of changing ALU architecture to more compact version without losing its performance and with the same specifications.

The previous ALU architecture (developed by subcontractors from Stony Brook University) was based on a Kogge-Stone type adder (see previous progress reports). The advantages of this

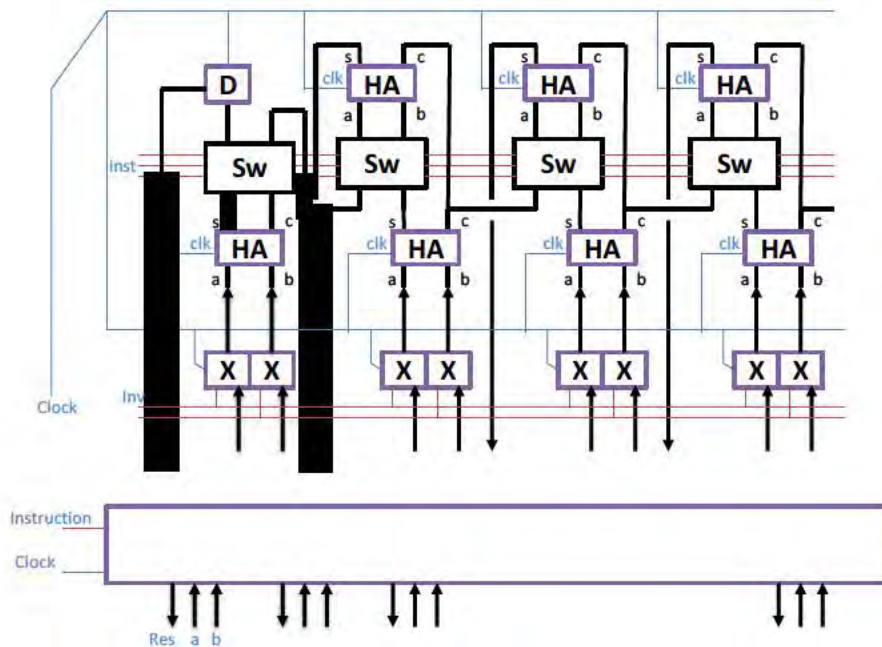


Fig. 2.3.2. Block-diagram of the 8-bit ERSFQ ALU.

The base element of the ALU is an ERSFQ Half Adder cells (Fig.1.2). This cell has been successfully used in ERSFQ 8-bit adder, in DSP processor, and in various ADCs. The main feature of this cell is its asynchronous Carry signal. Meaning, a Carry signal is not being latched to a Clock signal and is being produced as soon as the second argument “1” is arrived before the Reset (clock). This property allows us propagating Carry signals in a form of a wave.

“skewed” approach (Fig. 2.3.3) is used in reading from and writing to a register as well, providing extremely high throughput. A small “vertical” size of the ALU, i.e. a short distance between input and output terminals, provides very low latency (simulated - 80 ps). Here, under “latency”, we assume a “turnaround” time between the start of loading operands LSBs and receiving a result LSB. The wave propagation time from LSB to MSB is 400 ps for the 8-bit ALU, but it does not affect the Datapath performance and therefore should not be regarded as ALU latency. The simulated throughput of the 8-bit ALU is 44 GHz in 4.5-kA/cm² fabrication process.

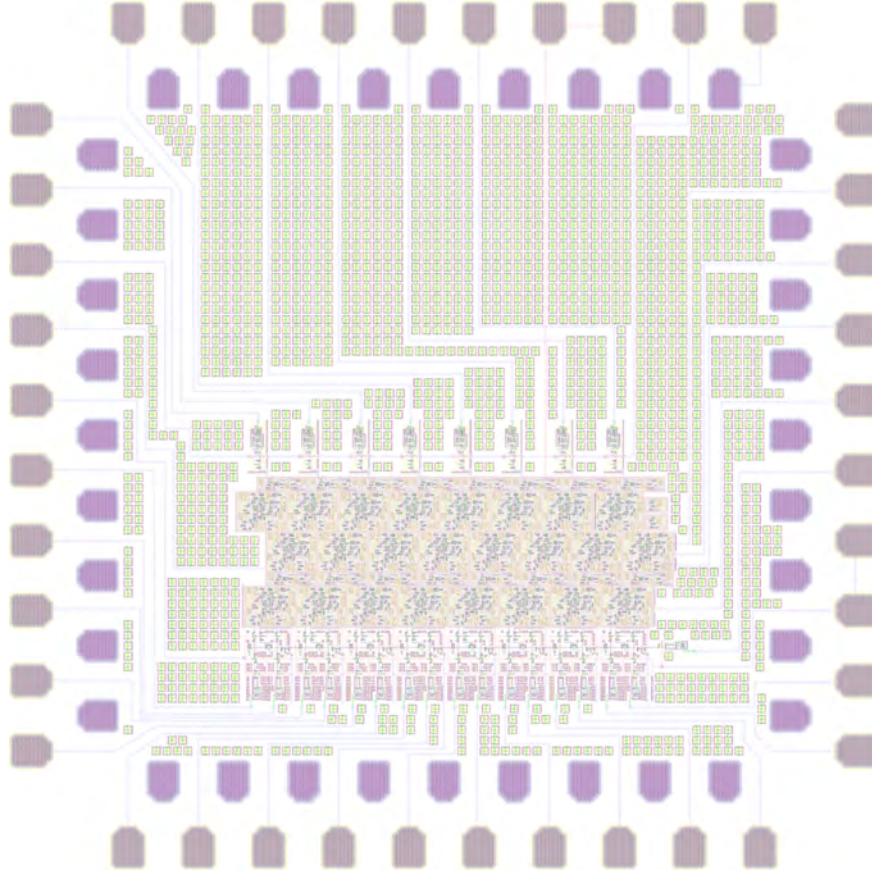


Fig. 2.3.4. A 5x5-mm chip with the prototype of 8-bit ERSFQ ALU.

Finally, we have designed an 8-bit ALU prototype on a 5 mm by 5mm chip (Fig. 2.3.4). The size of the ERSFQ ALU is three times smaller than the size of previous RSFQ 8-bit ALU, although ERSFQ cells occupy more room than their RSFQ counterparts, because of the biasing scheme.

4. Energy Efficiency Maximization of SFQ Circuits

Summary:

During this project period, we were developing approaches to maximize energy-efficiency of SFQ digital circuits. We performed the first experimental demonstration of recently proposed another energy-efficient single flux quantum logic with zero static power dissipation, eSFQ. We also demonstrate that the introduction of passive phase shifters allows the reduction of dynamic power dissipation by about 20%, reaching ~ 0.8 aJ per bit operation. Two types of demonstration eSFQ circuits, shift registers and demultiplexers (deserializers), were implemented using the standard HYPRES 4.5 kA/cm^2 fabrication process.

Scope

In this project, we achieved the first experimental demonstration of eSFQ circuits including shift registers and demultiplexers. These eSFQ circuits make use of superconducting dc bias current dividers and thus avoid static power dissipation. Until recently, this was considered impossible in RSFQ-type circuits, since it would lead to superconducting phase and average voltage imbalances caused by data SFQ propagation in superconducting Josephson circuits. In eSFQ circuits, all RSFQ core advantages of high-speed, dc power, internal memory, local clock control along with the already developed RSFQ circuit designs are largely preserved. The elimination of static power dissipation in eSFQ circuits results in over two orders of magnitude reduction of overall circuit power as compared to conventional RSFQ circuits.

We also were able to reduce dynamic power dissipation of SFQ gate. This is achieved by employing passive superconducting phase shifters resulting in reduction of circuit bias current and, thus, dynamic power dissipation. Furthermore, since the eSFQ circuit dc bias is controlled by the SFQ clock, one can manage dynamic power by managing the distribution of SFQ in the clock network. It is possible to turn off the SFQ clock for a particular part of a processor and effectively stop the circuit operation, i.e. achieve zero dynamic power, while maintaining the internal state of the affected circuit. This feature is compatible with the coveted goal of achieving energy-proportional computing as the ultimate energy-efficient machine.

Design of eSFQ demonstrator circuits

Most RSFQ circuits are generally well-suited to conversion to eSFQ. D-cell (D flip-flop) conversion from RSFQ to eSFQ is depicted in Fig. 2.4.1. Conventionally, the D-cell is biased so that it initially stores a logic “0”. Such biasing occurs on junction J_1 , which only experiences a π phase increment when a pulse arrives at In . However, exactly one pulse arrives at $Clock$ during every clock period, ensuring a 2π phase increment across the Decision Making Pair (DMP). Hence, for eSFQ, the bias injection point is moved to the DMP. As a side effect, the converted D-cell stores a logic “1” after initial bias ramp-up.

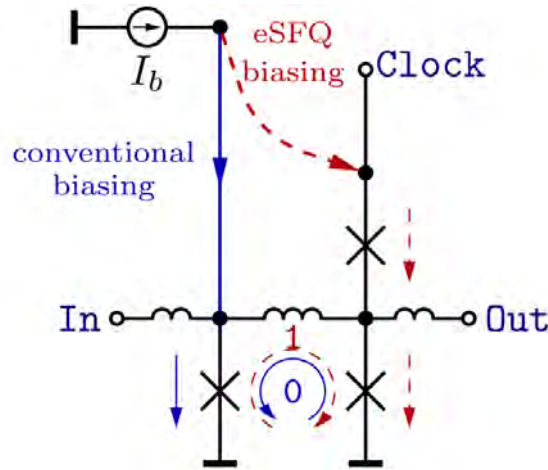


Fig. 2.4.1. Conversion of standard RSFQ D flip-flop to eSFQ.

We chose two circuits for the first experimental demonstration of eSFQ approach: a shift register and a demultiplexer (deserializer). A shift register is a typical benchmark circuit used on assessment of a new circuit technology. It is also widely used in digital and mixed-signal circuits. Both of these circuits are quite suitable for implementation using the eSFQ approach, as they are clocked and therefore naturally coupled to an SFQ clock distribution network.

Circuit design and analysis of performance metrics were achieved with a pre-release version of the *NioPulse* software suite, whereas *LASI 7* software was employed for cell and chip layout. Circuit extraction and verification were done with the *InductEx* package.

Two different eSFQ versions of these shift registers were implemented: a straight-forward conversion from RSFQ termed “eSR” and a version with an additional magnetic flux bias, “MeSR”. The MeSR design is shown to have higher margins retaining the high speed conventional RSFQ design. It also has the potential to achieve lower bias current and thus, considering, lower dynamic power dissipation.

The eSFQ shift register cell, eSR, is depicted in Fig. 2.4.2(a). Its topology can be partitioned into two sections: *clock* and *data*. Junctions and the DMP () make up the clock section, which transmits the clock and interrogates the DMP. Note that we used a counter-flow clocking scheme, as this has generally yielded higher margins in conventional RSFQ designs. If switches, the clock pulse is simply transmitted from *CIn* to *COut*. If switches instead, the clock pulse is transmitted and an output pulse is generated, which exits at *DOut*. In either case, the phase increases by . The only bias current injection point for eSR is at point . Inductors and determine, to a large extent, the bias current distribution between and the DMP (somewhat skewed by Josephson inductances and parasitics). Junctions and make up the data section. After bias current ramp-up, is biased, whereas is not, which corresponds to the cell storing a “1.” After the first clock signal, the bias current redistributes to , which corresponds to the cell storing a “0”. A pulse appears at the output, representing the initially stored “1” as depicted in Fig. 2.4.2(b).

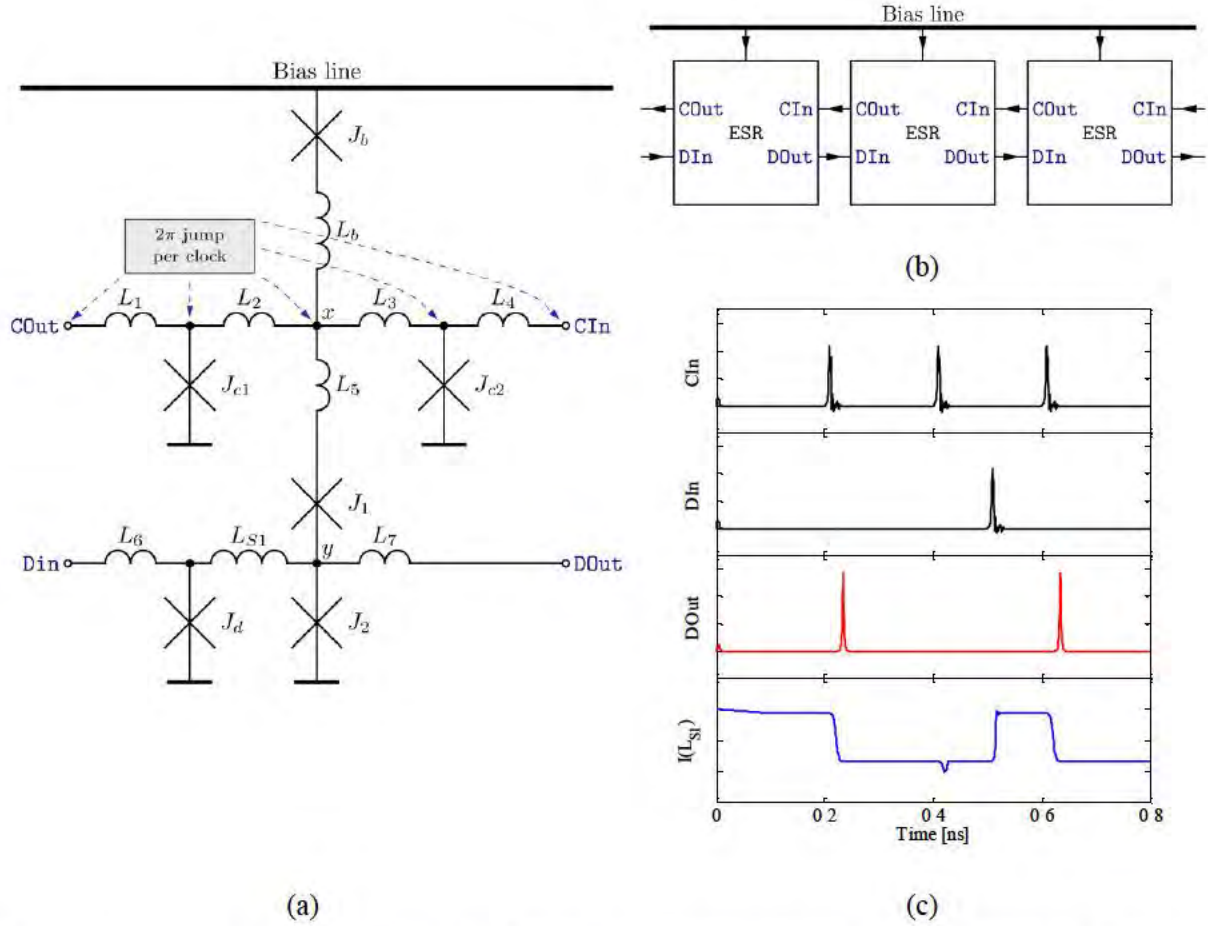


Fig. 2.4.2. eSR - eSFQ shift register cell: Schematic (parasitics are omitted) (a), typical configuration illustrating the counterflow clock (b) and simulated cell operation (c). Circuit parameters for (a): Inductances: $L1$: 2 pH, $L2$: 1.9 pH, $L3$: 1.2 pH, $L4$: 2.1 pH, $L5$: 2.1 pH, $L6$: 3.5 pH, $L7$: 3.4 pH, $LS1$: 10.8 pH, Lb : 10 pH. Critical currents: $Jc1$: 213 μA , $Jc2$: 250 μA , $J1$: 313 μA , $J2$: 188 μA , Jd : 225 μA , Jb : 575 μA . All junctions except $J1$ are critically damped (). $J1$ has .

Margins of operation of the circuit were determined for a 4-bit shift register configuration. The critical parameter was identified as the critical current of junction , the upper (escape) junction of the DMP. One of the reasons for this is the injection of bias current through the DMP as required in accordance with the eSFQ biasing scheme. The difference between the biased and unbiased DMP is evident from the phases of the DMP junctions shown in Fig. 2.4.3.

The grounded junction in a DMP () switches when it is biased, whereas the escape junction () switches when the grounded junction is not biased. The escape junction is, conventionally, not biased. Hence, when is unbiased as it is in case of RSFQ (ERSFQ) circuits, both junctions have a phase near zero, and as has a lower critical current, and is closer to the source of the interrogating pulse, it switches in the presence of an interrogating pulse. When is biased, its phase is nearly critical, with the phase of remaining near zero, making the switching junction when the DMP is interrogated. When biasing through the DMP as in eSFQ, the escape junction is permanently biased. This fixes its operating point phase at greater than zero,

increasing its affinity to switch, particularly as it is closer to the source of the interrogating pulse (the Clock node). This reduces the difference between the steady-state phases of ϕ_1 and ϕ_2 when ϕ_1 is biased. In this case, the increased switching affinity of ϕ_1 is undesirable (as ϕ_1 should then switch) and results in lower parameter margins for ϕ_2 .

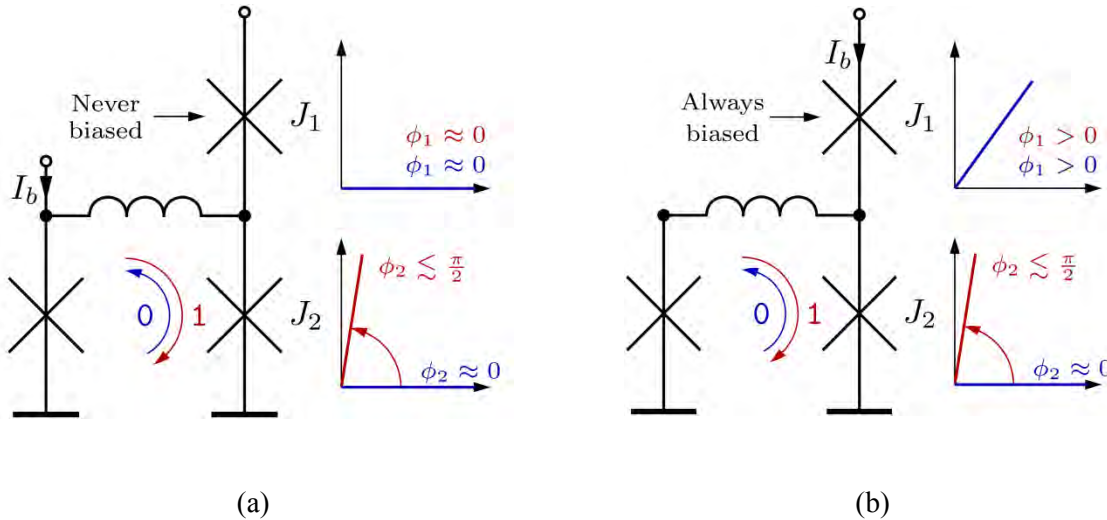


Fig. 2.4.3. Comparison of RSFQ (ERSFQ) and eSFQ biasing: Injecting bias current in the conventional DFF leaves the upper junction of the DMP unbiased (a). Moving the bias current injection point to the DMP forces the phase in both DMP junctions in the same direction during ramp-up (b). (Colour may appear only in the online journal.)

In order to improve the margins of ϕ_2 , it was designed in an underdamped configuration with $\beta \approx 1$. An underdamped junction exhibits lower switching speeds and is thus less likely to switch before ϕ_1 when the DMP receives the interrogating pulse. With the underdamped ϕ_2 , a 4-bit configuration of eSR achieved critical margins of $\approx 10\%$ and bias margins of $\approx 10\%$, with bias margin relating to the bias of the entire 4-bit test structure and critical parameter the area of $\approx 10\%$ for all four eSR cells.

Although underdamping ϕ_2 achieves the goal of increased parameter margins, it has the undesired side-effect of increasing data-dependent clock skew. Since ϕ_2 switches slower than ϕ_1 , the clock propagates through the shift register faster when the stored bits are primarily “1”s, and slower if the stored bits are primarily “0”s. This effect is seen also in conventionally biased shift registers, although to lesser extent. In conventionally biased shift registers, this effect is due to an underbiased escape junction ϕ_1 . In eSR, it is due to the slow-down imposed for eSFQ biasing. Compared to critical damping, for ϕ_2 as used above, the characteristic time of ϕ_2 is doubled, potentially halving the maximum clock frequency achievable.

Hence it was desirable to have all junctions equally shunted with $I_{c1} = I_{c2}$ and therefore, having the same junction speed, achieving the maximum frequency for a typical 4.5 kA/cm^2 critical current density. To accomplish this without punishingly narrow parameter margins, one might investigate several options. For correct operation an interrogating pulse must not cause ϕ_1 to switch when ϕ_1 is biased. At first glance, keeping the critical current of ϕ_1 low should achieve

this. Considering Fig. 2.4.2, when the bias current enters at node , some travels down the DMP, biasing junction . After crossing , the bias current divides again at node . The alternate path to ground through means that some of the bias current leaks away from , ensuring that always receives less bias current than . Lowering the critical current of increases its Josephson inductance, which exacerbates the leakage effect.

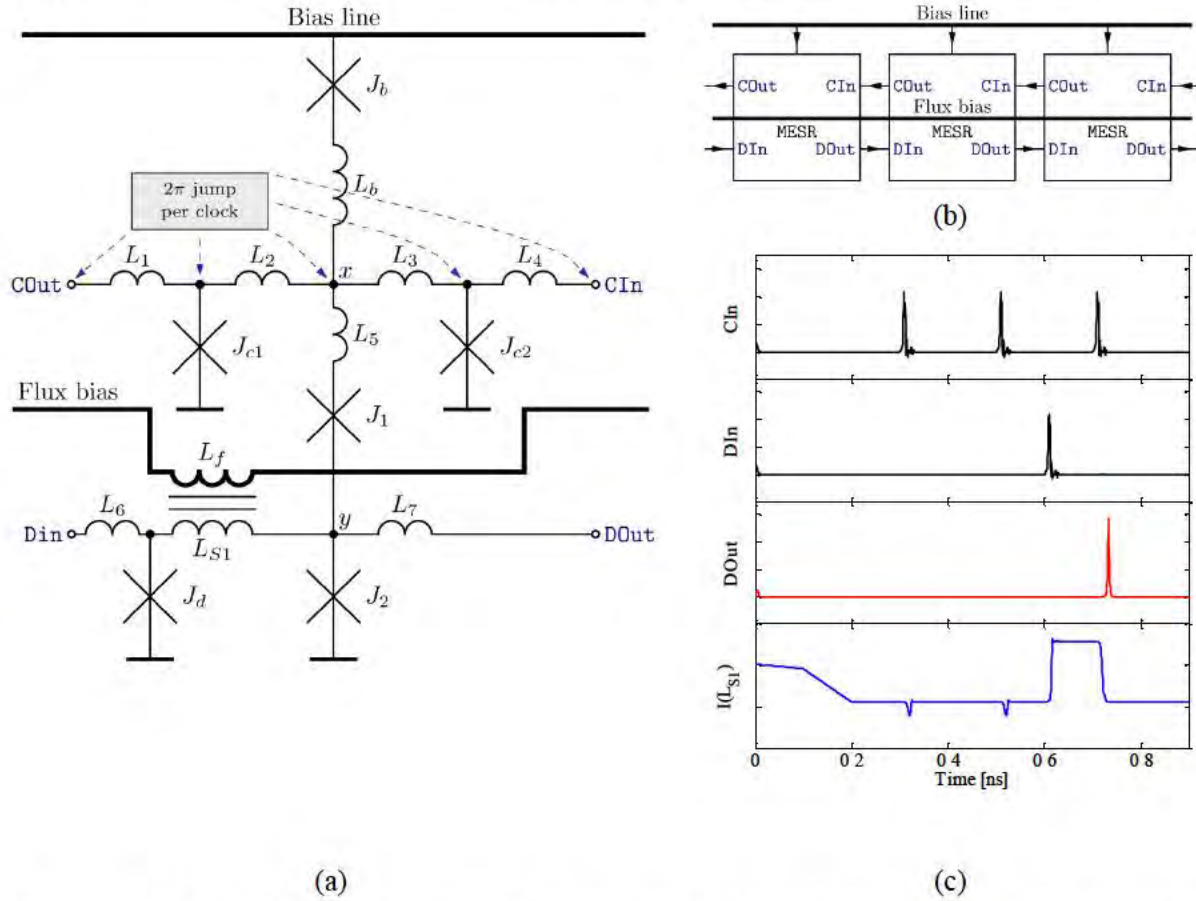


Fig. 2.4.4. MeSR - eSFQ shift register cell with magnetic flux bias: Schematic of eSFQ shift register cell with flux bias (parasitics are omitted) (a); a typical configuration illustrating the counterflow clocking scheme (b); simulated operation (c). The flux bias ramps up from 0.1ns to 0.2ns, clearly evident in the current trace for . After flux-bias ramp-up, MeSR is non-storing. Circuit parameters for (a): Inductances: $L1$: 2.2 pH, $L2$: 1 pH, $L3$: 1.8 pH, $L4$: 2.0 pH, $L5$: 1.8 pH, $L6$: 2.8 pH, $L7$: 4.2 pH, $LS1$: 11.2 pH, Lf : 11.5 pH, k : 0.25, Lb : 10 pH. Critical currents: $Jc1$: 188 μA , $Jc2$: 188 μA , $J1$: 288 μA , $J2$: 200 μA , Jd : 163 μA , Jb : 525 μA . All junctions are critically shunted.

A magnetically introduced corrective flux bias was used to solve the leakage problem, resulting in cell MeSR, depicted in Fig. 2.4.4. The dc flux bias, introduced through , forces the current in the storage loop to redistribute as intended, opposing the leakage effect. In this way, the phase offset of (as a result of the eSFQ bias current) can be modified. During circuit optimization, it became apparent that using the flux bias to redirect initial bias current from to was most effective at maximizing parameter margins. A potential advantage of this is that shift registers based on MeSR initially store a “0” which aligns well with conventional RSFQ shift registers.

A further advantage of the flux bias manifests itself in reduced bias current requirements in terms of injected bias current (and corresponding decrease in dynamic power dissipation). As undesired leakage can be avoided and the desired balance in the storage loop be established using the flux bias, less bias current needs to be injected at the injection point. Initial “0” storage and reduced bias current requirements are shown in Fig. 2.4.5. Note that one flux bias line is required to bias the entire shift register, irrespective of its length. For a 4-bit MeSR-based shift register, a critical margin of , and bias margin of were achieved.

The presence of the additional flux bias line might appear as a complication. In reality, a constant flux bias can be implemented in a variety of ways ranging from a small superconducting loop with frozen-in SFQ to a π -junction implemented using superconducting-ferromagnetic-superconducting (SFS) Josephson junctions. Even for conventional RSFQ circuits, the improved operational margins, bit-error rates, and gate memory non-volatility were reported.

The reduction of bias current directly translates into the reduction of dynamic power dissipation as . This makes the magnetic bias approach especially valuable. As magnetic flux bias is a passive non-switching element, it does not contribute to power dissipation. As is evident from the results of simulations for 20 GHz clock, the eSR shift register consumes ~ 1.0 aJ/bit, while the MeSR shift register consumes ~ 0.8 aJ/bit. These energies correspond to the centre of the bias current operational region. At the lower limit, the energy per bit operation reaches ~ 0.5 aJ/bit.

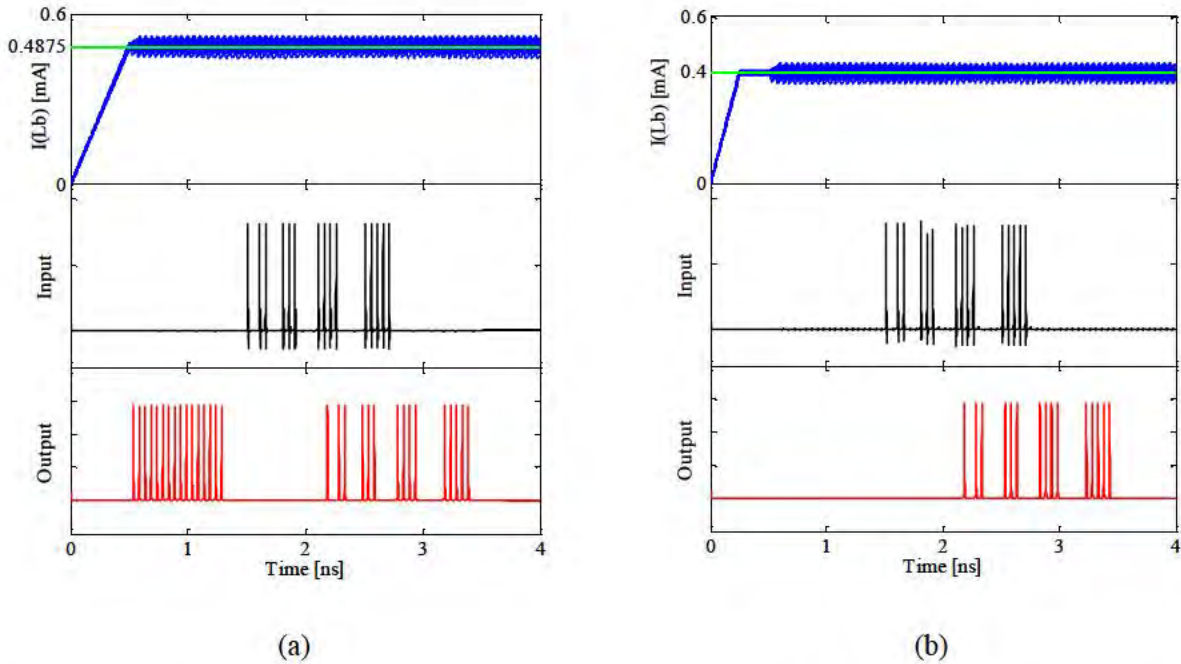


Fig. 2.4.5. Results of simulation with a 20 GHz clock for 1.0 aJ/bit eSR- (a) and 0.8 aJ/bit MeSR-based (b) 16-bit eSFQ shift registers at bias current corresponding to centre of operational region. Bias currents distribute correctly, with acceptable distortion through switching events. For the eSR-based shift register, 16 output bits are immediately observed after starting the clock. In both cases, the input pattern is reproduced at the output. Lower bias current requirements are evident for the magnetic flux-biased shift register.

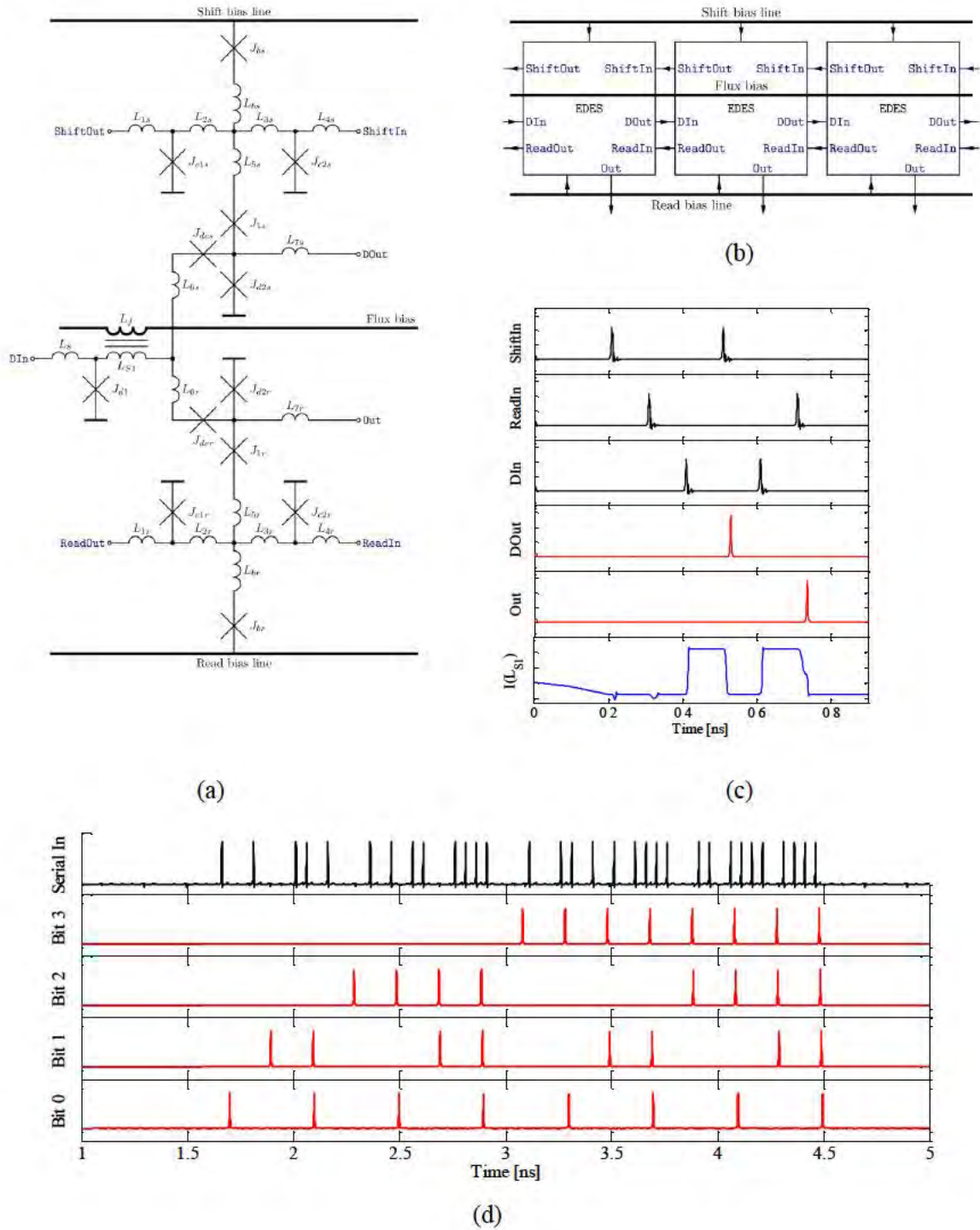


Fig. 2.4.6. eDES - eSFQ deserializer cell with magnetic flux bias. Schematic of eDES cell (a); a deserializer configuration (b); the operation of eDES (c). Flux bias is ramped up from 0.1 ns to 0.2 ns, as evident in the bottom trace. Initially, eDES is non-storing, but when a pulse arrives at DIn, it is stored, readable by both a Shift or a Read pulse. Simulated 4-bit operation of the deserializer at 20 GHz (d). Clearly, the input signal (a count from 0 to 15) is parallelized, resulting in 4 output streams. Circuit parameters for (a): Inductances: $L1s$: 2.9 pH, $L2s$: 2.0 pH, $L3s$: 1.4 pH, $L4s$: 1.2 pH, $L5s$: 0.2

pH, L6s: 0.9 pH, L7s: 4.2 pH, L8: 2.0 pH, L5l: 3.1 pH, Lbs: 10 pH, Lf: 16.1 pH, k: 0.24, L1r: 1.7 pH, L2r: 1.7 pH, L3r: 1.6 pH, L4r: 2.5 pH, L5r: 0.2 pH, L6r: 0.6 pH, L7r: 3.4 pH, Lbr: 10 pH. Critical currents: Jc1s: 163 μ A, Jc2s: 188 μ A, J1s: 288 μ A, Jd2s: 188 μ A, Jdes: 200 μ A, Jd1: 150 μ A, Jbs: 500 μ A, Jc1r: 188 μ A, Jc2r: 188 μ A, J1r: 225 μ A, Jd2r: 188 μ A, Jder: 138 μ A, Jbr: 500 μ A. All junctions are critically shunted.

RSFQ deserializers (demultiplexers) generally follow two different approaches: a binary tree or a shift-and-dump architectures. For conversion to eSFQ, we chose the latter approach as it has found more applications in practical circuits due to its high modularity and simple timing. Our eSFQ deserializer is based on a dual-port D flip-flop or D²-cell, which is a derivation of the B flip-flop. One port is intended for serial shifting of data, the other for parallel readout. An -bit deserializer divides a serial stream of bits into parallel streams.

The designed eSFQ deserializer cell, eDES, is depicted in Fig. 2.4.6. The two readout ports are topologically symmetrical, both achieving destructive readout of stored flux. Note the additional escape junction in each readout arm (). The deserializer cell contains two DMPs, suggesting two bias injection points. As in MeSR, a flux bias is employed in the data section to achieve the desired bias current distribution between . All junctions were designed to be critically shunted. When correctly biased, eDES stores a “0” after ramp-up.

There are essentially two clocks that thread each deserializer cell. The symmetry of the cell and size of the limiting junction means that the per-bit switching energy required by the shift operation as well as the read operation is comparable to that of the MeSR-based shift register. For normal operation the ratio of the clock frequencies depends on the length of the deserialiser. A per-bit switching energy is thus not meaningfully ascribed to the deserializer cell, but for long deserializers the per-bit switching energy of the deserializer approaches that of the MeSR-based shift register.

Experimental Evaluation

In order to investigate eSFQ logic experimentally, the eSR, MeSR and eDES cells were laid out and their circuits were reoptimized to account for the extracted layout parasitics. Several eSFQ shift registers with 16- and 32-bit length, as well as deserializers with 4-, 8- and 16-bit lengths were assembled. Fig. 2.4.7 shows examples of the experimental eSFQ chips designed for fabrication using the HYPRES Niobium superconductor integrated circuit fabrication process. To investigate the performance of the designed eSFQ circuits in a variety of environments, 12 test structures were laid out across five 5 x 5 mm² chips for the fabrication with a 4.5 kA/cm² Josephson junction critical current density.

Fig. 2.4.8 shows examples of the fabricated eSR, MeSR circuits. As is evident, they differ in the escape junction J₁ shunt resistor in order to achieve overdamping for the eSR design and critical damping for the MeSR design. For MeSR, the magnetic flux bias was implemented as a superconducting line under the cell storage inductors to induce magnetically the required phase shift. Microphotographs of the deserializer are depicted in Fig. 2.4.9. In order to protect circuits from flux trapping, ground plane moats were employed as well as ground plane holes covering unused chips areas.

To concentrate design effort on the eSFQ demonstrator cells and to minimize the probability of failure in the periphery circuits, existing conventional RSFQ cells from the HYPRES cell library were employed as a testbed. These comprise standard interfaces to room-temperature circuitry,

such as dc/SFQ and toggle-type SFQ/dc converters. Fig. 2.4.9(b) shows an RSFQ testbed made of these standard library RSFQ cells. The test chips also contain standard diagnostic circuits for fabrication process control visible in Fig. 2.4.7.

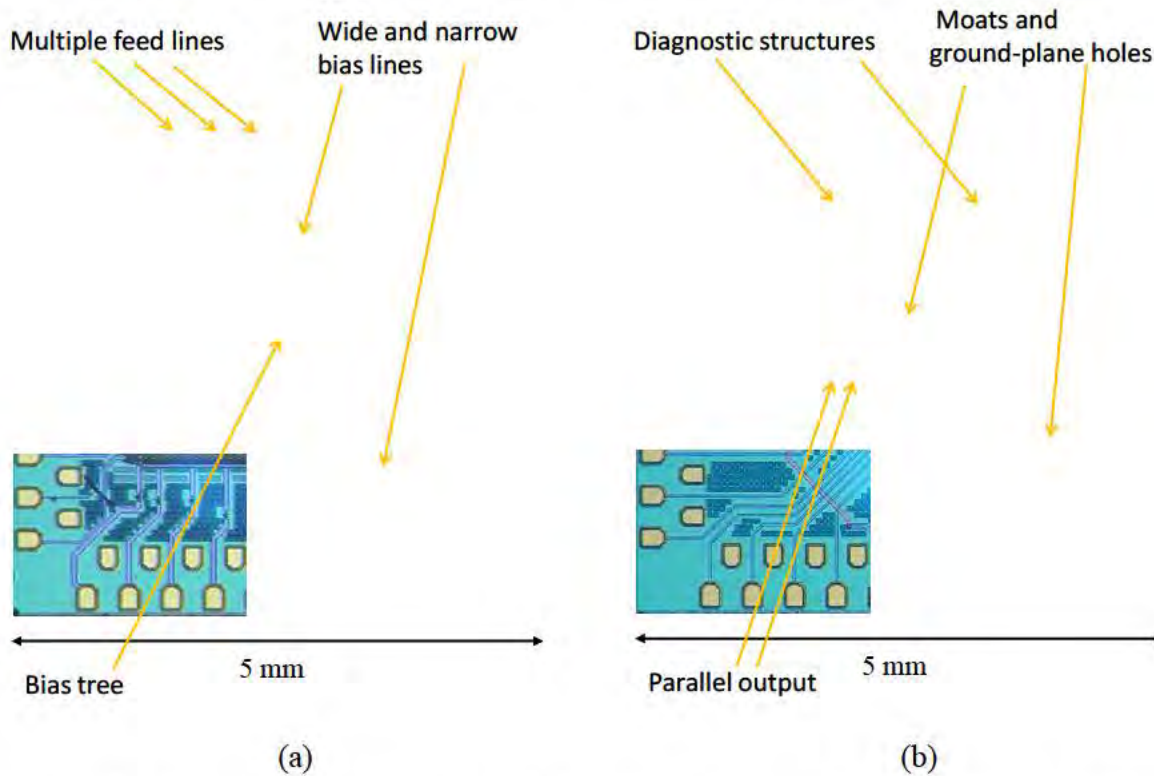


Fig. 2.4.7. Layouts of two of the five 5x5 mm² ICs fabricated with HYPRES's 4.5 kA/cm² process, one with three shift registers (a), and one with a 16-bit deserializer (b). Each bias line is fed from multiple contact pads, which enables experimental investigation of different bias fan-in configurations.

Besides establishing functional correctness of the designed eSFQ cells, the objective was to investigate experimentally the effects of the bias current distribution in superconducting biasing network at the initial bias current ramp-up. Since eSFQ circuits do not have resistors in the bias network, the bias distribution relies on interplay between specific inductances of the bias lines and gate current limiting junctions. This is not easy to simulate as the circuit initialization is inherently a slower process than its SFQ operation. For this reason, several versions of shift registers with different width (specific inductance) of bias distribution buses and different current injection fan-in were designed.

Thus, in addition to laying out different combinations of the basic designed cells, these were placed in a variety of different bias lines. The designed bias lines are characterized by the cell-to-cell inductance of the line, L_{cc} , as well as the line-to-cell limiting inductance, L_{lc} . Bias lines of two different widths (narrow: 10 μ m, pH, wide: 20 μ m, pH) were laid out and combined with three lengths of limiting inductor (short: 10 μ m, pH, medium: 20 μ m, pH, long: 30 μ m, pH).

For each laid-out structure, bias fan-in was conservatively high. Each structure has its own bias line, which is shared by all cells in the structure (deserializer structures each have two bias lines,

one for the read- and one for the shift operation). One bias pin was allocated to every four cells in a structure. This enables comprehensive investigation of different bias-current fan-in configurations (biasing from all available pins or biasing from one pin only, for example). Fig. 2.4.7 depicts two examples of chip layout, illustrating the high number of bias-current pins. To further the breadth of this investigation, one structure was equipped with a bias-current divider that binds the four bias line entry points of the 16-bit shift register to a single pin.

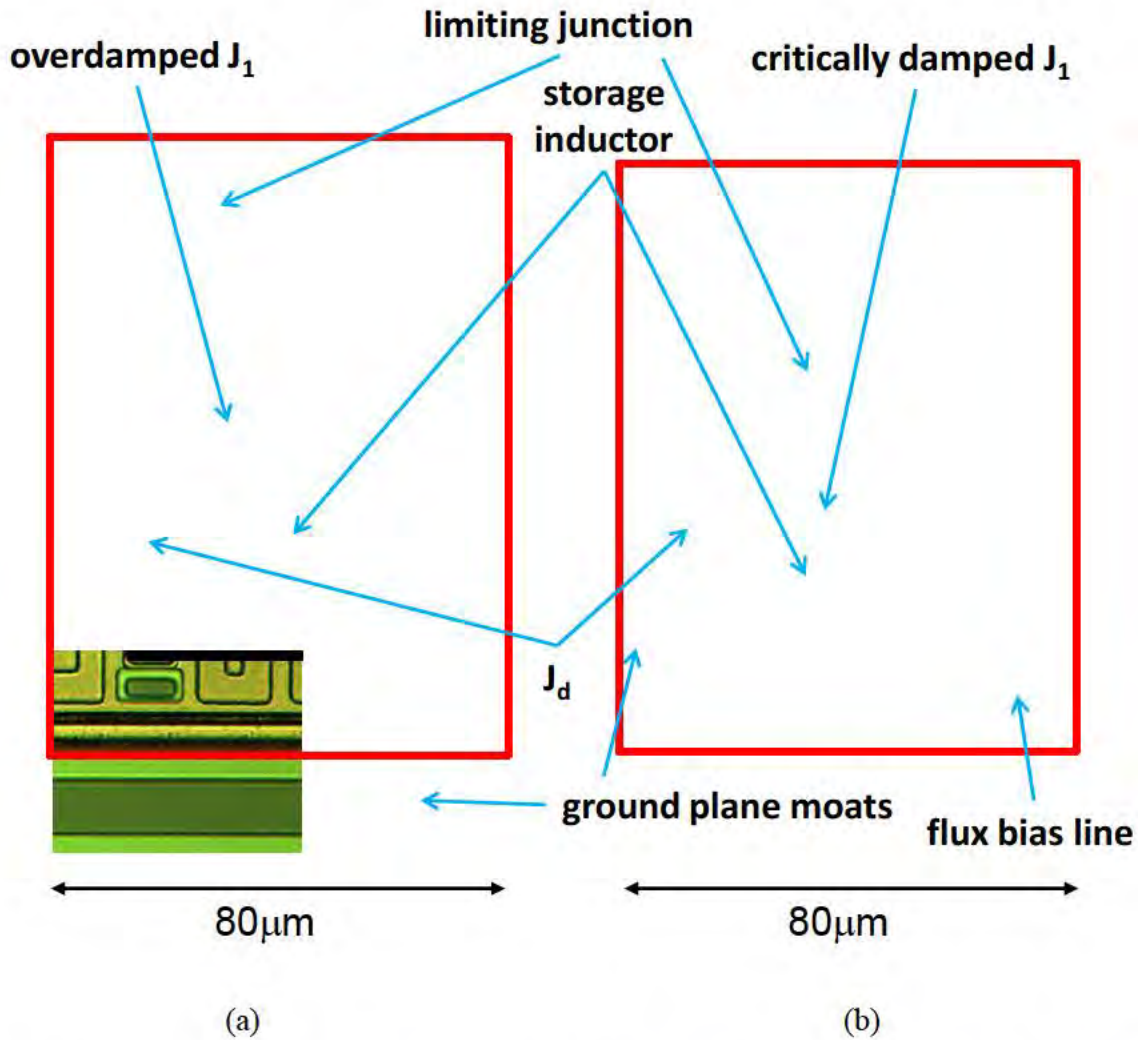


Fig. 2.4.8. Layouts of eSFQ shift register cells eSR with overdamped (a) and MeSR with critically damped and a flux bias line inductively coupled to cell storage inductor (b). Cell sizes (indicated by red boundary): eSR: 80x110 , MeSR: 80x105 . These dimensions do not include the bias line.

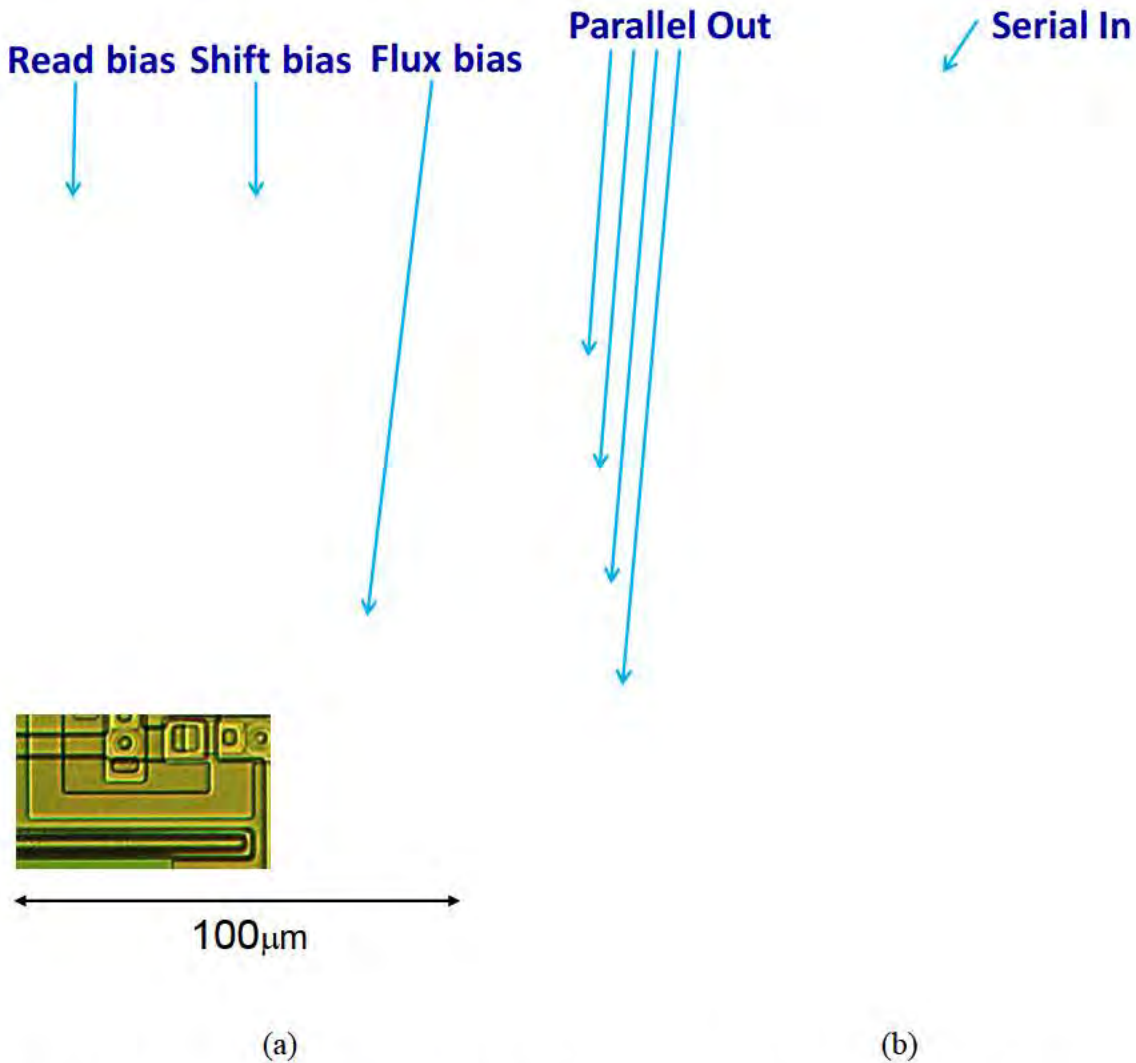
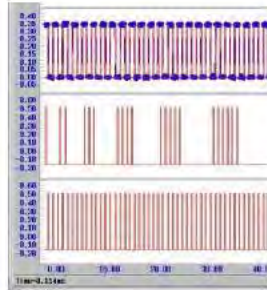


Fig. 2.4.9. Photographs of deserializer test structures: the deserializer base cell eDES (a), and a corresponding 4-bit eSFQ deserializer (b). Bias lines and some key devices are indicated. A set of dc/SFQ and SFQ/dc converters enable the interface with room temperature electronics.

Experimental evaluation was performed with test patterns applied and responses measured with the Octopux system. Each chip was tested in a liquid helium dewar using HYPRES standard cryoprobes. Correct operation of the shift register structures was established by feeding in a bit pattern and verifying its transmission with the correct delay (in terms of clock events). Correct - bit deserializer operation was established by feeding in a pattern of length with the shift clock, applying a read pulse, and then verifying the parallel readout against the input pattern. This process was repeated several times to verify deserializer operation. Figs. 4.10-11 depict examples of the measured correct test patterns of the 16-bit eSFQ shift registers and deserializers. For exhaustive testing, not only uniform clock and data patterns were employed, but also randomly generated ones.



(a)

(b)

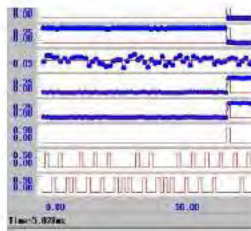
Data out

Clock out

Data in

Clock in

Fig. 2.4.10. Measured correct functionality of 16-bit eSFQ shift registers: simple pattern (a), randomly generated data and clock pattern (b). All 9 shift registers were fully operational.



(a)

(b)

Data out

Bit 1

Bit 2

Bit 3

Bit 4

Bit 5

Bit 6

Bit 7

Bit 8

Bit 9

Bit 10

Bit 11

Bit 12

Bit 13

Bit 14

Bit 15

Bit 16

Read clk

Data in

Shift clk

Fig. 2.4.11. Measured correct functionality of 16-bit deserializer for different input patterns. This circuit divides the input serial stream into 16 output parallel streams. Random data and shift clock pulses are used for testing. Note that measured voltages are scaled automatically.

To determine the bias margins of investigated structures, random 200-bit test patterns were applied to the devices under test for various bias currents. Various bias-current feeding

configurations were investigated, most notably biasing from one pin only (repeated for each available pin), and biasing from all pins simultaneously. Only the largest identified continuous region of operation was considered. All tested structures passed functional testing for all tested patterns. The measured results of the bias current margin investigation are listed in table 1.

Table 1. Experimentally determined bias margins for eSFQ test structures across five chips: a comprehensive set of devices in different bias configurations, measured to establish functional correctness of the devices and attempt to identify desirable traits of the bias line layout.

Kind	Len	Bias Line		Comment	Bias margins [mA]	
					All pins	Single pin
Shift Reg	32	Narrow	Medium			
Shift Reg	16	Narrow	Medium	Bias Tree	-	
Shift Reg	32	Wide	Medium			
Shift Reg	16	Narrow	Short			
Shift Reg	16	Narrow	Medium			
Shift Reg	16	Narrow	Long			
Shift Reg	32	Narrow	Medium	Flux Bias		Not tested
Shift Reg	16	Narrow	Medium	Flux Bias		Not tested
Shift Reg	16	Wide	Medium	Flux Bias		Not tested
Deserialiser	16	Narrow	Medium	Flux Bias	(Clk) (Rd)	Not tested
Deserialiser	8	Narrow	Medium	Flux Bias	(Clk) (Rd)	Not tested
Deserialiser	4	Narrow	Medium	Flux Bias	(Clk) (Rd)	Not tested

The measured bias margins roughly conform to expectations extrapolated from simulated results. Simulations relied on (small) 4-bit configurations to reduce computation time to design-friendly speeds and were performed in high-speed testbeds, not reflecting the actual devices under test or their periphery. The observed agreement with simulations confirmed that the designed structures are robust and scale well.

As Fig. 2.4.12 indicates, the MeSR-based shift registers (with magnetic flux bias) functioned only when the magnetic bias is applied, which corresponds to our simulations. Bias margins do not seem dependent on the length of the shift register structure, although the dataset is too small to identify definite trends.

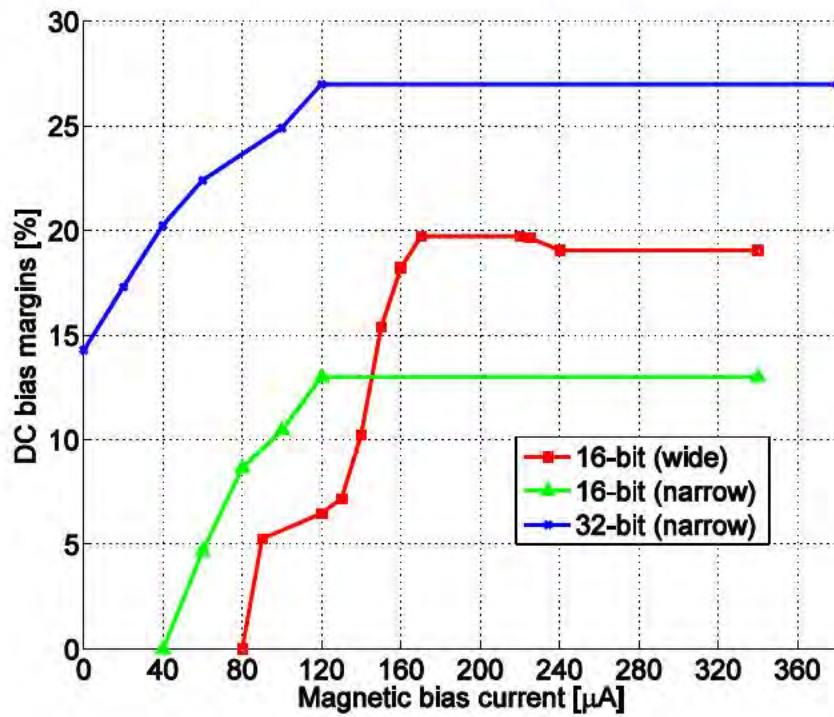


Fig. 2.4.12. Measured bias margins vs. magnetic bias for different MeSR-based shift registers.

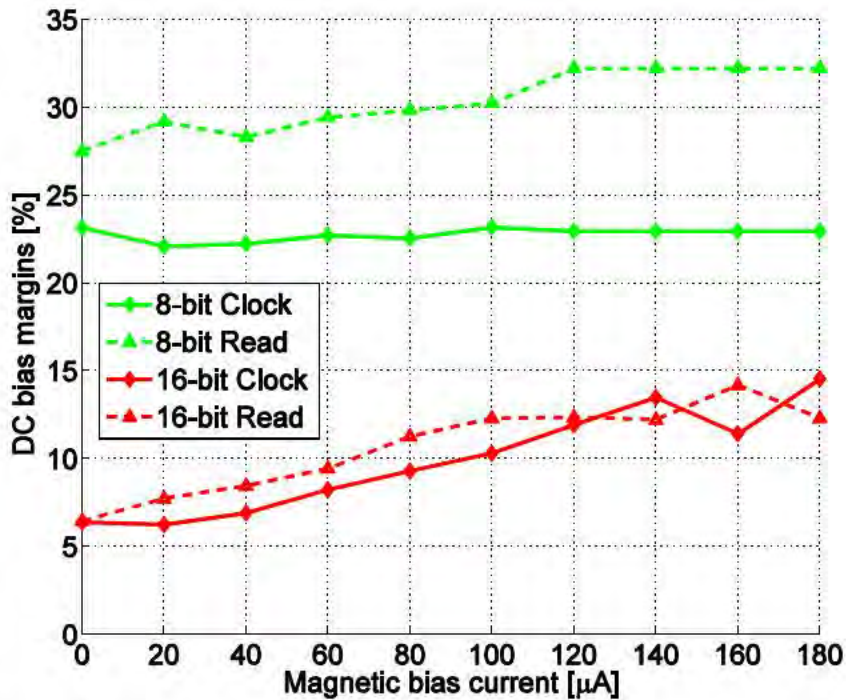


Fig. 2.4.13. Measured bias margins vs. supplied magnetic bias current of 8-bit and 16-bit deserializer test structures.

The deserializer structures under test worked without the magnetic flux bias applied. As demonstrated in Fig. 2.4.13, applying the magnetic flux bias improves their bias margins, doubling them in the case of the 16-bit deserializer. For the 16-bit deserializer, the clock and read bias margins exhibit comparable absolute values and dependence on the magnetic flux bias, which is consistent with simulations. The 8-bit structure does not mirror this symmetry, which may indicate higher susceptibility to the periphery.

Comparatively low bias margins were recorded for the 16-bit deserializer. We attribute this to the relative complexity of the test structure and to an ill-designed monitor setup. The high fan-out of the deserializer requires a large number of SFQ/dc monitors, as well as several dc/SFQ converters to apply the test patterns. Due to the high pin count of the test structure (two bias lines, parallel output), all peripheral cells were biased from a single pin, which yielded low margins for the peripheral bias, potentially depressing the margins of the device under test.

As for designing optimal bias line inductances and limiting inductors, the experimental test structures did not yield conclusive trends. We conclude from this that these inductances, at least when constrained to the parameter ranges investigated, do not significantly affect bias current distribution, which is a positive result. Promising are the high bias margins measured for the 16-bit shift register biased from a single pin feeding a bias tree. This suggests that the off-chip biasing effort for eSFQ systems should be comparable to systems based on conventional RSFQ.

Conclusions

We have demonstrated for the first time eSFQ digital circuits – a new ultra-low power RSFQ-type logic capable of achieving a significant increase in energy efficiency of computing systems. The demonstrated eSFQ shift registers reached ~ 0.8 aJ/bit. This number includes the integrated SFQ clock lines. The achieved energy per bit is over two orders of magnitude better than that of the same circuits implemented in conventional RSFQ logic.

Similar to ERSFQ, another energy efficient RSFQ-type logic, eSFQ relies on limiting Josephson junctions to distribute the dc bias to logic gates. In contrast to ERSFQ, the limiting junctions do not switch during circuit operation and are needed only for the initial bias current ramp-up. This is achieved by the bias current injection via two-junction decision making pairs (DMPs) which have equal phases during the gate operation independent of digital data. This also allows eSFQ circuits to operate without large bias inductances otherwise needed to minimize data dependent bias current fluctuations. As a result, the eSFQ circuit layouts are more dense and easier to scale.

However, we found that the injection of bias current via DMPs depresses parameter margins. In this work, we explored ways to rectify this effect by using either stronger junction damping (slowing down the DMP escape junction) or passive phase shifters. The first method is simpler in the implementation but leads to a reduction of the maximum speed of operation. The second method does not limit the maximum clock frequency but requires an introduction of extra phase shifting elements such as flux bias line or π -junctions.

Passive phase shifters would bring an additional, perhaps even more significant result: a reduction of the required dc bias for eSFQ gates. We demonstrated that phase shifters allow a $\sim 20\%$ gate bias reduction which directly translates to the corresponding $\sim 20\%$ reduction of the gate dynamic power dissipation, . We believe that this number can be further improved with the targeted circuit optimization. For example, the critical currents used in these circuits are in a 180-300 μA range, which is larger than required by thermal noise at 4 K.

In contrast to a simple flux biasing line implemented in this work, the introduction of phase shifting π -junctions would require the incorporation of ferromagnetic materials into a conventional superconducting fabrication process. This might look cumbersome and expensive at first, but the work on the superconductor-ferromagnetic fabrication process is already happening. It is motivated by the recent efforts in superconducting magnetic memory developments and research in superconducting spintronics. We expect that superconductor-ferromagnetic phase shifters will be preferable for eSFQ circuits.

The demonstrated eSFQ shift register design is quite compact comprising five junctions per bit excluding the passive bias-limiting junction. The total number of junctions for a 16-bit shift register is 80. This compares favourably to an RQL shift register with 8 junctions per bit.

While achieving a significant improvement in power dissipation, the demonstrated eSFQ logic retains all key advantages of conventional RSFQ logic: high speed, high throughput, dc bias, controllable and programmable SFQ clock, and lossless interconnects. As opposed to ac biasing and global clock, the eSFQ dc bias and locally controllable SFQ clock is particularly advantageous for scaling up integrated circuit complexity to millions of junctions. Simple eSFQ layout requirements without the need for transformers and microwave plumbing also bode well in terms of scaling up the circuit density. Finally, the ability to control the SFQ clock distribution allows management of eSFQ circuit power dissipation. This is the pre-requisite for the development of energy proportional processors – the ultimate goal of computing system developers.

Superconducting systems require cryocooling. The efficiency of 4 K cryocoolers ranges from $\sim 10,000$ W/W for small cryocoolers (heat capacity of < 1 W) to < 400 W/W for large machines (heat capacity of 600-900 W). For high-end computing systems, the larger cryocoolers are relevant. For example, for the Linde LR280 with 360 W/W efficiency, this puts the eSFQ circuit demonstrated in this work at ~ 290 aJ/bit. This is close to the projected bit energy for a future CMOS gates, however, one should realize that the biggest energy loss ($> \sim$ pJ/bit) in CMOS circuits is in data movement. In contrast, superconducting SFQ circuits including eSFQ can use ballistic data transport at the similar sub-aJ per bit level as for logic and register circuits. There is also a potential advantage of superconducting SFQ circuits over room-temperature competition in power density, which constrained the progress towards faster CMOS circuits. Assuming that eSFQ circuits can be scaled to the CMOS circuit densities, power density will be at least three orders of magnitude lower, as the cryocooling penalty does not change this difference. The practical advantage of this much lower power density requires further study to account comparative heat removal capabilities and operation temperature ranges. This will be done in the next project period.

III. Energy-Efficient Interface based on Ultra-Low Input Voltage polarization modulating VCSELs

Scope

The overall goal of this multi-phase project is to develop and demonstrate the energy-efficient data output interface between cryogenic 4 K modules and room-temperature systems using a combination of energy-efficient:

- low-voltage drivers based on energy efficient SFQ logic;
- lossless, low dispersion superconductor cables;
- low-voltage electro-optical links based on polarization modulating (PM) VCSELs.

Objective is to achieve a record energy-efficiency of <0.2 pJ/bit at 12 Gb/s. The projected data rate is targeted to 12.5 Gbps and then further extended to higher data rates (~ 25 Gb/s).

The current work focuses on the development of a critical component technology – energy-efficient high-speed, very low input voltage (~ 1 mV) Polarization Modulation (PM) VCSELs:

Project funding for this project period (Phase 2b): \$184K.

The project team consists of HYPRES and Prof. K. Choquette group from University of Illinois (Urbana). Report cover progress from Sep. 1, 2012 to Aug. 30, 2013.

The Energy-efficient Cryogenic Optical (ECO) data link design is based on balancing power dissipation and signal gain at each temperature stage to maximize overall energy efficiency following the recently introduced Thermo-Gain Rule. To achieve VCSEL light emission with two switchable distinct polarization modes, a cruciform-shaped anisotropic optical cavity is formed by fabrication of a photonic crystal with etched periodic air holes surrounding the unetched cruciform region. In this report, we present the results of design, fabrication, and preliminary testing of the ECO data link components

Introduction

The lack of the energy-efficient, high-bandwidth, and scalable technology for data links from cryogenic low-power superconducting circuits to room-temperature higher-power semiconductor circuits has been a serious impediment for application of superconducting electronics including digital-RF receivers, instrumentation, high performance computing, network switches, sensor systems, etc. [1]-[5]. There were multiple attempts to address this problems [6]-[10] using all-electrical or electro-optical (E/O) links. The E/O data links are generally preferred for communication in high-performance computing systems. For exascale systems, the link energy efficiency should be on the order of 2 pJ/bit [11]. The use of an optical fiber to carry digital data has an additional benefit for cryogenic systems due to its negligible heat leak and signal attenuation. In this paper, we will focus on the development of key components for the energy efficient cryogenic E/O links capable of transmitting data at >20 Gbps and ~ 1 pJ/bit.

Technical Approach: Cryogenic Output Data Link

Fig. 3.1 shows a diagram of our energy-efficient output digital link from 4 K superconducting modules to room temperature electronics. The SFQ digital data is converted to ~ 1 mV voltage

pulses using low-power, compact superconducting drivers. These relatively weak pulses are transported to a ~ 70 K stage using low-loss, low-dispersion, low-heat-leak electrical cables. At this stage, the data is converted to the optical domain and transmitted to room temperature via low-loss, low-dispersion, low-heat-leak optical fiber. To determine the total link efficiency, the power dissipation at each temperature stage has to include the cryocooler (closed cycle refrigerator, CCR) efficiency. These efficiencies vary depending on CCR size [12], [13] as shown in Fig. 3.1. For some CCRs, warmer stages of CCR have limited excess cooling capacity (a flat load curve) providing an opportunity to cool circuits without the increase of overall power [13]. To achieve the link energy efficiency F_{EE} maximization, we distribute amplification of the transmitted signal (and, therefore, dissipated power) over different temperature stages following the Thermo-Gain Rule (TGR) [14]: $1/F_{EE} \sim G_1/T_1 + G_2/T_2 + G_3/T_3$, where G – gain of an amplifier located at temperature T , e.g., $T = 4$ K, 70 K, 300 K. The amplification gain at each temperature stage should be kept to a minimum – just enough to provide a low-bit-error data transmission to a warmer stage over the connecting cable. The less signal degradation in the cable, the less signal gain is required at the colder stage.

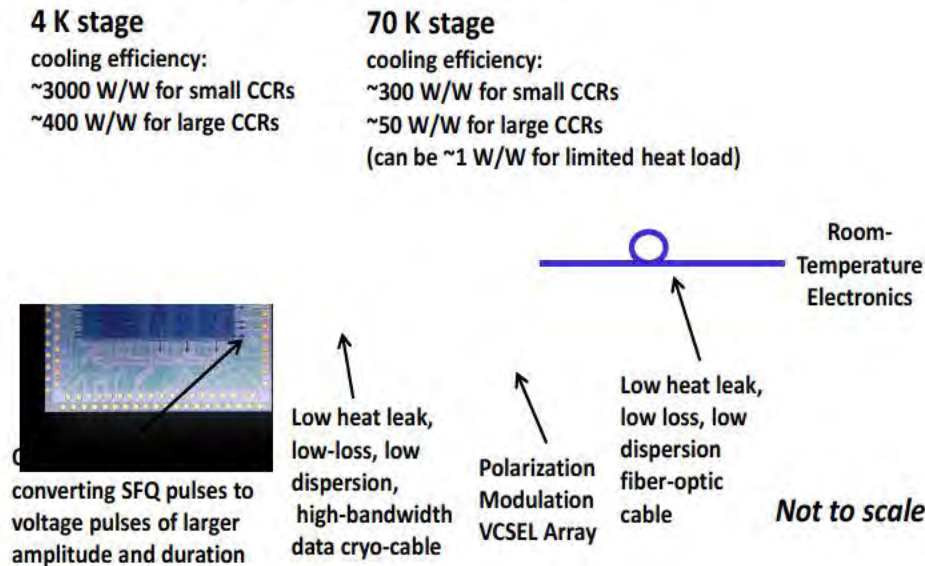


Fig. 3.1. ECO Data Link concept - an energy-efficient data interface to transport high-speed digital data from cryogenic to room-temperature stages. Signal amplification is distributed over different temperature stages of closed cycle refrigerator (CCR).

Superconductor SFQ electronics operate with SFQ pulses of $E_J = \Phi_0 I_C \sim 10^{-19}$ J. The low signal energy is the major advantage of SFQ electronics. At the same time, this poses a significant challenge for getting output signals to room-temperature electronics or optics. To amplify these signals, a number of superconducting amplifiers (drivers) were developed [6]-[9], [15]-[17]. To minimize the power dissipation, we use the smallest and fastest driver: the toggle flip-flop (TFF) SFQ/dc converter. To increase its energy-efficiency, the circuit dc bias was re-designed using a combination of ERSFQ-style biasing [18] for the TFF circuit, and the dc bias for the output junction pair applied via the output data line. This new scheme was successfully verified experimentally. These drivers are also the most compact compared to other known superconducting drivers, which is an important feature for high-density circuits.

The output data cable connecting the 4 K drivers to the 70 K circuits has to prevent a heat leak, provide minimum losses and dispersion for the mV-level signals transmission, and avoid joule heating associated with dc biasing via output lines. All these requirements can be met by HTS cables. The HTS cables have been already proven for dc biasing [19]. To provide proper impedance for high-bandwidth data transmission, HTS bit-lines can be formed as coplanar lines. To achieve lower crosstalk and denser line placement, a two-layer HTS microstrip multi-bit cable is being developed [20].

The choice of E/O component is guided by a significant signal level difference between the ~mV-level output signals of superconducting drivers and *volt*-levels signals typically required to drive existing E/O devices. The lowest driving voltage E/O modulators available today require ~400 mV [21] with prospects to achieve sub-100 mV in the future. However, even this goal is hardly acceptable, since it would require the use of power- and area-consuming intermediate amplifiers to amplify sub-mV signals.

As an alternative to E/O modulators, vertical cavity surface emitting lasers (VCSELs) can be used [22]-[28]. These laser diodes require low operation power, allow high-density integration, and can be optimized for operation at cryogenic temperatures. However, the amplitude of the VCSEL output is modulated using typically a few mA variation of laser drive current (corresponding to > 100 mV voltage swing). Therefore, the conventional approach of *modulating intensity* of the laser output is not advantageous compared to E/O modulators. In order to obtain a significant reduction in driving signal to the millivolt levels, we propose to *modulate polarization* of VCSEL output to transmit digital data as shown in Fig. 3.2.

In a polarization-modulation (PM) VCSEL, both the transverse cavity geometry and current injection are designed to be anisotropic to fix the VCSEL emission polarization [22], [23], which otherwise would be random [24]. In our cruciform VCSEL design, two orthogonal polarizations are allowed due to the effect of index-guiding and loss confinement in the laser diode, shown in Fig. 3.2. By injecting current into one of the two perpendicular arms, the dominant polarization direction can be selected (Fig. 3.2). In contrast to VCSEL direct intensity modulation, such polarization switching should only require a small driving signal, and the VCSEL emission intensity will remain relatively constant.

The transverse optical aperture is defined by a cross-shaped defect in a square-lattice pattern of air holes. The lattice of holes creates a photonic crystal which can be used to control the optical confinement [25]. Injection anisotropy is achieved by the bias applied to the two orthogonally positioned pairs of metal contacts [22] across a cruciform current aperture surrounded by high-energy proton implantation.

We demonstrate experimentally that the dominant polarization of PM VCSEL emission follows the direction of current injection, as indicated in Fig. 3.3. A polarizer is inserted in front of the photodetector. The light output of the VCSEL operated at room temperature is measured to determine the polarization of emission. Fig. 3.3 shows the polarization-resolved continuous wave laser outputs when the horizontal (threshold at 12 mA) or vertical (threshold at 17 mA) arm of the cruciform VCSEL are injected with current [22]. By injection into either arm of the laser cavity at 17 mA, the direction of the laser polarization can be selected with the direction of current injection with nearly 10 dB selectivity.

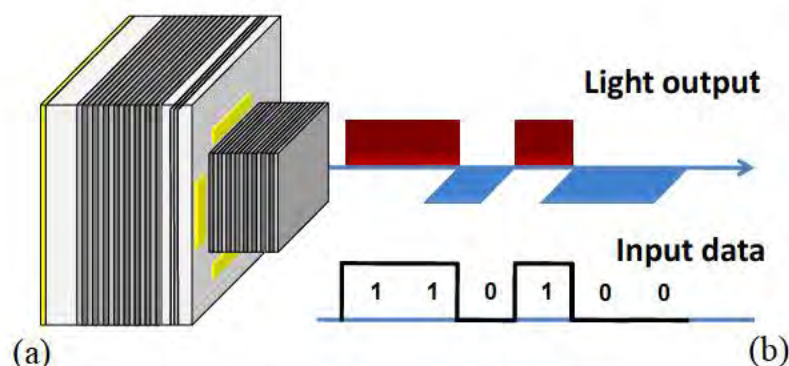


Fig. 3.2. (a) Modulation of the VCSEL light output. The polarization of the output light is varied between the two linear orthogonal states as controlled by the separate electrical contacts. (b) Scanning electron microscope image of a PM VCSEL showing square-lattice photonic crystal defects and orthogonally positioned top metal contacts to control VCSEL output light polarization.

VCSELs have been characterized at cryogenic temperatures [20], [21]. It has been found that the threshold current, output power, and laser emission characteristics can all be optimized for cryogenic operation by engineering the epitaxial design of a VCSEL. In particular, by creating an offset between the maximum wavelength of the laser gain produced by the quantum wells as compared to the allowed VCSEL emission from the cavity resonance, the performance of the VCSEL can be tuned for a particular operation temperature. For cryogenic VCSELs, their optical performance will be reduced at room temperature, but found to be optimal at their design temperature. This implies that custom compound semiconductor epitaxial materials are required for optimum cryogenic VCSELs. We have been optimizing VCSEL performance by fabricating samples with a dielectric top distributed Bragg reflector (DBR) [28]. In the following section, we provide details of this work.

Development of Polarization Modulating VCSELs

This section describes the research activity at the University of Illinois by Prof. Kent Choquette and his students during the period Sep. 1, 2012 to Aug. 30, 2013. The specific objective is to explore low power modulation of the light output from a VCSEL emitting at 850 nm. The Phase II activity began approximately March 1, 2012 and is scheduled to end approximately Sept. 30, 2013. This research includes the following tasks: (1) Design and fabricate revised photolithographic masks for photonic crystal ion implanted VCSELs for polarization modulation using “half VCSEL” epitaxial materials; (2) fabricate prototype VCSEL devices using epitaxial VCSEL material and characterize devices; (3) fabricate prototype polarization modulation VCSEL devices using epitaxial VCSEL material; (4) characterize at room temperature the laser performance, including polarized light versus current, emission spectrum, and polarization properties; and (5) provide recommendations and assistance to HYPRES staff for packaging VCSELs for cryogenic measurements. The following describes in detail our results to date.

Revised Mask Design

Starting in the Fall of 2012, revised mask designs were made in order to fabricate VCSELs with a top distributed Bragg reflector (DBR) mirror composed of dielectric materials (Fig. 3.3). Hence the semiconductor epitaxial materials correspond to a “half VCSEL” composed of a semiconductor bottom DBR, and active region, and capped with a contact layer. On top of this wafer, after device patterning and fabrication, a top DBR is deposited. The advantage of this

structure is to avoid current transport through the top DBR which was found in Phase I to create isotropic, rather than directional, current injection. Two mask levels were made: an ion implantation mask (used to define the current path) which is smaller than previously used, and a mask to define the extent of the top DBR mirror over the cruciform cavity (see Fig. 3.4).

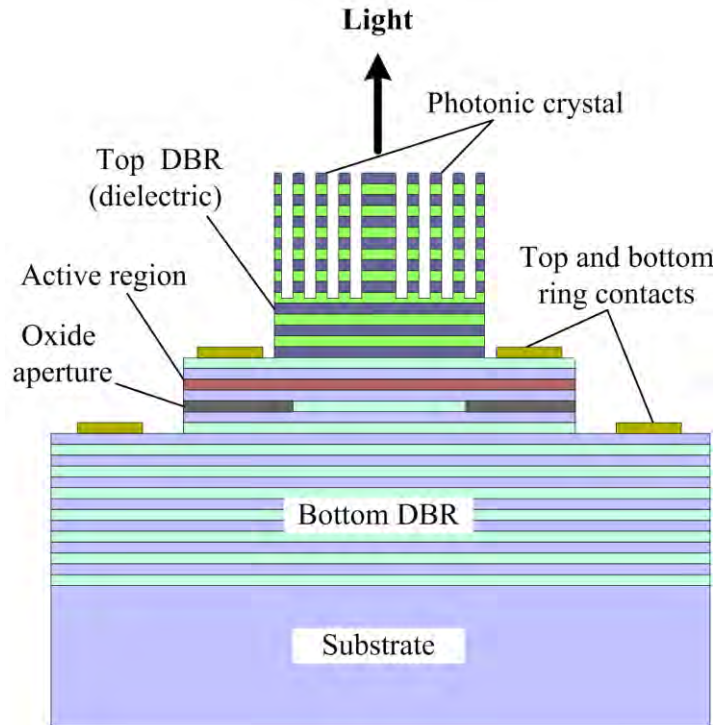


Fig. 3.3. Side view sketch of polarization modulation VCSEL with top dielectric DBR mirror.

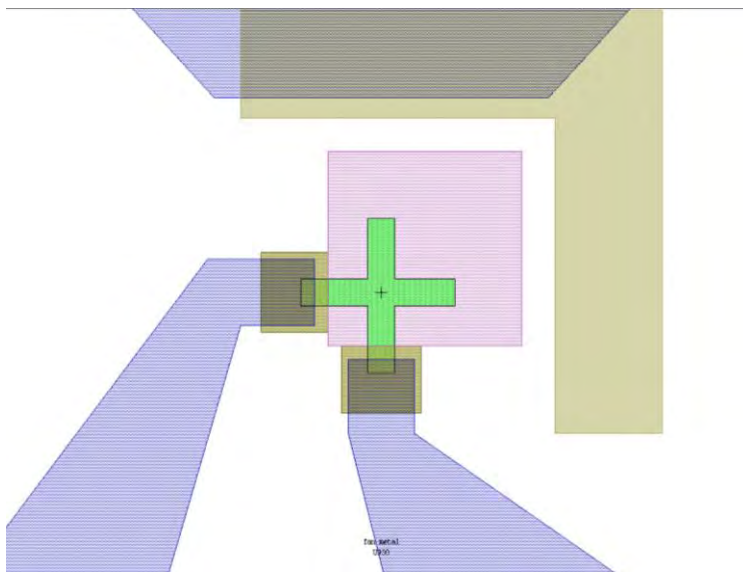


Fig. 3.4. Sketch of example device from the revised masks: smaller implant (green layer) and top DBR mirror pattern (light purple).

Prototype dielectric DBR VCSEL Fabrication and Characterization

Using epitaxial material with a lower semiconductor DBR and active region (i.e. "half VCSEL") round VCSELs were fabricated to confirm the viability of the material and to provide Hypres with samples for low temperature testing. Shown in Fig. 3.5(a) is a side view sketch showing the top contact under the dielectric DBR, while Fig. 3.5(b) shows an optical microscope view of the fabricated devices. Note in Fig. 3.5(b) the adjacent metal contact pads have an extra thickness of 3 μm of Au to enable wire bonding.

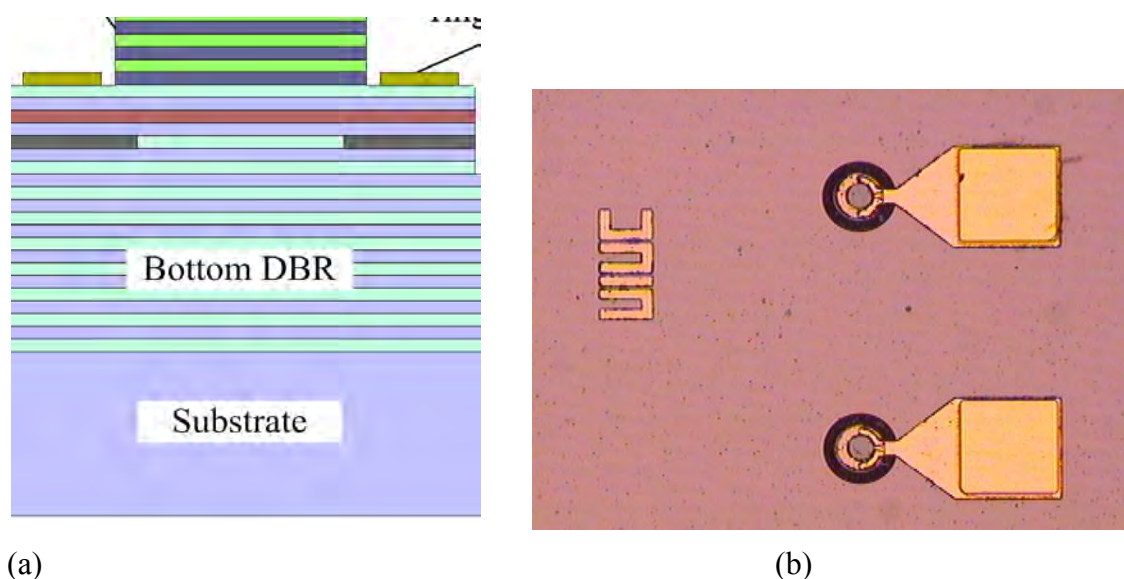


Fig. 3.5. (a) Side view sketch of VCSEL with top dielectric DBR mirror; and (b) optical image.

Fig. 3.6 is a plot of the reflectivity at normal incidence for the top dielectric DBR. The mirror consists of 6 periods of $\text{TiO}_2/\text{SiO}_2$. Initial attempts to deposit these layers were carried out at the University of Illinois, but it was ultimately decided to utilize a commercial vender (KLab in New Jersey). Shown in Fig. 3.7 are the light and voltage versus injection current for the fabricated dielectric DBR VCSELs. Note the slope change to the voltage curves at lasing threshold (e.g. approximately 3 mA in Fig. 3.7(a)). The finite voltage drop observed at currents less than threshold current arises from current leakage in these devices. This in turn arises from the deficiency in the current isolation in the VCSEL, which will be rectified in the polarization modulation VCSELs with the revised implantation mask. Device die of dielectric DBR VCSELs with various aperture sizes were provided to Hypres on April 30, 2012. Specifically approximately 10 die of 10, 15, and 5 μm aperture VCSELs, where each die contained 3 rows of 10 identical VCSELs. These samples were subsequently tested by Hypres at cryogenic temperatures to determine their operating characteristics and to verify their viability at low temperature.

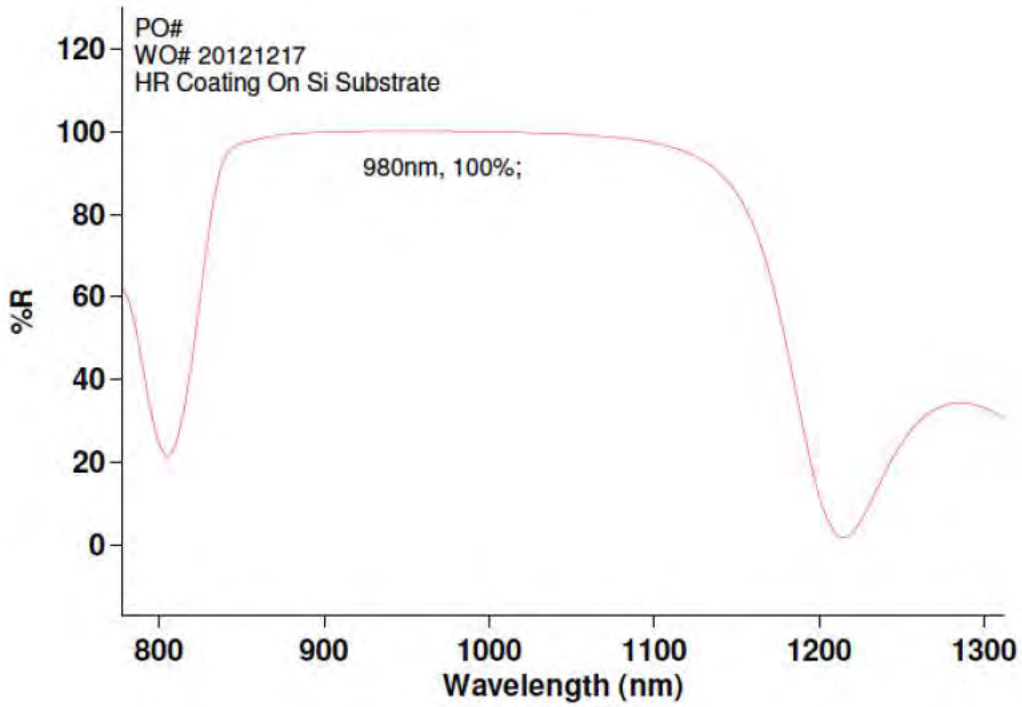
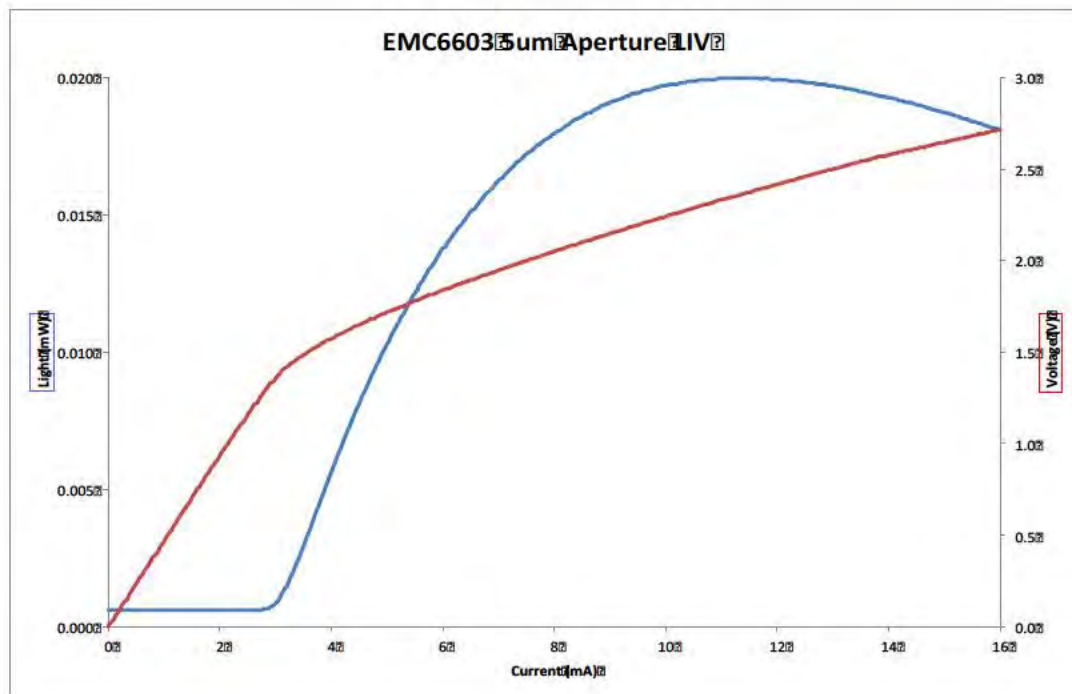
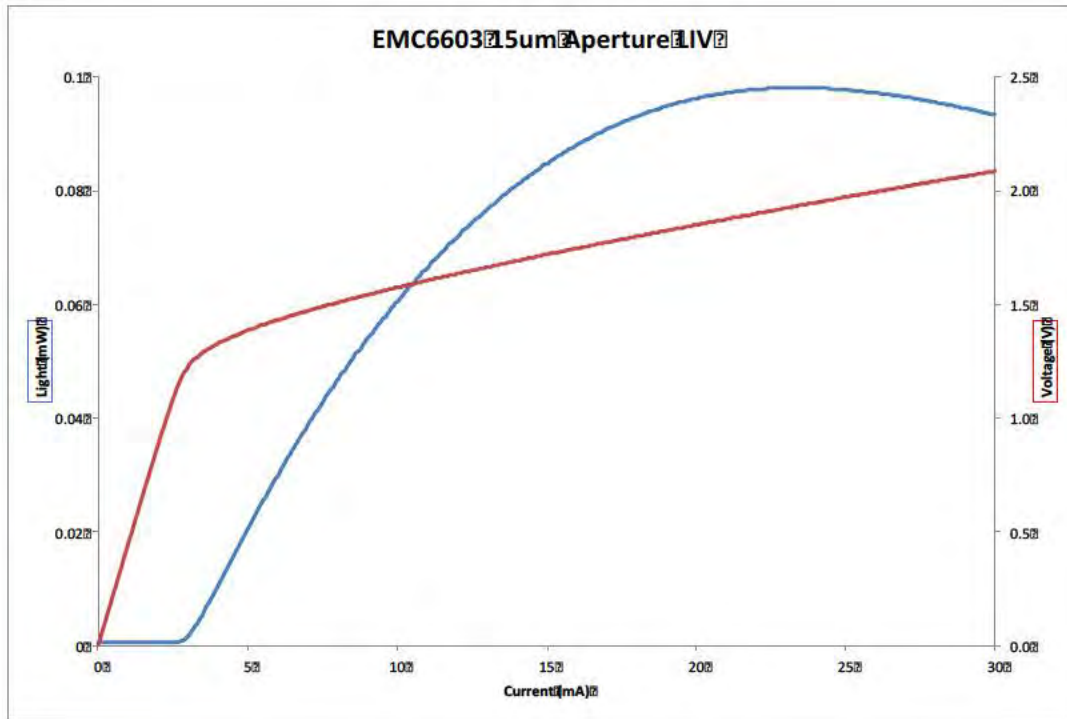


Fig. 3.6: Reflectance spectra of dielectric DBR deposited by KLabs showing high reflectivity at 980 nm.



(a)



(b)

Fig. 3.7: Light and voltage versus injection current for dielectric DBR VCSEL with: (a) 5 μm; and (b) 15 μm aperture.



(a)

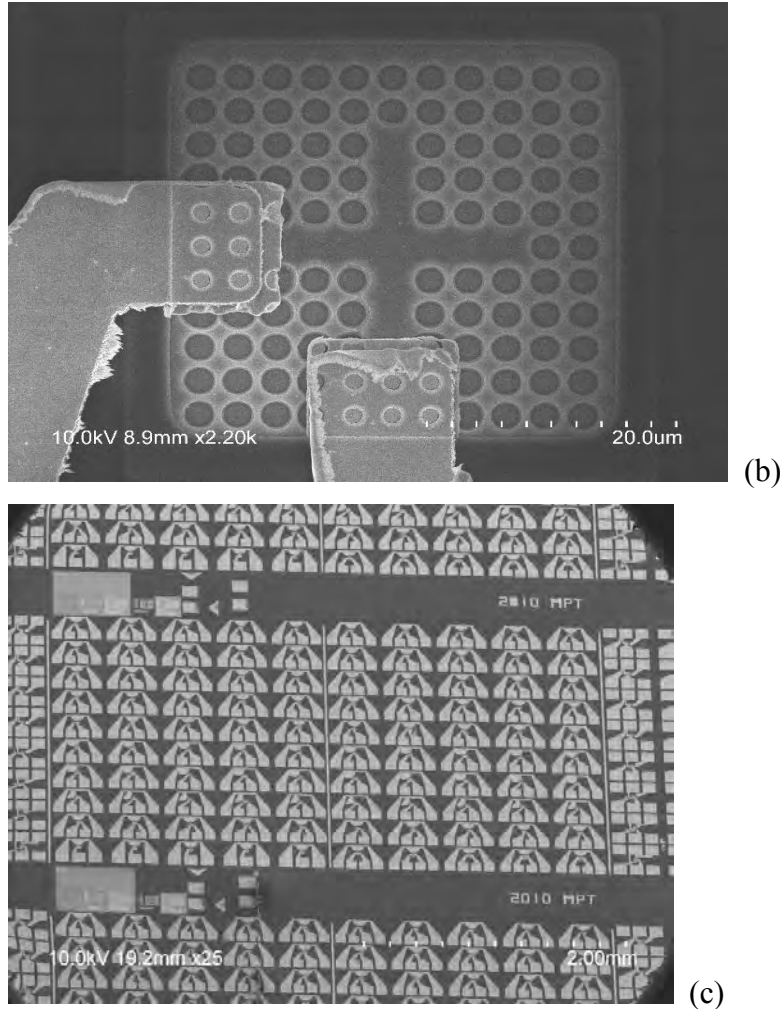


Fig. 3.8: Polarization modulation VCSELs before top mirror deposition: (a) optical image of cruciform device showing electroluminescence in one of the arms of the cruciform cavity; (b) SEM image showing photonic crystal polarization modulation VCSEL; and (c) SEM image of a unit cell of devices.

Fabrication of Dielectric DBR Polarization Modulation VCSELs

Starting in May 2012, the fabrication process for polarization modulation VCSELs began. In the Appendix we show the process follower for this fabrication run. Because of the new device structure (top dielectric DBR), several steps required process development. These included the ion implantation, the polyimide planarization, and the dielectric DBR patterning. Fig. 3.8 shows optical images and scanning electron microscope images of the polarization modulation VCSELs before deposition of the top DBR mirror.

Preliminary testing of these devices before deposition of the top dielectric DBR mirror shows diode current-voltage characteristics, and clear electroluminescence is observed. As evident in Fig. 3.8(a), spontaneous emission with current injection is evident in one of the arms of the cruciform device. Two samples were sent for dielectric DBR mirror deposition. At the present time these devices are undergoing their final processing steps, and laser emission and characterization will begin starting in September.

Cryogenic Test Setup Development

For cryogenic characterization of the fabricated PM VCSELs at low temperatures and demonstrate an entire energy-efficient interface, we developed complete experimental setup to characterize VCSEL at various temperatures ranging from cryogenic temperature of 70K to room temperature of 300K. We constructed a test setup based on the available two stage cryocooler Sumitomo Heavy Industries (SHI) SRDK-101DP-11C. Earlier in this program, we performed the modification of the cryopackage in order to adapt it for VCSEL samples and provide the required temperature control necessary for study temperature-dependence of its performance. During this phase of the program, we specifically performed the following:

- Developed and assembled complete experimental setup to test VCSELs at cryogenic temperatures.
- Developed LabView© software program for automated data acquisition and thorough characterization of VCSELs at cryogenic temperatures.
- Mounted VCSELs at cryostage of the cryocooler with different aperture sizes of 5, 10 and 15 μm . This cryostage with an active temperature control allowing setting operation temperatures in range from $\sim 70\text{ K}$ to $\sim 200\text{ K}$ for VCSEL samples mounted on the first temperature stage. Here we note that, superconducting chips with ERSFQ/eSFQ circuits will be installed at the 2nd (4 K) stage of this cryocooler. Both these stages supplied with their own calibrated thermometers.
- Verified correct operation of complete experimental setup by characterizing VCSELs at room temperature of 300K and cryogenic temperatures in the range of from 70 K to 200 K. VCSELs current-voltage and current-power characteristics have been measured.

We assembled experimental setup comprised of cryocooler with modified cryostage to accommodate VCSELs, temperature controller, optometer, current source and voltmeter all governed by PC for data acquisition and control to evaluate VCSELs at room and cryogenic temperatures. The complete setup is shown in Fig. 3.9a. Fig.1b shows arrangements inside the cryocooler vacuum chamber with chip with multiple VCSELs (see Fig. 3.10) facing down an optical detector connected by low-noise coaxial cable to an optometer.

Before testing began the chip containing the VCSEL samples was secured to an OFHC mount and PCB using a conductive aluminum paste which is shown in Fig. 3.10. Once the chip is glued, each VCSEL sample to be tested is wire bonded to the PCB. In order to supply current from room temperature current source, flat connectors are soldered connected by wires to room temperature for measurements.

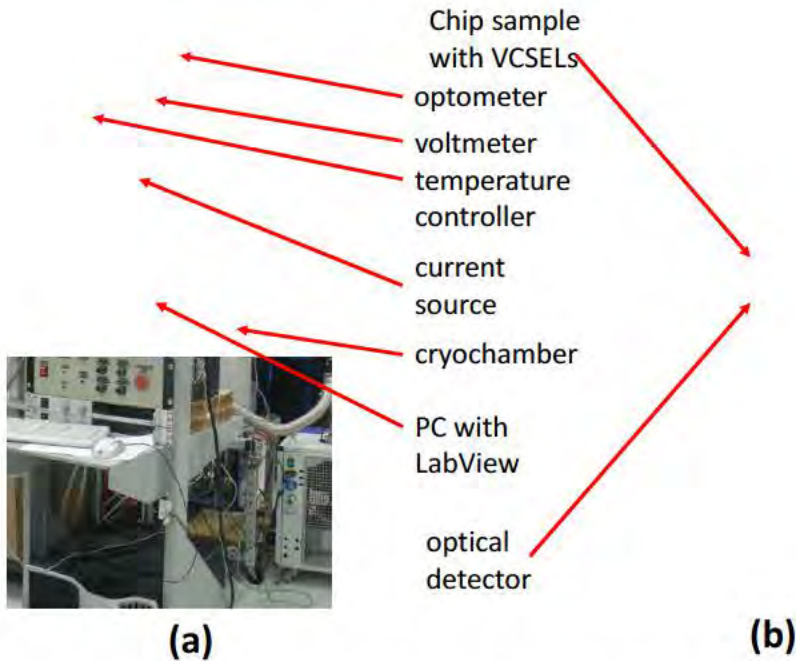


Fig. 3.9. Complete experimental setup to characterize VCSELs from cryo- to room temperature:
 (b) Chip with VCSELs

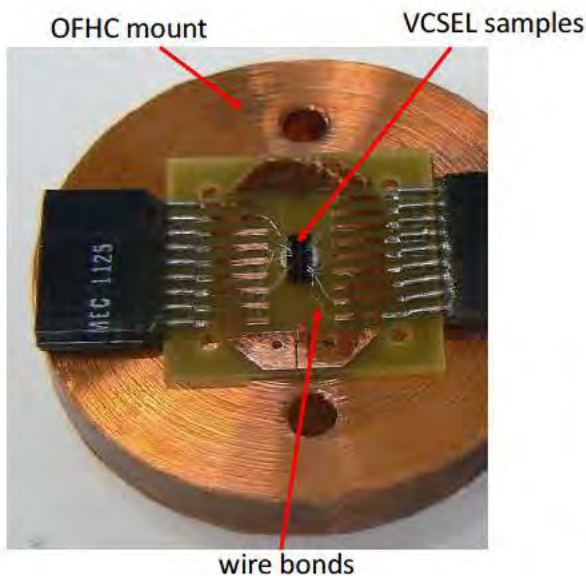


Fig. 3.10. Chip with VCSEL samples glued to OFHC mount and wire bonded to PCB.

All experimental instruments were connected via a GPIB interface to a PC. Data collection itself was done using custom program created using LabView©. The software (screenshot shown in Fig. 3.11) requires the user to choose a starting current, a step current, and a final current so that the current source can run a DC current sweep for single VCSEL while measuring voltage and optical responses. By taking advantage of the GPIB network, the instruments are able to respond to one another, and take readings in synced intervals, as directed by the LabView© program.

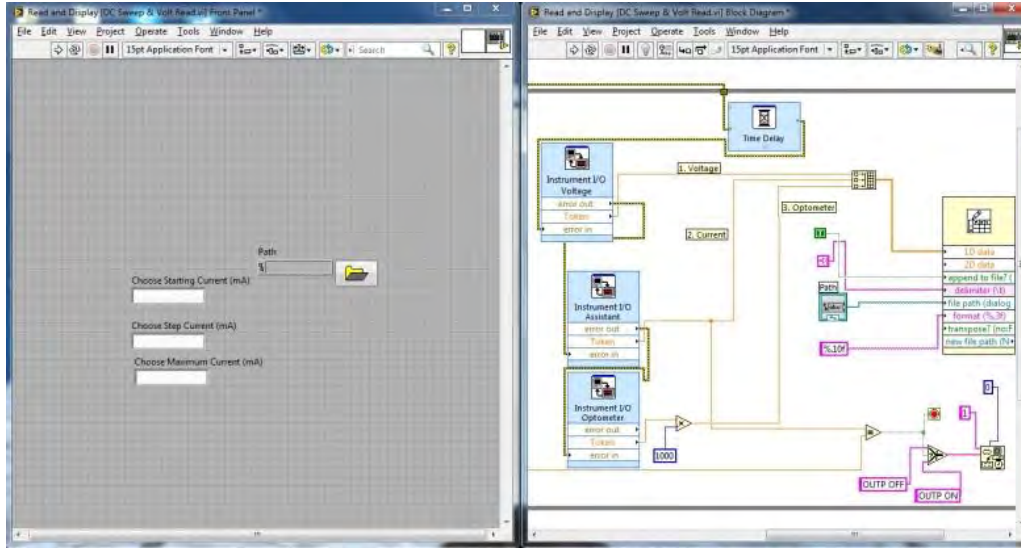


Fig. 3.11. Screenshot of LabView data acquisition program.

To verify our experimental setup and LabView data acquisition program we have measured three conventional VCSEL samples with different aperture of 5, 10 and 15 μm . We measured the same set consisting of current-voltage and current-power characteristics for all VCSEL samples. Fig. 3.12a shows typical current voltage and current-power characteristics for particular 15 μm sample (d_Y1) taken at 300 K. The VCSEL' current-voltage characteristic did not change much with temperature: slight changes in voltage were caused by change in lead resistance. Fig. 3.12b presents current-power dependencies for different VCSEL temperatures - from cryogenic to room temperature ones showing increase of lasing threshold with lowering of the temperature.

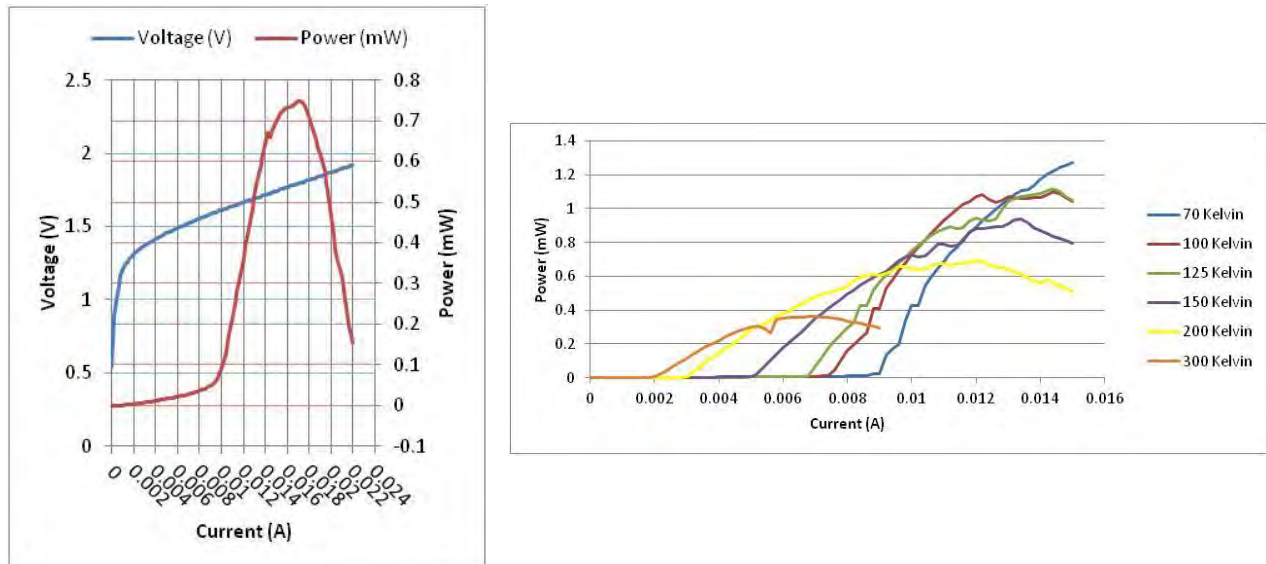


Fig. 3.12 (a) Current-voltage and current-power characteristics for d_Y1 15 μm VCSEL measured at 300 K. (b) Current-power characteristics for d_Y1 15 μm VCSEL measured at different temperatures.

Development of Energy-Efficient on-chip Drivers

In the project, we worked on the lowest power, fastest and smallest area drivers - SFQ-to-dc (or SFQ/dc) converters, to modulate VCSEL polarization. In order to increase energy efficiency, we have converted this SFQ-to-dc converter to ERSFQ logic. The standard RSFQ SFQ/dc converter consist of a flip-flop and output junction pair generating output voltage depending on a state of the flip flop. Typically, a toggle flip flop (TFF) is used. If the conversion of TFF from standard RSFQ to ERSFQ is relatively straightforward, biasing for the output junction pair is not obvious as its output voltage should exceed the voltage on a clock line. During the previous project periods, we invented a solution to this problem by feeding output pair of the SFQ/dc converter off the VCSEL device via the connecting data cable (see Fig. 3.13). The test circuits were designed for HYPRES conventional 4.5 kA/cm² fabrication process.

In this project period, we fabricated the ERSFQ SFQ/dc converter with output stage biasing enabled via output data line from the VCSEL. Fig. 3.14 shows a micrograph of integrated circuit fragment with the designed test circuit consisting of dc/SFQ converter, Josephson Transmission Line (JTL) and the ERSFQ output SFQ/dc converter. The dc/SFQ and JTL are made in standard RSFQ logic to reduce risk, while the SFQ/dc converter is designed using ERSFQ logic approach. Fig. 3.15 shows the results of experimental evaluation demonstrating the correct operating of this circuit.

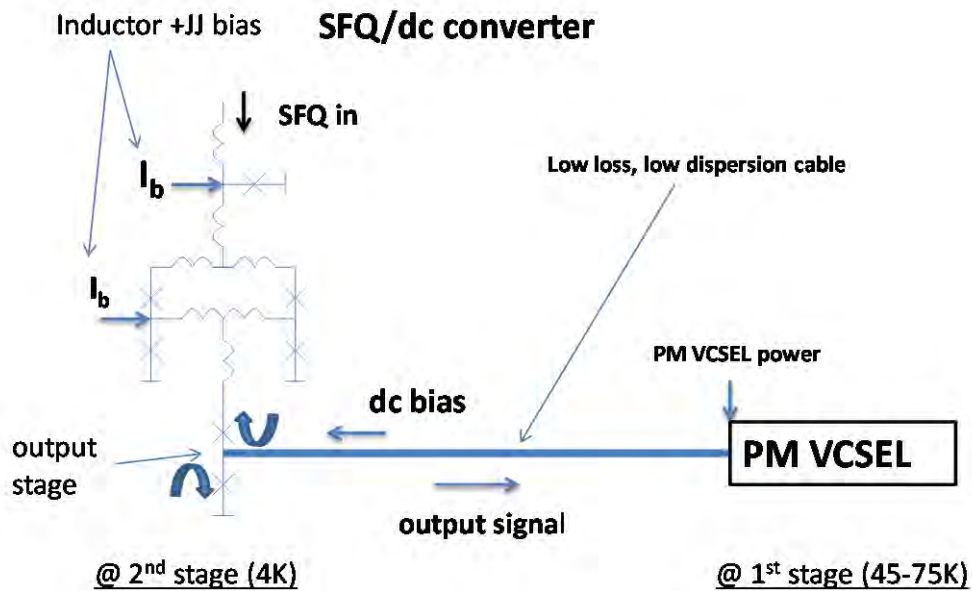


Fig. 3.13. A new ERSFQ SFQ/dc converter with output junction pair fed via output data cable connecting SFQ/dc converter and VCSEL.

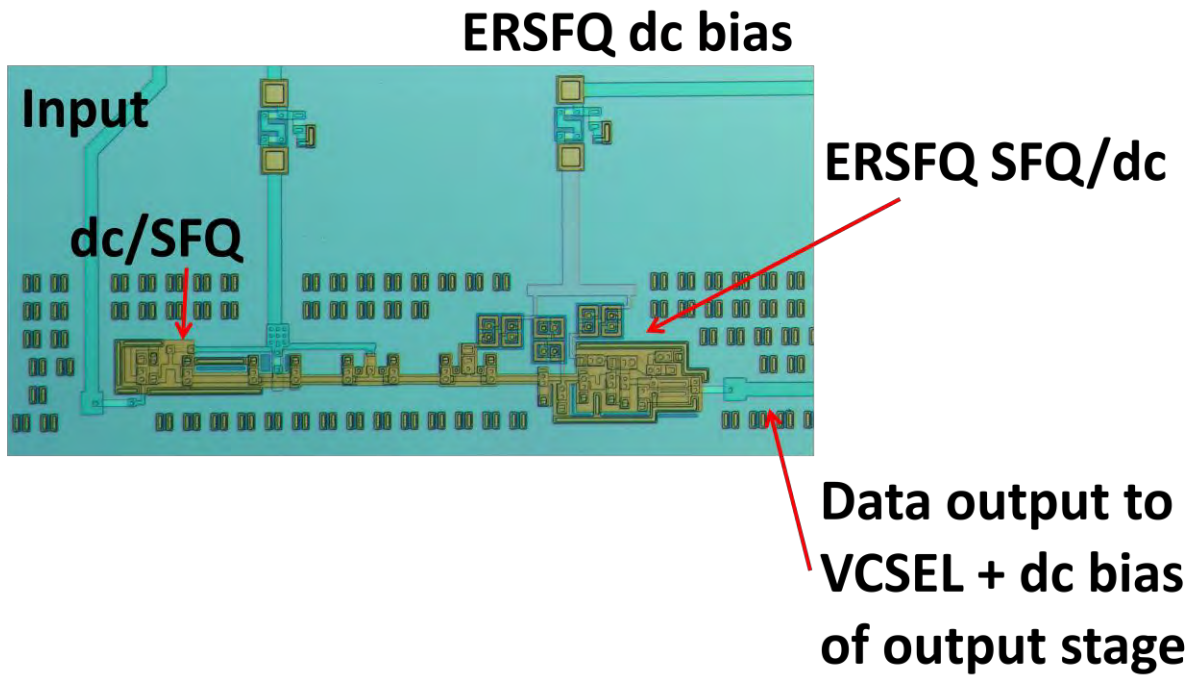


Fig. 3.14. Micrograph of the fabricated test circuits with a new ERSFQ on-chip driver (SFQ/dc converter) integrated with input circuitry (dc/SFQ converter and Josephson Transmission Line (JTL) for the driver operation and verification.

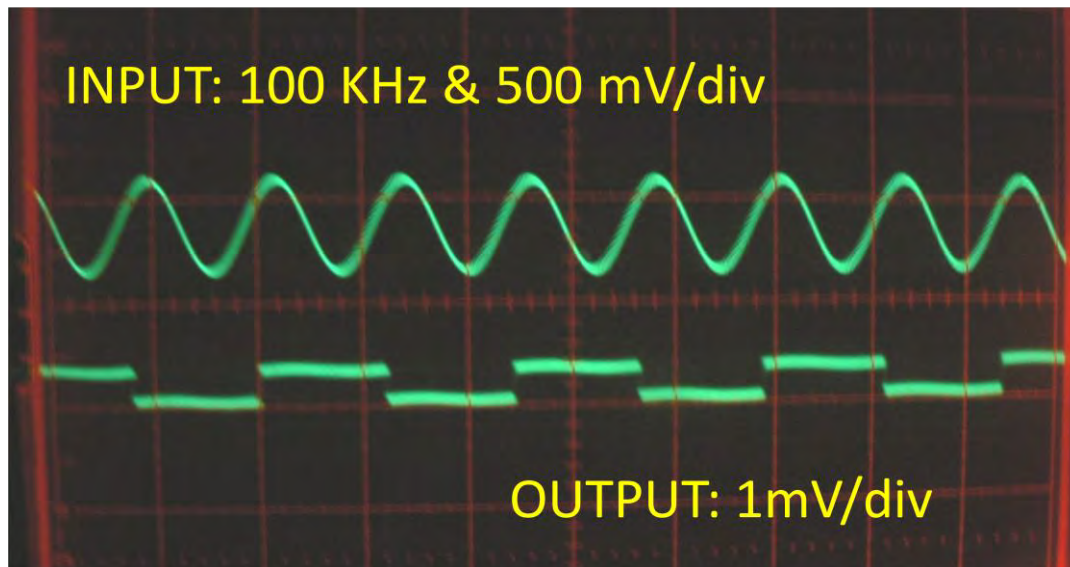


Fig. 3.15. Correct operation of ERSFQ SFQ/dc converter with output stage biasing implemented via output data line.

Superconducting Ferromagnetic Random Access Memory Development

The goal of this additional task is to perform two tasks in the development of a 4K Superconducting Ferromagnetic MRAM circuits compatible with Josephson junction digital energy efficient SFQ circuits. Task 1 focuses on the development of a scalable, energy-efficient memory element based on Magnetic Josephson junctions (MJJs) with either one (superconductor-insulator-superconductor-ferromagnetic-superconductor (SISFS) MJJ) or two (superconductor-insulator-superconductor-ferromagnetic-superconductor-ferromagnetic-superconductor (SISFsFS) MJJ) ferromagnetic layers. For SISFS MJJ, we demonstrated earlier the memory properties of two memory states with different critical current values and high I_{cRn} comparable to that of conventional SIS Josephson junctions. Task 2 is devoted to the demonstration of a superconducting ferromagnetic transistor (SFT) – a three-terminal device with good input/output isolation for integration with MJJ-based memory cell. and capable of performing the memory cell selector function in random access memory arrays.

Summary of the project accomplishments

In this project, we have achieved the following results:

1. Successful demonstration of the SISFS MJJ memory element with the reduced dimensions $2\ \mu\text{m} \times 2\ \mu\text{m}$ as compared to the previously demonstrated $10\ \mu\text{m} \times 10\ \mu\text{m}$ MJJ.
 - a. Fabricated a set of $2 \times 2\ \mu\text{m}^2$ SISFS MJJs with a Nb-Al/ AlO_x -Nb-PdFe-Nb structure using HYPRES/InQubit co-fabrication approach.
 - b. By applying external magnetic field pulses and biasing MJJ with the appropriate Read current, both Write and Read operations showing switching between “0” and “1” states for SISFS MJJ were demonstrated.
2. Development of the SISFsFS MJJ memory element scalable to sub- μm dimensions.
 - a. As a first step here, we fabricated a set of $10 \times 10\ \mu\text{m}^2$ SFsFS MJJs with Nb-PdFe-Nb-PdFe-Nb structure.
 - b. Demonstrated a 2.8% difference in magneto-resistive measurements between parallel (P) and anti-parallel (AP) orientation of ferromagnetic layers.
3. Development of a memory cell selector – a superconductor-ferromagnetic transistor (SFT) with high input-output isolation.
 - a. Fabrication of single and double-acceptor SFIFSIS superconducting ferromagnetic transistors.
 - b. Demonstration of a critical current modulation for SFT acceptor by applying current through the SFT injector for the single-acceptor SFTs. This is required for SFT input/output isolation to realize MJJ memory cell with the integrated SFT cell selector.
 - c. Demonstration of a voltage gain above 25 and perfect input/output isolation for double-acceptor SFT.

Our proposed memory cell designs takes advantage of the distinct and unique characteristic of our MJJs – the fast switching time comparable to that of conventional SIS JJs employed in low-power fast SFQ circuits. This feature allows us to avoid using the SIS JJ based readout SQUID elements integrated in memory cells restricting the memory cell scalability and the overall RAM array density. In order to achieve the fast switching time of MJJs, we combine a fast SIS junction with a magnetic SFS junction in a single tunnel structure [1-4].

This leads to the ability to utilize MJJs as fast-switching Josephson junctions with programmable critical current – the new feature in superconducting electronics not available in the past. Such MJJs can be directly used for memory cells and programmable logic in the most area efficient way without area consuming SQUIDs and/or additional SIS junctions. The memory cell can now be read out by direct electrical switching this MJJ. As a result, the memory cell area will be determined by the scalable MJJ rather than auxiliary SIS JJs leading to a very dense memory array – one of the prime motivations for the cryogenic MRAM development. Even relatively large MJJ (e.g. $2 \times 2 \mu\text{m}^2$) can be quite competitive, since it does not require any additional SQUIDs.

In contrast, the known alternative approaches of using superconducting–ferromagnetic junction as programmable pi-shifters lead to the necessity to integrate them with additional SIS junctions to form SQUIDs, etc. Such memory cells have to be readout by switching additional SIS junctions, since these 0-pi phase shifters are too slow (MHz-range) to be readout directly. As a result, the memory cell area will be determined not by the scalable MJJ area but by the SQUID area made of resistively shunted SIS junctions and geometrically large inductors, which compromise the memory cell density.

Our fast MJJs are to be employed in two possible memory cell designs, which we developed at no cost to this project as HYPRES' internal R&D effort. These designs are the subject of a patent application. Both memory cell designs allow the energy-efficient, small area, and fast memory cells suitable for dense, scalable MRAM applicable for cache, main memory and even naturally extendible for multi-port register files. The first design is a single-MJJ cell with a ballistic SFQ readout (SFQ-MJJ memory cell). The second design follows a typical MRAM memory cell configuration, in which with a single MJJ storage element is combined with a 3-terminal SFT cell selector (SFT-MJJ memory cell).

In this project, we focus on two highest-priority tasks:

- Scalable (below $1 \mu\text{m}$) magnetic Josephson junction with two ferromagnetic layers for the use as a storage element of memory cell.
- Superconducting–ferromagnetic transistor (SFT) with good input/output isolation for the use as a memory cell selector.

Fabrication and characterization of scalable MJJ memory element for cryogenic memory

The specific objective of the HYPRES/InQubit group effort is to explore scalability of MJJ memory elements starting from the already demonstrated $10 \times 10 \mu\text{m}^2$ memory elements. The goals of this project are to optimize the MJJ design and fabrication procedure to realize MJJ minimal (optimally sub- μm) dimensions while retaining their main properties (high $IcRn$ product, ability to write-in and retain information, etc.) required for application as a memory

element. At the beginning of this project, we planned to optimize the MJJ memory element with single ferromagnetic layer (SIsFS) and scale it to $\sim \mu\text{m}$ dimensions. To scale the MJJ memory element further to the sub- μm dimensions, we introduce additional sF layers. This progression is depicted in Fig. 5.1. Thickness of the additional 's' layer should ensure its superconductivity assisted by an opposite orientation of the magnetization vectors of F films with significant (complete) suppression at their parallel (P) orientation (see Fig. 5.2). In the first case, with opposite (AP) orientation of F layer magnetizations, the SIsFsFS device can be decomposed to a series connection of SIs tunnel junction with sFs and s-F-S sandwiches with higher I_c for a whole structure. In the second case, with co-aligned (P) magnetization of F layers, the s layer between two F layers transitions into the normal state significantly decreasing structures' I_c .

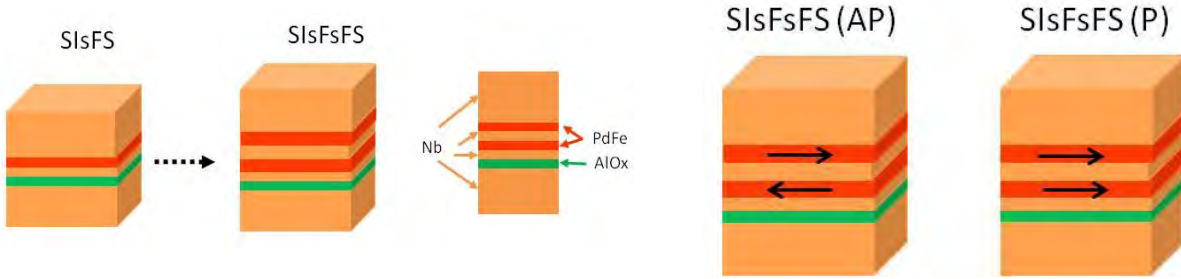


Fig.1. MJJ memory element progression.

Fig.2. SIsFsFS memory element in AP and P states.

This report covers the research activity for the period from September 13, 2013 to August 30, 2014. The subtasks were:

- Sub-Task 1.1: Fabrication of SIsFS MJJ with $2 \times 2 \mu\text{m}^2$ dimension using earlier established HYPRES/InQubit co-fabrication approach (details follow).
- Sub-Task 1.2: Characterization (I - V curves, $I_c(H)$, switching curves, etc.) of MJJs produced in sub-task 1.1 for the application as a cryogenic memory element.
- Sub-Task 1.3: Selection of the optimal parameters, e.g., layer thicknesses for two ferromagnetic layers and superconducting layers between them for SIsFsFS memory element.
- Sub-Task 1.4: Fabrication and characterization of SFsFS MJJ produced with layer thicknesses selected in sub-task 1.3.

2.1 Fabrication of SIsFS MJJs

Our fabrication process is based on the established and proved HYPRES/InQubit co-fabrication approach. The fabrication was split into two major steps. Firstly, we produced a series of 150-mm wafers with an in-situ deposited Nb-Al/AIO_x-Nb trilayers with 4.5 kA/cm² target Josephson critical current density. The wafers were then diced into 15 x 15 mm² samples and transferred to the InQubit/ISSP for subsequent deposition of a ferromagnetic layer (Pd_{0.99}Fe_{0.01}) and top Nb counter electrode. The resultant structure is of a SIsFS type. For the SIs fabrications, the thickness of the counter electrode was 20 nm whereas for Nb base electrode thickness was 120 nm. At the InQubit facility, the samples were cleaned in acetone/methanol/IPA and blow dried with N₂ gas. In-situ Ar sputter etching was used to remove about 10 nm of Nb oxide layer before depositing ferromagnetic layer. The PdFe/Nb bilayer was deposited using rf- and dc-magnetron

sputtering. The PdFe layer was 25nm thin, enough to avoid significant critical current suppression. The top Nb layer thickness was about 150 nm to ensure uniform supercurrent flow through a Josephson junction. Then, we formed a square mesa of $2 \times 2 \mu\text{m}^2$ sizes by photolithography, reactive ion etching (RIE) of the top Nb layer and argon plasma etching of PdFe and Al/AlO_x layers, and patterned the bottom Nb-electrode with photolithography and RIE. At the third step, we formed an isolation layer with a contact (wiring) window by using thermal evaporation of SiO and a lift-off process. Junction contact size in SiO layer was $4 \times 4 \mu\text{m}^2$. At the last step we formed Nb wiring electrode of 450 nm thickness using magnetron sputtering and a lift-off. We used argon RF-etching to ensure a good interface transparency between the wiring and the top Nb electrode of the mesa. The resultant structure is shown in Fig. 5.3.

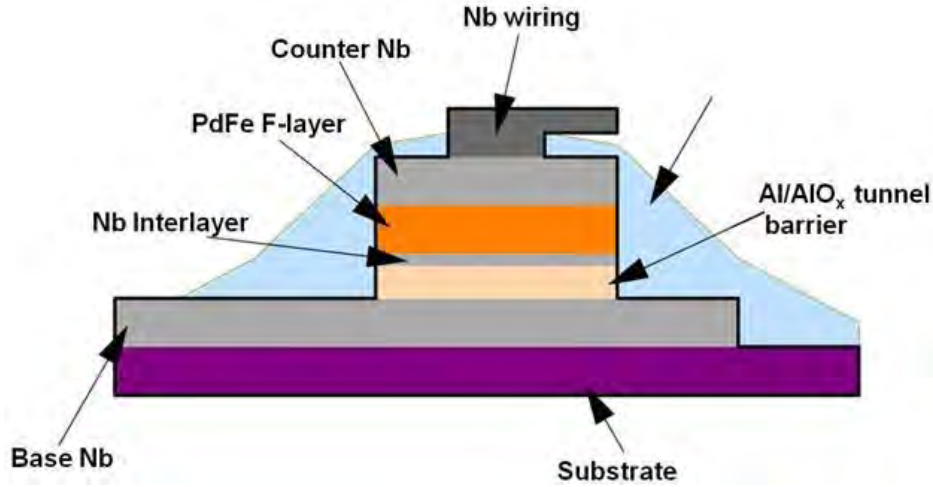


Fig. 5.3. The MJJ structure produced using HYPRES/InQubit MJJ co-fabrication process.

2.2 Characterization of $2 \times 2 \mu\text{m}^2$ SISFS MJJ samples

All SISFS measurements were performed in a variable temperature liquid He cryostat. The sample holder was placed in a vacuum can with He gas added for better heat exchange. The sample temperature was controlled using a carbon thermometer and a compact heater wound by a twisted pair and glued close to the sample. Fig. 5.4 shows the measured current-voltage characteristics (CVC) of SISFS MJJ at 4.2 K temperature. The unshunted MJJ is susceptible to the external noise and premature switching to voltage state. To measure MJJ critical current I_c , the post-process shunting by 0.01Ω resistor made of Al wire was performed and CVC shown in Fig. 5.4 was obtained. With critical current density of 4.5 kA/cm^2 , the expected I_c for MJJ with dimensions of $2 \times 2 \mu\text{m}^2$ is about $180 \mu\text{A}$. Critical current $I_c = 60 \mu\text{A}$ at 4.2 K shown in Fig. 5.4 can be explained both by degradation of quality of Nb in intermediate s-layer due to excessive Ar ion cleaning and suppression of superconductivity in MJJ by ferromagnetic. As expected, the I_c of MJJ under investigation rose up while junction temperature was decreased reaching $I_c = 165 \mu\text{A}$ for $T = 2.1 \text{ K}$ (see Fig. 5.5).

The switching experiment was performed for a $2 \times 2 \mu\text{m}^2$ unshunted MJJ device at temperature $T = 3.4 \text{ K}$ with I-V-curve presented in Fig. 5.6. An application of small external magnetic field changed the magnetization of the ferromagnetic layer that in turn changes the junction I_c , allowing the realization of two distinct states with high and low I_c , corresponding to logical “0” and “1” states, respectively. Thus, one can choose a junction bias current ($I_{\text{read}} = 75 \mu\text{A}$) to switch the SISFS MJJ from a superconducting to a resistive state by a pulse of magnetic field.

This experiment is presented in Fig. 5.7, where positive and negative magnetic field pulses switch the SISFS junction from a superconducting (zero-resistance) or “0” state to a resistive or “1” state and back.

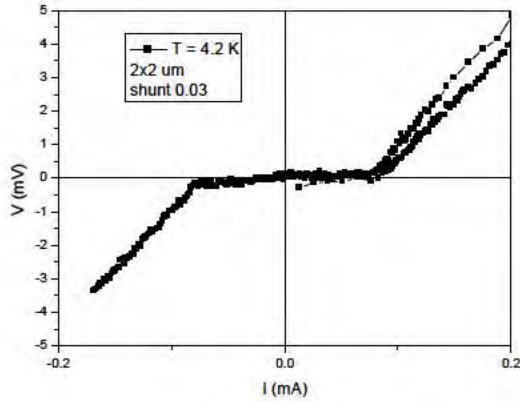


Fig. 5.4. Current-voltage characteristic (CVC) of $2 \times 2 \mu\text{m}^2$ SISFS MJJ externally shunted with 0.03Ω resistor taken at $T = 4.2 \text{ K}$.

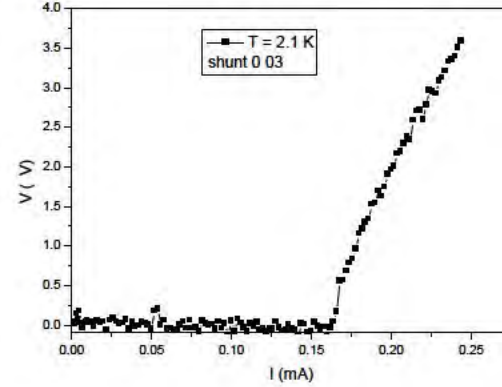


Fig. 5.5 CVC of $2 \times 2 \mu\text{m}^2$ SISFS MJJ externally shunted with 0.03Ω resistor taken at $T = 2.1 \text{ K}$.

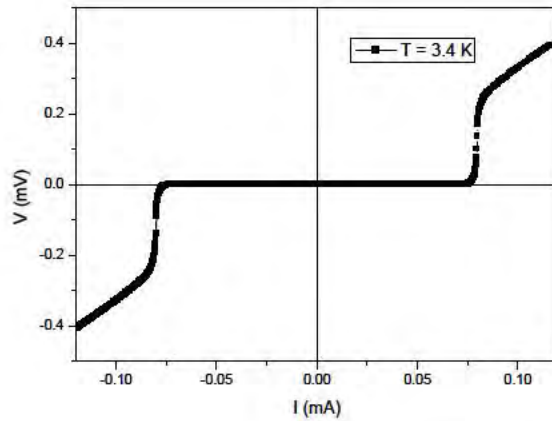


Fig. 5.6. I-V characteristic (CVC) of $2 \times 2 \mu\text{m}^2$ unshunted SISFS MJJ taken at $T = 3.4 \text{ K}$.

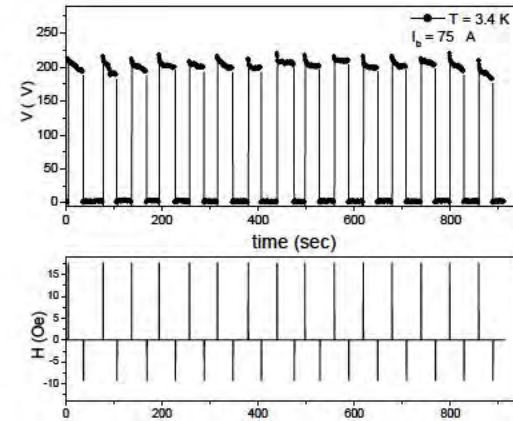


Fig. 5.7. Confirmation of Write/Read operation: switching of SISFS MJJ between “0” and “1” states by remagnetization with external magnetic field. $V(t)$ – average junction voltage, $H(t)$ – applied magnetic field.

1.3 Selection of parameters for SISFS MJJ memory element for cryogenic memory

2.3.1 Thickness of the ‘s’ interlayer between two ‘F’ layers

First, we have to find the optimal thickness of Nb interlayer between two ferromagnetic $\text{Pd}_{0.99}\text{Fe}_{0.01}$ layers. This Nb interlayer has to be thin enough for whole structure to operate as a single MJJ. Additionally, it has to be thick enough for its superconducting properties not to be completely suppressed by proximity effect from neighboring ferromagnetic layers.

We fabricated and studied (FsF) PdFe-Nb-PdFe trilayer with thicknesses of PdFe layers of 20 nm and 25 nm. We observed that with the Nb interlayer of 15 nm this trilayer has critical temperature of $T_c=2.62$ K (see Fig. 5.8) which proves that in this case superconducting properties of Nb are strongly affected by proximity effect from ferromagnetic PdFe. For trilayer with Nb interlayer thickness of 10 nm, $T_c < 1$ K was measured, making it unpractical. Larger thickness of Nb interlayer is required.

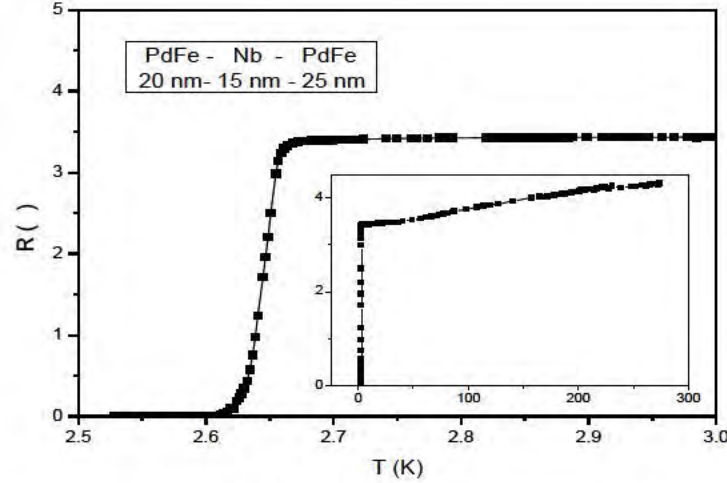


Fig. 5.8. Superconducting transition for PdFe-Nb-PdFe (20 nm-15 nm-25 nm) trilayer affected by proximity effect.

2.3.2 Thicknesses of ferromagnetic ‘F’ layers

As a next step, we are finding the thicknesses for ferromagnetic layers to realize AP and P states with higher and lower I_c , respectively. We, first, try to realize AP and P states in MJJ with two F-layers of $\text{Pd}_{0.99}\text{Fe}_{0.01}$ of different thickness. We study $I_c(H)$ magnetization curves for SIsFS (Nb-Al/AlOx-Nb-PdFe-Nb) MJJs co-fabricated by Hypres/InQubit/ISSP as described in section 2.1.

Figs. 9-12 show hysteretic dependences of critical current I_c on magnetic field for SIsFS MJJs with a 20 nm ferromagnetic layer (Figs. 9 & 11) and a 25 nm ferromagnetic layer (Figs. 10 & 12). Figs. 9-12 demonstrate a typical Fraunhofer-like $I_c(H)$ dependence of MJJ critical current on external magnetic field H aligned parallel to the layers within the MJJ and supplied by an external solenoid. For each measured point of the $I_c(H)$ curve, the current through the sample is swept from a subcritical value upwards until the threshold voltage is exceeded while the external magnetic field is fixed. For all $I_c(H)$ dependencies magnetic field sweep directions are shown by arrows in Fig. 5.9.

From Fig. 5.9, one can conclude that coercive field for the 20 nm F-layer at temperature $T = 2.5$ K is $H_c \approx -2.2$ Oe. Coercive field by the MJJ is defined by the magnetic field when both magnetic induction B and magnetic flux Φ of the MJJ are zero. Consequently, the critical current of the MJJ should beat its maximum in the coercive field. Similarly, from Fig. 5.10, one can conclude that coercive field for the 25 nm F-layer at temperature $T = 2.5$ K is $H_c \approx -3.35$ Oe.

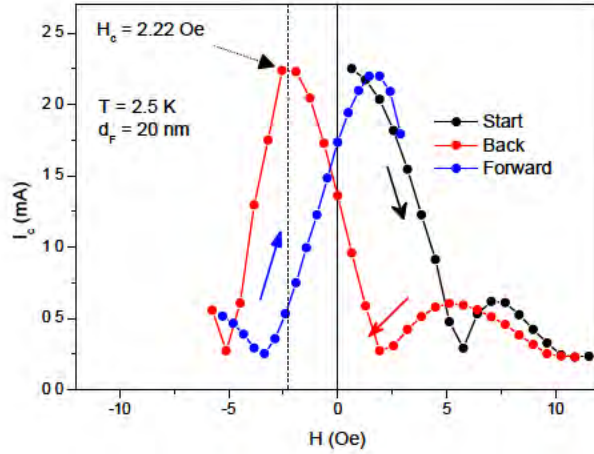


Fig. 5.9. $I_c(H)$ dependence for Nb-Al/AlOx-Nb-PdFe-Nb SIsFS MJJ with a 20 nm ferromagnetic layer.

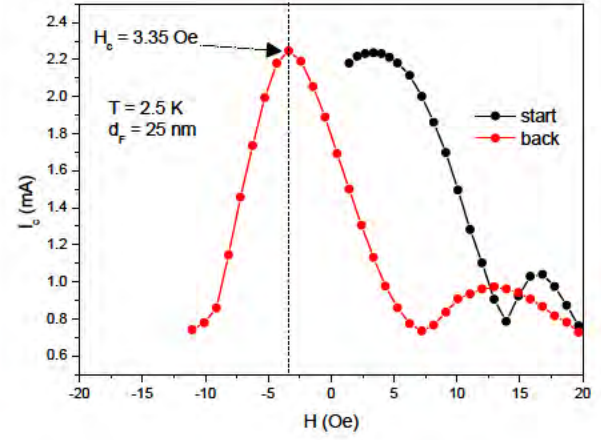


Fig. 5.10. $I_c(H)$ dependence for Nb-Al/AlOx-Nb-PdFe-Nb SIsFS MJJ with a 25 nm ferromagnetic layer.

$I_c(H)$ hysteretic dependence in Fig. 5.11 shows that for a full remagnetization MJJ with a 20 nm PdFe has to be placed in an external magnetic field higher than 5.2 Oe. At the same time, Fig. 5.12 shows that the fully magnetized MJJ with 25 nm PdFe remains magnetized at zero field. Fig. 5.12 was measured sweeping external magnetic field from very large positive $H \approx 25$ Oe (ensuring PdFe full magnetization) to $H \approx -5.2$ Oe and then back to $H \approx 25$ Oe. For red $I_c(H)$ curve, at ≈ -2.2 Oe zero magnetic field, I_c is suppressed proving that 25 nm PdFe still remains magnetized.

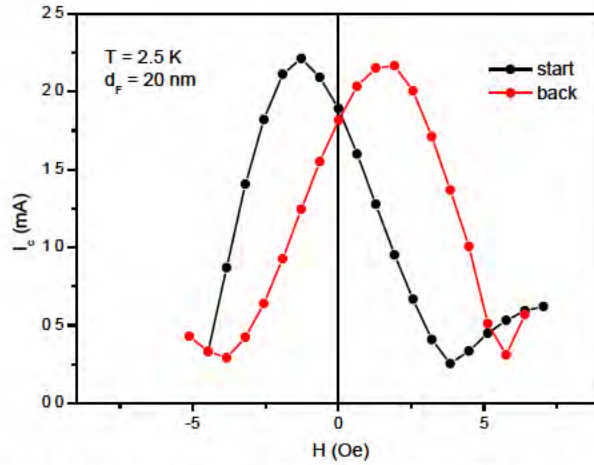


Fig. 5.11. $I_c(H)$ dependence for SIsFS MJJ with a 20 nm ferromagnetic layer.

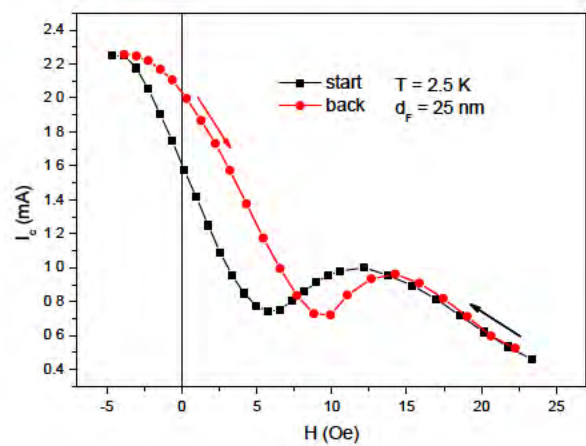


Fig. 5.12. $I_c(H)$ dependence for SIsFS MJJ with a 25 nm ferromagnetic layer.

Therefore, the opposite magnetization for two F-layers can be realized in MJJ with 20 nm and 25 nm PdFe layers. Moreover, to make this magnetization difference even more pronounced, we study MJJ with 20 nm and 30 nm PdFe layers.

1.4 Fabrication and evaluation of SFsFS test MJJs

As a first step towards the development of the fast MJJs based on SIsFsFS, we fabricated and tested simpler SFsFS MJJs with Nb-PdFe-Nb-PdFe-Nb $10 \mu\text{m} \times 10 \mu\text{m}$ structures and respective

layer thicknesses 120-30-15-20-450 nanometers. The Nb-PdFe-Nb-PdFe-Nb (120-30-15-20-150 nm) was formed by rf- and dc-magnetron sputtering and a $10 \times 10 \mu\text{m}^2$ mesa is formed by:

1. Reactive Ion Etching (RIE) of top Nb,
2. Barrier geometry is formed by RIE of PdFe and Nb interlayer,
3. Patterning the bottom Nb-electrode with photolithography and RIE,
4. An isolation layer with a contact (wiring) window by using thermal evaporation of SiO and a lift-off process is formed,
5. Nb wiring electrode of 450 nm thickness using magnetron sputtering and a lift-off is formed.

Fig. 5.13 presents $I_c(T)$ dependencies for SFsFS MJJ with three normalized maxima shown, i.e., the main $I_c(H)$ peak in the demagnetized state as well as the first and second negative $I_c(H)$ peaks in the magnetized state. With the MJJ being cooled, all curves in Fig. 5.13 show crossover at $T \approx 2.25$ K with drastic increase in I_c that reflects s-layer between F-layers becoming superconducting. Fig. 5.13 does not show any effect of stimulation of I_c by the external magnetic field with all peaks (main and secondary) following the same temperature dependence. This might indicate that two PdFe layers acted as a single one. This assumption is confirmed by the fact that the coercive field (H_c) on $I_c(H)$ dependences account for single ~ 50 nm PdFe layer.

Still, we were able to distinguish P and AP states at lowest temperature available in our measurements system (see Fig. 5.14). Fig. 5.14 shows normalized CVCs for SFsFS MJJ in P (solid black) and AP (solid red) states with a magneto-resistive effect of 2.8% difference between P and AP being measured. Since this is not yet sufficient for memory application at $T = 4.2$ K, further material research in optimization this double ferromagnetic layer memory element is required. This may include different composition of PdFe (i.e., the increase of Fe content from current 1%) and/or different thickness(s) of PdFe layers.

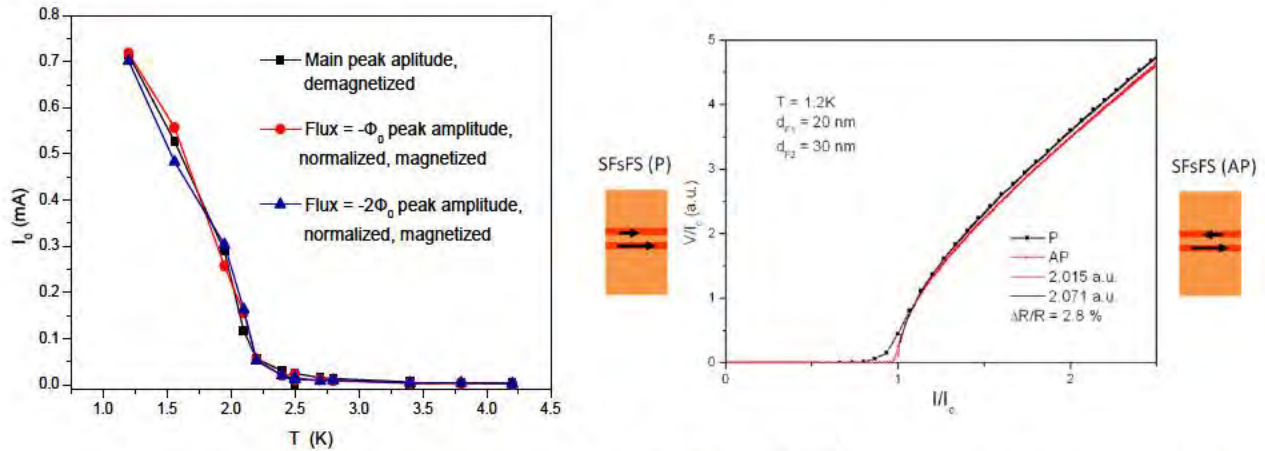


Fig. 5.13. $I_c(T)$ dependence for SFsFS MJJ.

Fig. 5.14. SFsFS MJJ magneto-resistive measurements at $T = 1.2$ K

2. Fabrication and characterization of a Superconductor-Ferromagnetic Transistor (SFT) for MJJ memory cell with integrated SFT cell selector

The specific objective of the HYPRES/Northwestern University (NWU) team effort is to develop a superconducting ferromagnetic SFIFSIS three-terminal device (Fig. 5.15) with a good input/output isolation as a memory cell selector integrated with MJJ. The goal of this task is to prove that SFT has transistor-like properties necessary for the intended use as a memory cell selector. These are: (i) an ability to modulate critical current between two device terminals by injecting current from the 3rd terminal; (ii) a good input/output isolation eliminating a potential half select issue. This device will be based on the SFIFSIS structures, which have already showed good isolation properties [6].

This final report covers the research activity from September 13, 2013 to August 30, 2014. The primary activities were:

- Sub-Task 2.1: Fabricate a set of SFIFSIS SFT devices with the goal to increase input/output isolation and demonstrate the modulation of the acceptor critical current by input current applied to the device injector terminal.
- Sub-Task 2.2: Experimentally evaluate the fabricated SFIFSIS SFT devices to investigate the levels of critical current modulation and input/output isolation in the regime applicable for memory readout process.

3.1 Fabrication of SFIFSIS superconductor-ferromagnetic transistor

In this project period, the focus of our work was on fabrication of superconductor-ferromagnet three-terminal devices and testing their characteristics at 4.2 K. The devices were patterned from SFIFSIS multilayers, where S (superconductor) stands for Nb; F (ferromagnetic material) stands for Ni; and I (insulator) stands for Al/AIO_x. For patterning of these devices, NWU used new photomasks provided earlier by HYPRES at no cost to this project. The goal was, first, to make the contact pads of the same configuration as HYPRES typically uses in order to standardize the chips and make their characterization compatible with HYPRES, and second, to reduce the size of devices.

Here we follow the technique for fabrication of multi-terminal SFIFSIS devices consisting of two stacked junctions developed earlier in NWU. The three-terminal devices were fabricated from Nb(120)/Ni(4)/Al/AIO_x(9)/Ni(4)/Nb(30)/Al/AIO_x(9)/Nb(80) multilayers with numbers in parenthesis indicate nominal thicknesses of the respective layers in nm (for Al/AIO_x it is the initial thickness of unoxidized Al). Anodization and deposition of SiO₂ was used for proper insulation of the electrodes from each other. The structure of a three-terminal SFIFSIS device together with the experimental technique, i.e., the way how bias currents are applied and voltage is measured, is shown in Fig. 5.16. Fig. 5.17 shows the top view microphotograph of the actual single and double-acceptor devices.

We succeeded in fabrication single-acceptor and double-acceptor three-terminal devices superconductor-ferromagnet transistors (SFTs). In latter case two acceptor SIS junctions are placed on top of the same injector SFIFS junction (see schematic side view of the device structure in Fig. 5.16). The devices were made on sapphire substrates. If the two acceptor junctions are measured in series, as shown in Fig. 5.16, then the output voltage is doubled as compared with that in an ordinary single-acceptor device similar to that described in [5]. This

configuration might be favorable if the device is used in the voltage amplifier mode [6], which is useful for investigation of the SFT properties.

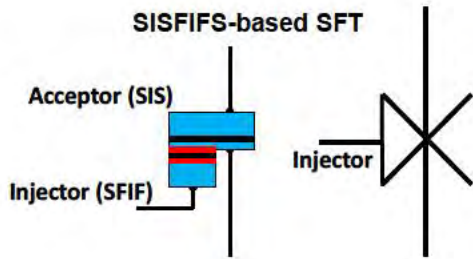


Fig. 5.15. Schematic side view and symbol of the SFT. The choice of cell-selector SFT design with a single or double acceptor will be determined in this project.

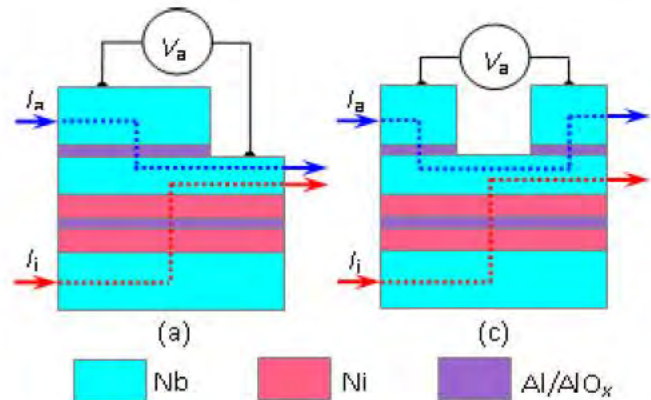


Fig. 5.16. Schematic cross-sectional view and biasing for the single-acceptor (a) and double-acceptor (b) SFT device.

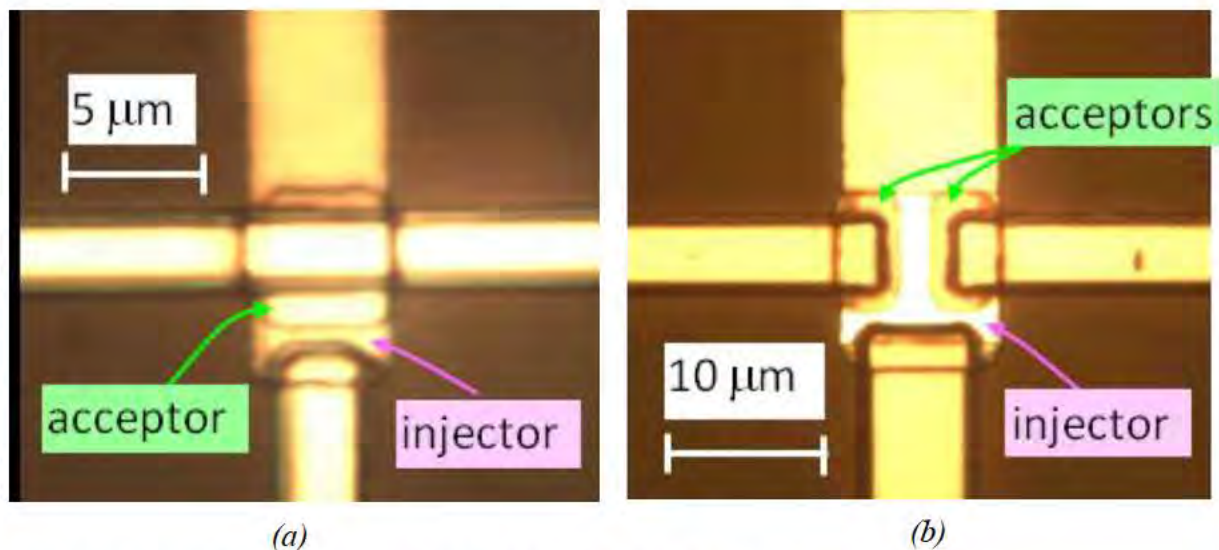


Fig. 5.17. Optical image of actual single (a) and double (b) acceptor SFT devices.

3.2 Evaluation of SISFIFS superconductor-ferromagnetic transistor

We report data for three devices, D1-D3, with some of their parameters being summarized in the Table 1.

Table 1. SFT Device Parameters.

Device No.	Substrate	No. of acceptors	Injector size ($\mu\text{m} \times \mu\text{m}$)	Acceptor size ($\mu\text{m} \times \mu\text{m}$)	d_{Nb2} (nm)	d_{Ni} (nm) for each of 2 layers	Injector R_T ($\Omega \times \text{cm}^2$)	Acceptor R_T ($\Omega \times \text{cm}^2$)
D ₁	Al ₂ O ₃	1	5 × 7.5	5 × 5	30	2	3.1×10^{-7}	3.3×10^{-7}
D ₂	Si/SiO ₂	1	10 × 12	8 × 10	45	2	1.3×10^{-6}	5.5×10^{-7}
D ₃	Al ₂ O ₃	2	10 × 12	4 × 8	35	2	3.9×10^{-7}	2.5×10^{-7}

3.2.1 Modulation of Josephson current in the single-acceptor devices

Similarly to a semiconductor transistor performing the cell selection function in room-temperature magnetic random access memory (MRAM) for cryogenic RAM applications, it is important to be able to control Josephson current with an SFT acting as a cell selector.

Quasiparticle injection from SFIFS junction suppresses the energy gap in the middle (Nb2) electrode, thus resulting in suppression of the Josephson current in the SIS (acceptor) junction. We demonstrate this using the single-acceptor SFTs D1 and D2. Fig. 5.18 shows CVC of the acceptor (black curve 1) and injector (blue curve 2) junctions for device D2. Red curve 3 is initial portion of the acceptor CVC recorded in an applied magnetic field corresponding to the second minimum of the I_c vs. H dependence (where I_c is the critical Josephson current). This curve displays the gap difference feature, which allows us to determine the superconducting energy gaps of the middle Nb2 and the top Nb3 electrodes to be 0.86 meV and 1.22 meV, respectively.

We measured the I_c vs. H dependence for the SIS (i.e., Nb2/Al/AlO_x/Nb3) acceptor junction of device D2 at different levels of current through the injector junction SFIFS. These data are shown in Fig. 5.19. Curves from top to bottom are for the injection current, I_i , from 0 to 4 mA applied with the 0.4 mA increment. Regular shape of the I_c vs. H dependence is preserved up to high injection current; at $I_i = 4.0$ mA the dependence is distorted, which may be due to several reasons: (1) trapping the magnetic flux; (2) development of an inhomogeneous gap state under quasiparticle injection on the scale of diffusion length, or (3) transition into the \square -state under influence of spin injection.

At the same time, we continue testing of the already made devices with two acceptors in order to study the voltage amplification by analogy with our previous work [6]. We expect to achieve higher voltage amplification in these devices. Our preliminary measurements of these devices confirmed that they have excellent input-output isolation, similarly to the devices with a single acceptor reported earlier [6, 7].

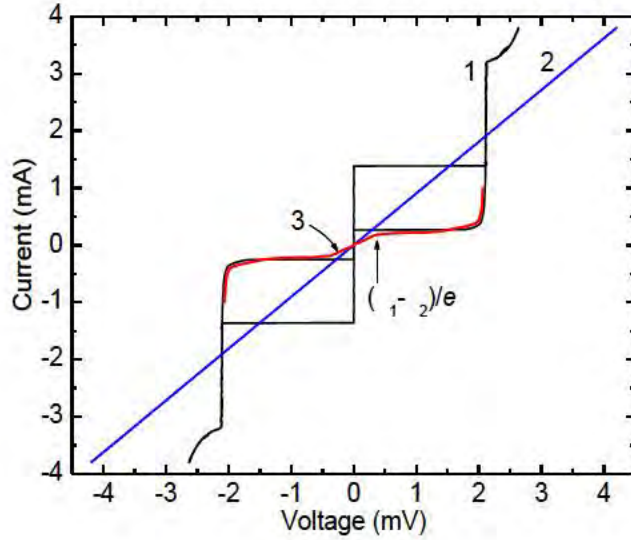


Fig. 5.18. Current-voltage characteristics (CVCs) for SFT device D_2 at 4.2 K. Black curve 1 is CVC of the acceptor SIS junction, blue curve 2 is CVC of the injector SFIFS junction, and red curve 3 is an initial portion of the acceptor CVC in an applied magnetic field corresponding to the 2nd minimum of the I_c vs. H dependence. Gap difference feature is seen in the latter curve.

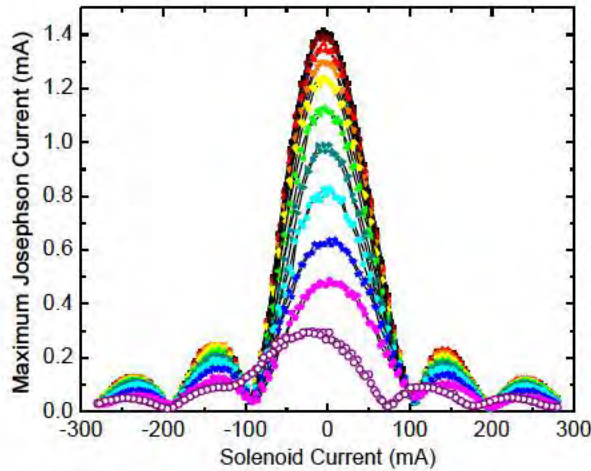


Fig. 5.19. I_c vs. H dependence for the acceptor junction of the device D_2 at different levels of the injection current. Curves from top to bottom are for the injection current from 0 to 4 mA applied with the 0.4 mA increment.

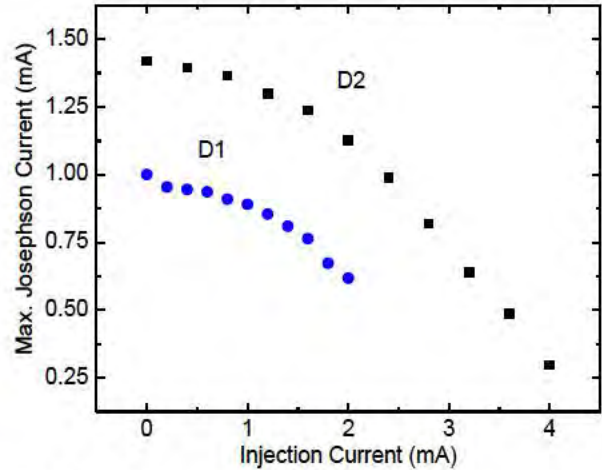


Fig. 5.20. Maximum Josephson current of the acceptor junction vs. the current through the injector junction for devices D_1 and D_2 .

Fig. 5.20 shows maximum Josephson current as a function of the injection current level for devices D_1 and D_2 . The data demonstrate possibility to modulate Josephson current by quasiparticle injection in SFT devices. The further optimization of the devices in order to achieve more efficient modulation is underway.

3.2.2 Amplification

Next we study voltage amplification in the double-acceptor SFTs exemplified by device 3. The experiment, illustrated in Fig. 5.21, was carried out at 4.2 K. In Fig. 5.21, Curve 1 is CVC of the injector; curve 2 is CVC of the double acceptor recorded at zero injection current in an applied magnetic field of 250 Oe; curve 3 is the same CVC but under influence of the injection current corresponding to the DC bias point A in curve 1. If, in addition to DC bias current, a small AC

signal is applied in point A (an image of the oscilloscope screen displaying this signal is shown on bottom in the lower inset) then one obtains an output signal (shown on top in the lower inset) in the operation point B of the double-acceptor CVC. The vertical (voltage) scale is 20 μV per division for the input signal, and 500 μV per division for the output signal. Horizontal scale is 5 ms/division in all cases. The peak-to-peak amplitude of the input signal is 20 μV , whereas the peak-to-peak amplitude of the output signal is about 600 μV ; therefore, the voltage gain is about 30. In the reverse transmission experiment, the input signal (top curve in the upper inset) was fed at the DC bias point D of the double-acceptor CVC, and the output signal (thick line on bottom in the upper inset) was acquired at the operation point C of the injector CVC. The voltage scale is 500 μV per division for the input signal, and 5 μV per division for the output signal proving very good input/output isolation in our SFT device similarly to the devices with a single acceptor reported earlier [6, 7].

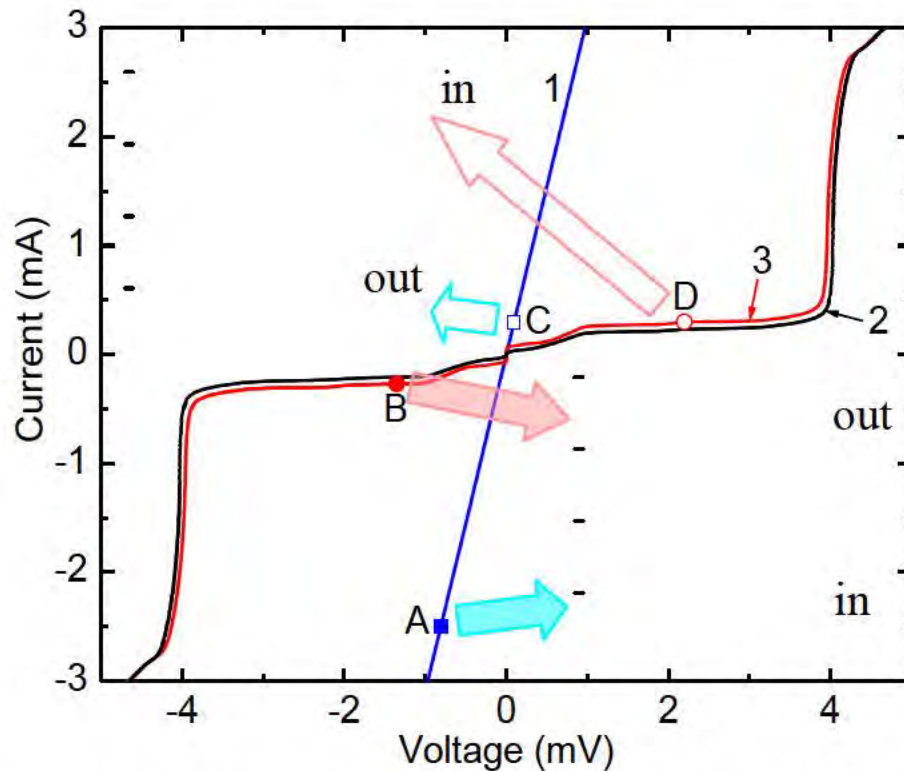


Fig. 5.21. Demonstration of the voltage amplification experiment on device D₃. Curve 1 is CVC of the injector; curve 2 is the unperturbed CVC of the double acceptor in an applied magnetic field of 250 Oe; curve 3 is the same CVC but under influence of the injection current corresponding to the DC bias point A. If a small AC signal is applied in point A (bottom signal in the lower inset) then one obtains an output signal (shown on top in the lower inset) in the operation point B of the acceptor CVC. The vertical (voltage) scale is 20 μV per division for the input signal, and 500 μV per division for the output signal. (Horizontal scale is 5 ms/division in all cases.) One can infer the voltage gain above 25. In the reverse transmission experiment, the input signal (top curve in the upper inset) was fed at the DC bias point D of the acceptor CVC, and the output signal (thick line in the upper inset) was acquired at the operation point C of the injector CVC. The voltage scale is 500 μV per division for the input signal, and 5 μV per division for the output signal. This experiment indicates very good input/output isolation.

Conclusions

During this project period, we made significant progress in two important directions achieving significant results important for the scalable and energy-efficient memory cell implementation critical for the cryogenic dense RAM development based on superconducting-ferromagnetic tunnel junctions:

1. Fabricated and successfully tested a new set of SISFS MJJ devices with smaller size ($2 \times 2 \mu\text{m}^2$). Demonstrated that with the reduction of MJJ size, we were able to retain all properties of our memory device. It showed the ability to be programmed (Write operation), readout (Read operation) with high $I_c R_n$ product (200 μV). To our knowledge, this is the only memory element based on a magnetic Josephson junction and demonstrated Write/Read operation. Similar results were only demonstrated with non-scalable long Josephson junctions (200 μm) with smaller $I_c R_n$ [8].

For further scaling memory element to the sub- μm dimensions, we fabricated and tested an MJJ with two ferromagnetic layers and demonstrated in magneto-resistive measurements $\sim 2.8\%$ critical current difference between parallel (P) and anti-parallel (AP) orientation of ferromagnetic layers.

2. Fabricated and tested a new set of SISFIS SFT devices with single and double acceptor configuration. Demonstrated a modulation of critical current of acceptor by current via injector – the key property of the SFT for the intended use as a memory cell selector. Demonstrated a voltage gain above 25 and perfect input/output isolation for the SFT.

References

- [1] T. I. Larkin, V. V. Bol'ginov, V. S. Stolyarov, V. V. Ryazanov, I. V. Vernik, S. K. Tolpygo, and O. A. Mukhanov, "Ferromagnetic Josephson switching device with high characteristic voltage," *Appl. Phys. Lett.*, vol. 100, art. no. 222601, May 2012.
- [2] V. V. Ryazanov, V. V. Bol'ginov, D. S. Sobanin, I. V. Vernik, S. K. Tolpygo, A. M. Kadin, O. A. Mukhanov, "Magnetic Josephson Junction technology for digital and memory applications," *Physics Procedia*, vol. 36, pp. 35-41, 2012.
- [3] I. V. Vernik, V. V. Bol'ginov, S. V. Bakurskiy, A. A. Golubov, M. Yu. Kupriyanov, V. V. Ryazanov, O. A. Mukhanov, "Magnetic Josephson junctions with superconducting interlayer for cryogenic memory," *IEEE Trans. Appl. Supercond.*, vol. 23, no. 3, art. no. 1701208, Jun. 2013.
- [4] S. V. Bakurskiy, N. V. Klenov, I. I. Soloviev, V. V. Bol'ginov, V. V. Ryazanov, I. V. Vernik, O. A. Mukhanov, M. Yu. Kupriyanov, and A. A. Golubov, "Theoretical Model of Superconducting Spintronic SISFS Devices," *Appl. Phys. Lett.*, vol. 102, art. no. 192603, 2013.
- [5] S. M. Faris, "QUITERON", *Physica*, vol. 126B, pp.165-175, 1984.
- [6] G. V. Prokopenko, O. A. Mukhanov, I. P. Nevirkovets, O. Chernyashevskyy, J. B. Ketterson, "Superconducting-Ferromagnetic-Transistor," *IEEE Trans. on Appl. Supercond.*, vol. 24, no. 4, art. no. 1800506, Aug.. 2014.
- [7] I. P. Nevirkovets and M. A. Belogolovskii, "Hybrid superconductor–ferromagnet transistor-like device", *Supercond. Sci. Technol.*, vol. 24, 024009, 2011.
- [8] E. Goldobin, H. Sickinger, M. Weides, N. Ruppelt, H. Kohlstedt, R. Kleiner, and D. Koelle, "Memory cell based on a ϕ Josephson junction," *Appl. Phys. Lett.*, vol. 102, art. no. 242602, 2013.

Conclusion

During the project, we have achieved the following results:

- We have designed an 8-bit Arithmetic-Logic Unit (ALU) in RSFQ technology. The design is based on Kogge-Stone CLA adder and employs wave-pipeline architecture. The ALU was fabricated and successfully tested at 20-GHz clock frequency, the major and critical part of the proposed processor datapath. The ALU was fully tested for functionality and operational margins. At low speed, the measured critical margin for bias current was +/- 7%. Using an on-chip test-bed based on the controlled SFQ relays, we have fully tested the ALU at 20-GHz clock frequency.
- We have designed, fabricated, and tested an 8-byte Register File comprising a matrix of two banks of four 8-bit registers integrated with control logic block. The complete 8x8-bit Register File was successfully demonstrated. Besides the data port operation, all 64 memory cells of the register file were tested individually at the nominal bias current. The operational margins for dc bias current were varying from -14% / +25% to -1% / +2%.
- In an additional effort, we have developed a novel resistor-free biasing scheme for RSFQ with zero static- and minimal dynamic power dissipation. We called it energy-efficient RSFQ or ERSFQ. It is fully compatible on a cell level with resistive RSFQ logic allowing us to utilize RSFQ cell library with minor modifications. Using this approach, we have designed and successfully demonstrated at high (up to 60 GHz) speed a number of circuits including a static frequency divider by 2^{20} , a detector digital readout (ADC), and two types of an 8-bit parallel adder. The main achievement in energy dissipation reduction was demonstration of ERSFQ 8-bit parallel adder dissipating 160 aJ per operation. All investigated ERSFQ circuits have shown no performance degradation comparing to their RSFQ counterparts and in some cases even excelled them.
- The 8-bit ALU was designed in new ERSFQ technology. The new ALU architecture is based on wave-pipeline ripple-carry adder featuring high throughput (simulated 44 GHz at 4.5 kA/cm² process), asynchronous carry propagation and small latency. At the same time, it operates with high data skew factor that should be matched by the register file.
- The other additional goal of this multi-phase project is to develop and demonstrate the energy-efficient output data interface between cryogenic 4 K superconducting modules and room-temperature semiconductor systems using a combination of energy-efficient on-chip drivers, low loss and dispersion cables, and polarization modulating vertical-cavity emission lasers (PM VCSELs). During this project period, we completed the fabrication and testing of the second generation designs of PM VCSELs with modifications introduced during the previous project period. This new design is based on a “half-VCSEL” structure with dielectric top distributed Bragg reflector (DBR). We fabricated the first iteration of VCSEL devices with dielectric DBR and demonstrated improvement in performance although with lesser polarization control. The second fabrication iteration to address polarization control is 80% complete. Preliminary testing

of these devices before deposition of the top dielectric DBR mirror shows diode current-voltage characteristics, and clear electroluminescence was observed. In addition, we have completed, optimized and employed a cryogenic setup for cryogenic VCSEL testing in wide temperature range. It is based on Sumitomo two-stage cryocooler with accurate temperature control of the first stage. The measurement process and data collection is performed using the developed for the measurements Labview program. We tested a set of VCSEL samples produced by Univ. of Illinois team to verify and calibrate our cryogenic setup. We also fabricated and successfully tested new on-chip energy-efficient driver based on ERSFQ logic. These drivers are based on dc/SFQ converters re-designed to ERSFQ logic. The bias of the driver output stage was implemented via the output data line from the PM VCSEL.

- Another added task was the development of approaches to maximizing energy-efficiency of SFQ digital circuits. We performed the first experimental demonstration of recently proposed energy-efficient single flux quantum logic with zero static power dissipation, eSFQ. We also demonstrate that the introduction of passive phase shifters allows the reduction of dynamic power dissipation by about 20%. Two types of demonstration eSFQ circuits, shift registers and demultiplexers (deserializers), were implemented using the standard HYPRES 4.5 kA/cm² fabrication process.
- The goal of this additional task is to perform development of a 4K Superconducting Ferromagnetic MRAM circuits compatible with Josephson junction digital energy efficient SFQ circuits. A scalable, energy-efficient memory element based on Magnetic Josephson junctions (MJJs) was developed and demonstrated. For SIFS MJJ, we demonstrated the memory properties of two memory states with different critical current values and high I_{cRn} comparable to that of conventional SIS Josephson junctions. We have also demonstrated a superconducting ferromagnetic transistor (SFT) – a three-terminal device with good input/output isolation for integration with MJJ-based memory cell capable of performing the memory cell selector function in random access memory arrays.
- We were redesigning the 8-bit ALU in new ERSFQ technology. In order to achieve integration of the full ERSFQ-based datapath (comprising the ALU, the Register File, and the Instruction Decoder), we developed new fabrication process featuring 6 wiring layers (in contrast to standard 4) and 0.25-um lithography (in contrast to previously employed 1.0 um). The first wafer with ALU blocks and an 8-bit adder will be available next month.
- During this project period, our HYPRES-University of Illinois team worked on the development of PM VCSELs. Specifically, we performed analysis of the existing first generation designs of PM VCSELs in order to identify the necessary design modifications; completed the design of a photomask set for the modified PM VCSELs with a new pattern of photonic crystal; completed fabrication of the PM VCSEL samples; performed testing and evaluation of fabricated VCSELs. While the low threshold voltage was achieved, we identified layout modifications to improve the observed poor PM

VCSEL polarization control. The new design with “half-VCSEL” structure (with dielectric top distributed Bragg reflector) was completed. The fabrication of new samples is underway. In addition, we were constructing a cryogenic setup for cryogenic VCSEL testing. We modified HYPRES cryogenic testbed based on Sumitomo two-stage cryocooler for mounting of PM VCSEL samples on the first stage of the cryocooler. We modified temperature control of the first stage of the cryocooler to enable accurate temperature setting over the 45K to 90K temperature range. We also invented and designed new on-chip energy-efficient drivers based on ERSFQ logic. These drivers are the re-designed dc/SFQ converter with biasing output stage via the output data line of the PM VCSEL. The new ERSFQ dc/SFQ drivers are being fabricated.